

Doctoral Thesis

**A Study on Carrier Transport Properties of  
Vertically-Stacked Nanowire Transistors**

A DISSERTATION SUBMITTED TO THE  
DEPARTMENT OF ELECTRONICS AND APPLIED PHYSICS  
INTERDISCIPLINARY GRADUATE SCHOOL OF  
SCIENCE AND ENGINEERING  
TOKYO INSTITUTE OF TECHNOLOGY  
FOR THE DEGREE OF DOCTOR OF ENGINEERING

**Kiichi Tachi**

March 2011

Supervisor: Professor Hiroshi Iwai



## ABSTRACT

Vertically-stacked silicon nanowire MOSFETs (SNWTs) were experimentally investigated as one of the possible solutions to achieve both high speed, low power consumption in combination with high integration capabilities for future LSI applications. To evaluate the potentials, analyze and improve the performance of these devices, source/drain series resistance for thick source/drain region were studied. Carrier transport mechanisms and the controllability of threshold voltage for vertically-stacked SNWTs with separated gates were also investigated.

The influence of *in situ* doped SEG source/drain was examined for vertically-stacked channel MOSFETs. A large enhancement, by a factor of 2 in the drive current, was obtained when *in situ* doped SEG process was adopted. Detailed parameter extraction from the electrical measurements showed the  $R_{SD}$  values can be reduced by 90 and 75% for *n*- and *p*-FETs, respectively, when *in situ* doped SEG is reinforced by adding ion implantation. On the other hand, by combining the ion implantation to SEG process,  $V_T$  roll-off characteristics and the effective mobility behavior are slightly degraded. Mobility analysis revealed an increase in the Coulomb scattering with  $L_G$  scaling, indicating the diffusion of dopant atoms from S/D regions. Further improvements in the performance can be sought by optimizing the S/D activation annealing step.

In order to enhance the performance of the vertically-stacked nanowire MOSFETs, the carrier transport limiting components caused by short channel effects were assessed. The optimization of drive currents will have to take into account specific effects to vertically-stacked SNWTs. In particular, the use of SiGe sacrificial layer to make vertically-stacked channels cause large mobility degradation due to the surface roughness, resulted from the damage of plasma etching. This leads to the poor ballisticity in the short channel SNWTs. Hydrogen annealing was shown to be advantageous for improving the surface-roughness limited mobility. Charge pumping measurements, however, revealed that circular-shaped SNWTs, which are formed by annealing, have a higher interface trap density ( $D_{it}$ ) than rectangular ones, leading to low-field mobility degradation. This high  $D_{it}$  could be caused by the

continuously-varying surface orientation. The resulting additional coulomb scattering could partly explain the quite low mobility in 5 nm diameter SNWTs together with the already known transport limitations in NWs. Vertically-stacked SNWTs with independent gates by internal spacers between the nanowires to control threshold voltage (named  $\Phi$ -FETs), were evaluated.  $\Phi$ -FETs demonstrated excellent  $V_T$  controllability due to inter-gate coupling effects. Numerical simulations to optimize  $\Phi$ -FETs structures show that when the spacer width is reduced, the DIBL value can be lowered by a factor of 2 compared to independent-gate FinFETs with the same silicon width. The superior scaling of  $\Phi$ -FETs with narrow spacer results from a better electrostatic control which also attenuates the inter-gate coupling.

Overall it was shown that using vertical stack structure can increase the drive current density while allowing for better threshold voltage controllability. As for the performance benchmark, nanowires with a diameter of 10 nm, showed the most acceptable balance between mobility, short channel effect. However, to further improve the device performance, process induced surface damage of nanowires must be mitigated.

## ACKNOWLEDGEMENTS

I would like to thank, first and foremost, my supervisor, Professor Hiroshi Iwai of Tokyo Institute of Technology for his guidance, encouragement and continuous support throughout my research.

I am also grateful to Professor Kenji Natori, Professor Kazuo Tsutsui, Professor Eisuke Tokumitsu, Professor Masahiro Watanabe and Professor Shun-ichiro Ohmi of Tokyo Institute of Technology for reviewing the thesis and for valuable advice.

All studies referred to in this thesis were performed at CEA-Leti in France during the last three years. I am indebted to everyone with whom I have worked at CEA-Leti over the years.

I am also grateful to Dr. Simon Deleonibus, Dr. Olivier Faynot and Dr. Thomas Ernst of CEA-Leti's Electronics Nanodevices Laboratory, and Professor Sorin Cristoloveanu of Grenoble Institute of Technology for their encouragement, useful advices and great help whenever I met difficult and subtle problem.

I would like to thank Professor Kuniyuki Kakushima, Professor Parhat Ahmet, Professor Nobuyuki Sugii, and Professor Akira Nishiyama of Tokyo Institute of Technology for their encouragement support of my studies.

I am also grateful to research colleagues of Iwai's Laboratory for the kind friendship.

I would like to express sincere gratitude to laboratory secretaries, Ms. M. Karakawa, Ms. A. Matsumoto, and Ms. M. Nishizawa for their invaluable assistance regarding administrative issues.

This work was partially performed as part of the IBM-STMicroelectronics-CEA-LETI Development Alliance.

*Acknowledgements*

---

*Acknowledgements*

---

*To my family for their kind  
support and encouragement throughout my life.*

*Merci beaucoup!*

## *Acknowledgements*

---



# CONTENTS

	<i>Page</i>
<i>List of Tables</i>	xi
<i>List of Figures</i>	xiii
<i>Symbols and Abbreviations</i>	xxiii
<b>1 Introduction – MOSFET Scaling –</b>	<b>1</b>
1.1 MOSFET Downsizing	3
1.1.1 Basic CMOS Operation	
1.1.2 MOSFET Scaling	
1.1.3 CMOS Performance Indexes	
1.2 Short Channel MOSFET	18
1.2.1 Short Channel Effects	
1.2.2 Source/Drain Series Resistance in Short-Channel MOSFET	
1.2.3 Carrier Transport Mechanisms in Short-Channel MOSFET	
1.3 Key Technologies to Improve MOSFET Performance	30
1.3.1 Gate-All-Around Silicon Nanowire MOSFET	
1.3.2 Vertically-Stacked Channel MOSFET	
1.4 Purpose and Contents of This Study	39
1.5 References	43

<b>2</b>	<b>Vertically-Stacked Channel MOSFET Fabrication</b>	49
2.1	Silicon-On-Nothing Technology	51
2.2	Process Step Overview for Multi-Channel MOSFET	52
2.3	Process Step Overview for Vertically-Stacked Nanowire MOSFET	54
2.4	Key Steps	59
2.4.1	High-k/Metal Gate Stacks	
2.4.2	SiGe Epitaxy and Etching	
2.5	Conclusions	60
2.6	References	61
 <b>3</b>	 <b>Electrical Characterization Methods</b>	 63
3.1	Introduction	65
3.2	Y-function Method	65
3.3	Split $C-V$ Method	69
3.4	Conclusions	72
3.5	References	72
 <b>4</b>	 <b>Source/Drain Doping Techniques for Vertically-Stacked Channel Structure</b>	 73
4.1	Introduction	75
4.2	Experimental Conditions	76
4.3	Electrical Characteristics	76
4.3.1	$I-V$ Characteristics	
4.3.2	Source/Drain Series Resistance Evaluation	
4.3.3	Carrier Mobility Evaluation	
4.3.4	Gate Length Scaling	
4.4	Conclusions	85
4.5	References	86

<b>5</b>	<b>Carrier Transport Properties of Vertically-Stacked Nanowire MOSFETs</b>	87
5.1	Introduction	90
5.2	Electrical Characteristics	90
5.2.1	<i>I–V</i> Characteristics	
5.2.2	Transport Limiting Velocity	
5.2.3	Carrier Mobility Evaluation	
5.2.4	Mobility Limiting Factors	
5.3	Impact on Plasma Etching of SiGe Sacrificial layers	102
5.3.1	One-Leveled Nanowire MOSFET Fabrication	
5.3.2	Carrier Mobility Evaluation	
5.4	Effect of Hydrogen Annealing	106
5.4.1	Cross-Sectional Shape	
5.4.2	Carrier Mobility Evaluation	
5.4.3	Interface Trap density	
5.5	SiGe Nanowire MOSFET	110
5.5.1	Device Fabrication Process	
5.5.2	<i>I–V</i> Characteristics	
5.5.3	Carrier Mobility Evaluation	
5.5.4	Noise Measurement	
5.6	Conclusions	113
5.7	References	114
<b>6</b>	<b>Threshold Voltage Control of Vertically-Stacked Nanowire MOSFETs</b>	117
6.1	Introduction	119
6.1.1	Threshold Voltage Control by Independent-Gate FinFET	
6.1.2	Vertically-Stacked Nanowire Transistor with Independent Gates	
6.2	Optimization of Device Dimensions	122
6.3	Conclusions	128
6.4	References	128

<b>7</b>	<b>Conclusions</b>	130
7.1	Summary	132
7.2	Conclusions and Perspectives	134
	<i>Publications and Presentations</i>	135
	<i>Awards</i>	143

# LIST OF TABLES

## Chapter 1 Introduction – MOSFET scaling –

Table 1.1	Constant-field scaling and generalized scaling of MOSFET device and circuit parameters.	10
Table 1.2	Key device features of Intel 32 nm logic technology [1.28].	31
Table 1.3	Natural length in devices with different geometries [1.32].	35

## Chapter 2 Vertically-Stacked Channel MOSFET Fabrication

Table 2.1	Nanowire width with various definitions and surface gain factor $W_{\text{eff}}/W_{\text{Top}}$ .	57
Table 2.2	Process description of anisotropic etching of SiGe/Si superlattice	59

## Chapter 4 Source/Drain Doping Techniques for Vertically-Stacked Channel Structure

Table 4.1	Doping scheme	76
-----------	---------------	----

## Chapter 5 Carrier Transport Properties of Vertically-Stacked Nanowire MOSFETs

Table 5.1	Device parameters for vertically-stacked silicon nanowire n- and p-MOSFET with sub-50-nm- $L_{\text{eff}}$ and 15-nm- $W_{\text{Top}}$ . The on-currents $I_{\text{ON}}$ are extracted at $V_G - V_T = 0.7$ and $-0.7$ V for n- and p-MOSFETs, respectively. The off-currents $I_{\text{OFF}}$ are extracted at $V_G - V_T = -0.3$ and $0.3$ V for n- and p-MOSFETs, respectively.	92
-----------	--	----



# LIST OF FIGURES

## Chapter 1 Introduction – MOSFET scaling –

- Figure 1.1 (a) Number of transistors in Intel's microprocessor chips, (b) Average transistor price by year, (c) Clock speed of Intel's microprocessor [1.2, 1.3]. 3
- Figure 1.2 Three-dimensional view of basic CMOS structure.  $V_G$  is gate voltage,  $V_S$  is source voltage,  $V_D$  is drain voltage,  $L_G$  is gate length,  $t_{ox}$  is gate oxide thickness,  $N_a$  is acceptor impurity density,  $N_d$  is donor impurity density,  $x_j$  is junction depth 4
- Figure 1.3 Three regions of a MOSFET operation in the  $V_{DS}$ - $V_G$  plane [1.4]. 5
- Figure 1.4 Typical  $I_{DS}$ - $V_G$  characteristics of an nMOSFET at high drain voltages. The same current is plotted on both linear scale (a) and logarithmic scale (b). 6
- Figure 1.5 (a) Circuit diagram of CMOS inverter. (b) Charge and (c) discharge equivalent circuits. 8
- Figure 1.6 Principles of MOSFET constant-electric-field scaling. 9
- Figure 1.7 CVI performance metric [1.6]. 12
- Figure 1.8 Equivalent circuit with wiring capacitance. 13
- Figure 1.9 (a) Operation of a CMOS inverter in inverter chain. (b)  $I_{DS}$ - $V_{DS}$  curve and trajectories with and without a degraded DIBL for nMOSFET [1.11]. 14
- Figure 1.10 Layout of a CMOS inverter based on lambda-based design rules [1. 15] 15
- Figure 1.11 Sources of leakage current increase as the technology causes gate lengths to shrink. Data from ITRS [1.6] 17
- Figure 1.12 (a) Leakage current components in a nMOSFET, (b)  $I_D$ - $V_G$  curves with and without leakage currents.  $I_{subth0}$  is the initial subthreshold current, while  $\Delta I_{subth}$  is the added current due to the short-channel effects. 17

Figure 1.13	Schematic diagram of the charge-sharing model. The dashed lines indicate the boundary of the gate and source–drain depletion regions. The arrows represent electric field lines that originate from a positive charge and terminate on a negative charge. The dotted lines partition the depletion charge and form the two sides of the trapezoid.	19
Figure 1.14	Surface potential lowering due to the short-channel effects: (a) a long-channel MOSFET, (b) a short-channel MOSFET at low drain bias, (c) a short-channel MOSFET at high drain bias.	21
Figure 1.15	Subthreshold swing calculated by using MASTAR MOSFET modeling software [1.19]: $N_a=10^{18}\text{cm}^{-3}$ , $x_j=30\text{ nm}$ , $t_{ox}=1.3\text{ nm}$ , $V_{DD}=1.2\text{ V}$ , $W=1\mu\text{m}$ .	21
Figure 1.16	DIBL calculated by using MASTAR MOSFET modeling software [1.19]: $N_a=10^{18}\text{cm}^{-3}$ , $x_j=30\text{ nm}$ , $t_{ox}=1.3\text{ nm}$ , $V_{DD}=1.2\text{ V}$ , $W=1\mu\text{m}$ .	22
Figure 1.17	$V_T$ roll-off calculated by using MASTAR MOSFET modeling software [1.19]: $N_a=10^{18}\text{cm}^{-3}$ , $x_j=30\text{ nm}$ , $t_{ox}=1.3\text{ nm}$ , $V_{DD}=1.2\text{ V}$ , $W=1\mu\text{m}$ .	23
Figure 1.18	Off-current increase due to the short-channel effects.	24
Figure 1.19	Equivalent circuit of MOSFET with source and drain resistance [1.4].	24
Figure 1.20	On-currents as a function of source/drain series resistance. All plots are calculated by using MASTAR MOSFET modeling software [1.19]: $N_a=10^{18}\text{cm}^{-3}$ , $t_{ox}=1.3\text{ nm}$ , $V_{DD}=1.2\text{ V}$ , $L_G=50\text{ nm}$ , $W=1\mu\text{m}$ .	25
Figure 1.21	On-current lowering ratio of $R_{SD}=500\ \Omega\cdot\mu\text{m}$ to $100\ \Omega\cdot\mu\text{m}$ as a function of gate length. All plots are calculated by using MASTAR MOSFET modeling software [1.19]: $N_a=10^{18}\text{cm}^{-3}$ , $t_{ox}=1.3\text{ nm}$ , $V_{DD}=1.2\text{ V}$ , $W=1\mu\text{m}$ .	26
Figure 1.22	Schematic diagrams of carrier transport models to determine $I_{ON}$ . (a) Conventional transport model. (b) Quasi-ballistic transport model. (c) Full-ballistic transport model [1.24, 1.25].	27
Figure 1.23	Channel potential profiles under conditions of carrier mobility $\mu$ and velocity $v$ . (a) Linear region. (b) Saturation region.	27
Figure 1.24	Velocity–field relationship for electrons ( $n=2$ ) and holes ( $n=1$ ) by the empirical form inserted [1.22]. The critical field $E_c = v_{sat}/\mu$ .	28
Figure 1.25	$L_G$ dependence of velocity with $\mu$ as parameter [1.27].	30
Figure 1.26	Cross section of Intel’s NMOS and PMOS with 4th generation strained silicon, 2nd generation high- $\kappa$ /metal gate, and raised S/D regions for 32 nm technology [1.28].	31
Figure 1.27	Cross-section of a planar FDSOI MOSFET.	33



Figure 1.28	Various SOI device: (a) Single gate SOI FET, (b) double gate planar SOI FET, (c) double gate non-planar FinFET, (d) tri-gate FET, (e) quadruple-gate (or gate-all-around) FET, and gate-all-around (or surrounding gate) FET (nanowire FET).	33
Figure 1.29	Illustration of electric field lines from drain of different device types: (a) bulk, (b) FD SOI, and (c) double gate (DG).	34
Figure 1.30	Maximum allowed Si thickness and device width vs. gate length to avoid short-channel effects in single-, double- and quadruple-gate SOI MOSFETs [1.35].	35
Figure 1.31	Comparison of DIBL of elliptical GAA SNWTs (width $W = 6.8$ nm and height $H = 9.5$ nm) and single-gate ETSOI FETs (SOI thickness $t_{si} = 8$ nm) with similar body dimensions. [1.36].	35
Figure 1.32	MOSFET layout; (a) planar MOSFET, (b) GAA SNWT with multi-finger, and (c) cross-section of GAA SNWT.	36
Figure 1.33	Normalized current of a rectangular GAA SNWT as a function of multi-finger pitch width. $W_{NW} = W_{pitch}/2$ . The top interface mobility is $300$ cm <sup>2</sup> /Vs and sidewall mobility is $150$ cm <sup>2</sup> /Vs.	37
Figure 1.34	Normalized current of a rectangular GAA SNWT as a function of space between nanowires. $H_{NW} = 10$ nm. The top interface mobility is $300$ cm <sup>2</sup> /Vs and sidewall mobility is $150$ cm <sup>2</sup> /Vs.	38
Figure 1.35	Structure of vertically-stacked GAA SNWT(a) and its cross-section (b)	39
Figure 1.36	Normalized current of a rectangular GAA SNWT as a function of staking level of nanowires. $H_{NW} = 10$ nm. $W_{space} = 30$ nm. The top interface mobility is $300$ cm <sup>2</sup> /Vs and sidewall mobility is $150$ cm <sup>2</sup> /Vs.	39
Figure 1.37	Outline of each chapter in this thesis.	40

## Chapter 2 Vertically-Stacked Channel MOSFET Fabrication

Figure 2.1	Fabrication process of the SON MOSFET: (a) epitaxy of SiGe and Si layers on isolated bulk wafer; (b) conventional CMOS process steps until formation of the nitride spacers; (c) formation of the shallow trenches in the S/D regions and formation of the tunnel under the Si film; (d) filling the tunnel with oxide (optional step); (e) selective epitaxy of S/D regions, implantation and RTA.	51
Figure 2.2	MCFET fabrication process overview [2.2].	53
Figure 2.3	Fabricated multi channel FET (MCFET) along (a) channel length and (b) width direction. (c) is the enlarged image of the gate stack.	54
Figure 2.4	Vertically-stacked nanowire MOSFET fabrication process overview [2.5].	55

Figure 2.5	Fabricated vertically-stacked silicon nanowires: (a) a top-view SEM image, (b) a cross-section TEM image.	55
Figure 2.6	(a) Top-view SEM images of silicon nanowires after HfO <sub>2</sub> deposition with width $W_{SEM} = 16, 26, \text{ and } 36 \text{ nm}$ . (b) Variation of nanowire width in a 200-nm-wafer. The variations are less than $\pm 1.5 \text{ nm}$ . The thickness of HfO <sub>2</sub> on side walls (3nm x 2) is included in the values of $W_{SEM}$ . $W_m$ is the mask width.	56
Figure 2.7	Cross-sectional TEM images of vertically-stacked silicon nanowire MOSFET with top-view width $W_{Top} = 10, 15, 20 \text{ and } 30 \text{ nm}$ .	57
Figure 2.8	(a) Cross-sectional TEM image of vertically-stacked silicon nanowire MOSFET with top-view width $W_{Top} = 5 \text{ nm}$ . (b) Enlarged image of 5-nm-diameter nanowire.	57
Figure 2.9	Top-view (a) and cross-section (b) of SEM images of vertically-stacked silicon nanowire MOSFET with mask length $L_m = 40, 100, \text{ and } 600 \text{ nm}$ .	58
Figure 2.10	Cross-sectional TEM image of vertically-stacked silicon nanowire with high- $\kappa$ /metal gate.	60

### Chapter 3 Electrical Characterization Methods

Figure 3.1	Y-function as a function of the gate voltage.	67
Figure 3.2	Extraction of the effective gate length.	67
Figure 3.3	Extraction of the series resistances for 40nm to 600nm gate lengths MCFET devices ( $W = 500\text{nm}$ ).	68
Figure 3.4	Measured and modeled $I_{Dlin}-V_G$ and $g_{mlin}-V_G$ characteristics of TiN/HfO <sub>2</sub> n-MCFETs. Gate length and width are 70 nm and 350 nm, respectively.	69
Figure 3.5	Comparison of effective mobility extracted by split C-V, double $L_m$ method, and from parameters extracted by Y-function method. The measured device is the stacked SNWTs with $W_{NW} = 15 \text{ nm}$ and $L_{eff} = 242 \text{ nm}$ . The device with $L_{eff} = 592 \text{ nm}$ was also used for double $L_m$ method.	71

### Chapter 4 Source/Drain Doping Techniques for Vertically-Stacked Channel Structure

Figure 4.1	On-off relations of (a) n- and (b) p-MCFETs.	77
Figure 4.2	$V_T$ roll-off characteristics of MCFETs with $L_G$ scaling.	78

Figure 4.3	On-current dependency on the gate length for (a) n- and (b) p-MCFETs.	78
Figure 4.4	Transconductance of the (a) n- and (b) p-MCFETs. Solid lines represent the fitted model.	79
Figure 4.5	$\Theta_{I_{eff}}$ vs. $\beta$ curves of the fabricated (a) n- and (b) p-MCFETs.	79
Figure 4.6	$C_{GC}$ characteristics with various $L_G$ for (a) n- and (b) p-MCFETs.	80
Figure 4.7	$\mu_{eff}$ of the MCFETs with different $L_G$ of 570 and 70 nm.	81
Figure 4.8	Estimated $\mu_0$ on $L_G$ scaling.	82
Figure 4.9	Summary of the extracted $\alpha_\mu$ and $\mu_{max}$ .	83
Figure 4.10	$I_{ON}$ - $I_{OFF}$ characteristics with several channel sizes for nMCFET (a) and pFET (b).	84
Figure 4.11	$I_D$ - $V_G$ (a) and $I_D$ - $V_D$ (b) characteristics for the scaled MCFETs.	85

Chapter 5 Carrier Transport Properties of Vertically-Stacked Nanowire MOSFETs

Figure 5.1	$I_D$ - $V_D$ characteristics of vertically-stacked silicon nanowire n- and p-MOSFET with sub-50-nm- $L_{eff}$ and 15-nm- $W_{Top}$ .	91
Figure 5.2	$I_D$ - $V_G$ characteristics of vertically-stacked silicon nanowire n- and p-MOSFET with sub-50-nm- $L_{eff}$ and 15-nm- $W_{Top}$ .	91
Figure 5.3	Threshold voltage as a function of effective gate length for vertically- stacked silicon nanowire n- and p-MOSFET with 15-nm- $W_{Top}$ .	92
Figure 5.4	Subthreshold slope as a function of effective gate length for vertically- stacked silicon nanowire n- and p-MOSFET with 15-nm- $W_{Top}$ .	93
Figure 5.5	Drain-induced barrier lowering (DIBL) as a function of effective gate length for vertically-stacked silicon nanowire n- and p-MOSFET with 15-nm- $W_{Top}$ .	93
Figure 5.6	$I_{ON}$ - $I_{OFF}$ characteristics of vertically-stacked silicon nanowire n- and p-MOSFET with 15-nm- $W_{Top}$ .	93
Figure 5.7	Saturation current density (a) and linear current density (b) as a function of effective gate length for vertically-stacked silicon nanowire n- and p-MOSFET with 15-nm- $W_{Top}$ . The currents are normalized by top-view width $W_{Top}$ (left y-axis) and effective total width $W_{eff}$ (right y-axis).	94
Figure 5.8	Schematic image of conduction band	95
Figure 5.9	Temperature dependence of saturated electron drift velocity [5.2].	95
Figure 5.10	Injection velocity of a NMOSFET on (100) plane as a function of inversion charge density at 300 and 77 K. [5.3].	95

Figure 5.11	Low-field mobility $\mu_0$ as a function of effective gate length for vertically-stacked silicon nanowire n- and p-MOSFET with 15-nm- $W_{Top}$ .	96
Figure 5.12	Temperature dependence of $I_D$ - $V_G$ characteristics for vertically-stacked SNWTs.	96
Figure 5.13	Temperature dependence of extracted limiting velocity $v_{lim}$ . Theoretical dependence of saturation velocity $v_{sat}$ from [5.5] and injection velocity $v_{inj}$ from [5.6] are given.	97
Figure 5.14	Schematic image of nanowire MOSFET (a) and its cross-section: (b) varying ratio of (100) width to (110) width, (c) varying size, (d) varying radius of curvature at the corners.	98
Figure 5.15	Nanowire mobility as a function of $W_{(100)}$ -to- $W_{(110)}$ ratio. The average mobility is $mave = (\mu_{(100)}W_{(100)} + \mu_{(110)}W_{(110)}) / (W_{(100)} + W_{(110)})$ , where $\mu_{(100)}$ and $\mu_{(110)}$ are the mobilities on (100) and (110) surfaces, respectively.	98
Figure 5.16	Calculated profiles of electron density across the cross section of silicon nanowires with $W_{(110)}=18$ nm, and $W_{(100)}= 7$ and 22 nm [5.7].	99
Figure 5.17	Temperature dependence of effective electron mobility in vertically-stacked silicon nanowire FET (a) and in fully-depleted SOI-FET (b).	100
Figure 5.18	Temperature dependence of effective hole mobility in vertically-stacked silicon nanowire FET.	100
Figure 5.19	(a) Temperature dependence of effective mobility at high inversion charge density ( $N_{INV}=10^{13}$ cm <sup>-2</sup> ). (b) Schematic diagram of mobility limiting components at low temperature.	101
Figure 5.20	Temperature dependence of phonon-limited mobility at high inversion charge density ( $N_{INV}=10^{13}$ cm <sup>-2</sup> ) for vertically-stacked silicon nanowire MOSFETs.	101
Figure 5.21	Mobility limiting components for electron (a) and hole for vertically- stacked silicon nanowire MOSFETs at 300 K.	101
Figure 5.22	Temperature dependence of effective mobility at low inversion charge density ( $N_{INV}=2 \times 10^{12}$ cm <sup>-2</sup> ).	102
Figure 5.23	Atomic force microscopy images of silicon surface after isotropic SiGe dry etching (a) and the reference sample without the etching (b).	102
Figure 5.24	Root mean square (RMS) values as a function of isotropic SiGe dry etching.	103
Figure 5.25	Brief process flow of 1-level silicon nanowire MOSFET.	103
Figure 5.26	Gate-all-around 1-level silicon nanowire MOSFETs fabricated without SiGe epitaxy and selective etching.	103
Figure 5.27	Electron mobility comparisons between 1-leveled and vertically-stacked Si nanowire MOSFET at 300 K (a) and 5 K (b).	104

Figure 5.28	Temperature dependence of effective mobility at high inversion charge density ( $N_{INV}=10^{13} \text{ cm}^{-2}$ ) for 1-leveled and vertically-stacked silicon nanowire MOSFET.	105
Figure 5.29	Temperature dependence of phonon-limited mobility at high inversion charge density ( $N_{INV}=10^{13} \text{ cm}^{-2}$ ) for 1-leveled and vertically-stacked silicon nanowire MOSFETs.	105
Figure 5.30	Mobility limiting components comparison at high inversion charge density between 1-leveled and vertically-stacked silicon nanowire MOSFETs at 300 K.	105
Figure 5.31	Temperature dependence of effective mobility at low inversion charge density ( $N_{INV}=2 \times 10^{12} \text{ cm}^{-2}$ ).	106
Figure 5.32	Cross-sectional TEM images of silicon nanowire (a) without and (b) with hydrogen annealing at 750 °C for two minutes.	106
Figure 5.33	Electron mobility comparison of 1-leveled silicon nanowire MOSFETs between with and without hydrogen annealing. The measurement temperatures are 300 K (a) and 5 K (b).	107
Figure 5.34	Temperature dependence of effective mobility at high inversion charge density ( $N_{INV}=10^{13} \text{ cm}^{-2}$ ) for 1-leveled nanowire MOSFET with and without $\text{H}_2$ anneal.	107
Figure 5.35	Mobility limiting components comparison at high inversion charge density and 300 K for 1-leveled silicon nanowire MOSFET between with and without hydrogen annealing.	108
Figure 5.36	Temperature dependence of effective mobility at low inversion charge density ( $N_{INV}=2 \times 10^{12} \text{ cm}^{-2}$ ).	108
Figure 5.37	Electron mobility comparison of vertically-stacked silicon nanowire MOSFETs between with and without hydrogen annealing.	108
Figure 5.38	Charge pumping currents $I_{cp}$ obtained base voltage sweep on nanowire gated-diode with $L_G = 240 \text{ nm}$ and $W_{NW}/H_{NW} = 20 \text{ nm}/15 \text{ nm}$ . The currents are normalized by $W_{eff}$ obtained from TEM images.	109
Figure 5.39	Charge pumping currents $I_{cp}$ as a function of frequency $f$ .	109
Figure 5.40	Interface trap density as a function of energy for vertically-stacked nanowires with (a) and without (b) hydrogen annealing, and planar SOI devices (c) with the same gate stack (3 nm $\text{HfO}_2$ ALD/10 nm TiN CVD). The profile is obtained by scanning temperature from 300 K down to 25 K by 25 K steps. The bold line represents the mean value of $D_{it}(E)$ . The dashed line is the directly measured mean value of interface trap density over the full energy range at 300 K which evidence the lower density of interface traps in the middle of the gap.	110

Figure 5.41	(a) Cross-sectional TEM micrographs of 3D- stacked compressively(c)- strained SiGe NWTs, (b) enlarged images of c-strained SiGe NW, (c) top view of bended c-strained SiGe NWs with $L_{NW}=600nm$ , (d) top view of c-strained SiGe NWs with $L_{NW}=250nm$ , and (e) top view of un-strained SiGe NWs with $L_{NW}=600nm$ . Short length SiGe NWs are straight, this whatever their strain state.	111
Figure 5.42	$I_{ON}/I_{OFF}$ characteristics of Si, c-strained and un-strained SiGe NWs normalized by the number of wires. The total NW surface $W_{total}$ is estimated from the cross-sectional TEM images. The $W_{NW}$ of all NWs is $\sim 20nm$ .	111
Figure 5.43	Threshold voltage of Si, c-strained and un-strained SiGe NWs as a function of gate length. The $W_{NW}$ of all NWs are $\sim 20nm$ .	112
Figure 5.44	Effective hole mobility of Si, c-strained and un-strained SiGe NWs. The $W_{NW}$ of all NWs are $\sim 20nm$ .	112
Figure 5.45	Low-frequency noise of Si and c-strained SiGe NWs. Inserted figure is a comparison of oxide trap density ( $N_t$ ). $L_G$ and $W_{NW}$ are $\sim 290nm$ and $\sim 20nm$ , respectively.	113

## Chapter 6 Threshold Voltage Control of Vertically-Stacked Nanowire MOSFETs

Figure 6.1	Cross-sectional TEM image of the independent-gate FinFET fabricated by the resist etch back process [6.4].	119
Figure 6.2	$\Phi$ -FET scheme.	121
Figure 6.3	Schematic fabrication sequence of $\Phi$ -FET.	121
Figure 6.4	Cross-sectional TEM pictures of $\Phi$ -FET (3 stacked nanowires). Left: 25s SiN isotropic etching Right: 28s SiN isotropic etching.	121
Figure 6.5	Experimental $I_d-V_{g1}$ characteristics at various $V_{g2}$ for n-channel $\Phi$ -FET. The gate length and channel width are 550 nm and 25 nm, respectively.	122
Figure 6.6	$I_{on}-I_{off}$ characteristics comparison between $\Phi$ -FET and IG-FinFET.	
Figure 6.7	Simulated inversion charge density in a $\Phi$ FET for (a) one gate activated (single drive mode) and (b) two gates activated (double drive mode).	122
Figure 6.8	Schematic illustration of a SNWT with boundary conditions.	124
Figure 6.9	Potential along the channel for a long and short-channel transistor.	125
Figure 6.10	Simplified Poisson equation resolution for long-channel with C.F. for short channel is compared to the drift-diffusion model.	125
Figure 6.11	DIBL versus coupling factor: Silicon width ( $W_{Si}$ ) dependence.	127
Figure 6.12	DIBL versus coupling factor: Spacer width ( $T_{Si}$ ) dependence.	127

*Figure 6.13 DIBL versus coupling factor: Spacer width ( $W_{sp}$ ) dependence.* 127

*Figure 6.14 Lateral gates can screen narrow silicon body from the other gate influence.* 128

Chapter 7 Conclusions

*Figure 7.1 Figure 7.1 Cross-sectional TEM image of the 19 period superlattice with 19 nm  $Si_{0.8}Ge_{0.2}$  and 32 nm of Si [fabricated by J.M. Hartmann in CEA-Leti].* 134





## LIST OF SYMBOLS AND ABBREVIATIONS

---

### A

AFM	Atomic Force Microscopy
ALD	Atomic Layer Deposition
$\alpha_\mu$	Mobility degradation factor

---

### B

BEOL	Back-End-Of-the-Line
BOX	Buried Oxide
$\beta$	Gain factor of the transistor

---

### C

CMOS	Complementary MOS
CMP	Chemical Mechanical Polishing
$C$	Capacitance [F]
$C_{dm}$	Maximum depletion-layer capacitance per area [F/cm <sup>2</sup> ]
$C_{ox}$	Gate oxide capacitance per area [F/cm <sup>2</sup> ]

*List of symbols and abbreviations*

---

$C_{in}$	Input capacitance of the next stage or stages [F]
$C_{out}$	Output capacitance of the switching inverter [F]
$C_{wire}$	Wiring capacitance [F]
$C_G$	Gate capacitance [F]
$C_{GC}$	Gate-to-channel capacitance [F]
$C_L$	Load capacitance [F]
$C_{L(W)}$	Load capacitance depending on gate width [F]

---

## **D**

DG	Double gate
DIBL	Drain-induced barrier lowering
$D_{it}$	Interface trap density

---

## **E, $\epsilon$**

EI	Electrostatic integrity
EOT	Equivalent oxide thickness
$E_{eff}$	Transverse effective electric field [V/cm]
$E_g$	Band gap [eV]
$E_{lateral}$	Lateral electric field [V/cm]
$E_F$	Fermi energy [eV]
$E_s$	Electric field near source edge [V/cm]
$\epsilon_0$	Vacuum permittivity [8.85 x 10 <sup>-14</sup> F/cm]
$\epsilon_s$	Semiconductor permittivity [Si: 1.04 x 10 <sup>-12</sup> F/cm]
$\epsilon_{ox}$	Silicon-dioxide permittivity [3.45 x 10 <sup>-13</sup> F/cm]
$\epsilon_r$	Relative permittivity

---

## **F**

FDSOI	Fully-depleted SOI
$f$	Frequency [Hz]

*List of symbols and abbreviations*

---

$f_{clk}$	Clock frequency
$\Phi_B$	Potential barrier [eV]
$\Phi_{MS}$	Work-function difference between metal and silicon [eV]

---

## **G**

GIDL	Gate-Induced Drain Leakage
GAA	Gate-All-Around
$g_m$	Transconductance [S]

---

## **H**

HM	Hard Mask
HP	High Performance logic
HTO	High-Temperature Oxide
$H_{fin}$	Fin height [cm]
$H_{NW}$	Nanowire hight [cm]
$\eta_F$	Reduced Fermi energy [eV]

---

## **I**

IG	Independent-Gate
I/I	Ion Implantation
$I_{Dlin}$	Drain current at low drain voltage [A]
$I_{Dsat}$	Saturation current [A]
$I_{DS}$	Drain-to-source current [A]
$I_{ON}$	On-state current [A]
$I_{OFF}$	Off-state current [A]
$I_N$	nMOSFET drain current in a CMOS inverter [A]
$I_P$	pMOSFET drain current in a CMOS inverter [A]
$I_{GIDL}$	Gate-induced drain leakage current [A]
$I_{cp}$	Charge pumping current [A]

## *List of symbols and abbreviations*

---

$I_{leak}$	Total leakage current including gate and junction leakages [A]
$I_{gate}$	Gate leakage current [A]
$I_{subth}$	Subthreshold current [A]
$I_{Tr}$	Transistor current corresponding to the threshold voltage [A]

---

## **J**

$J_G$	Gate leakage current density [A/cm <sup>2</sup> ]
-------	---

---

## **K, κ**

$k$	Boltzmann constant [=8.617 x 10 <sup>-5</sup> eV/K]
$\kappa$	Scaling factor, Relative dielectric constant

---

## **L**

LOP	Low Operating Power logic
LSTP	Low Standby Power logic
LSI	Large-Scale Integrated circuit
$L_G$	Physical gate length [cm]
$L_{eff}$	Electrical channel length [cm]
$L_{ov}$	Gate overlap length [cm]
$L_m$	Mask gate length [cm]
$\lambda$	Backscattering mean free path of carriers [cm]
$\lambda$	Natural length [cm]
$l$	Critical length of scattering [cm]

---

## **M, μ**

MBCFET	Multi-Bridge Channel MOSFET
MCFET	Multi-Channel MOSFET
MOSFET	Metal-Oxide-Silicon Field-Effect-Transistor
$m$	Body-effect coefficient

*List of symbols and abbreviations*

---

$m^*$	Carrier effective conduction mass
$\mu_{eff}$	Effective mobility [ $\text{cm}^2/\text{V}\cdot\text{s}$ ]
$\mu_s$	Mobility near source edge [ $\text{cm}^2/\text{V}\cdot\text{s}$ ]
$\mu_{ph}$	Phonon limited mobility [ $\text{cm}^2/\text{V}\cdot\text{s}$ ]
$\mu_{sr}$	Surface-roughness limited mobility [ $\text{cm}^2/\text{V}\cdot\text{s}$ ]
$\mu_{cb}$	Coulomb limited mobility [ $\text{cm}^2/\text{V}\cdot\text{s}$ ]
$\mu_0$	Low-field mobility [ $\text{cm}^2/\text{V}\cdot\text{s}$ ]

---

## **N**

$N_{INV}$	Inversion charge density [ $\text{cm}^{-2}$ ]
$N_{INV}^{source}$	Inversion charge density near source edge [ $\text{cm}^{-2}$ ]
$N_a$	Acceptor impurity concentration [ $\text{cm}^{-3}$ ]
$N_d$	Donor impurity concentration [ $\text{cm}^{-3}$ ]
$N_t$	Oxide trap density

---

## **O**

## **P**

---

## **Q**

$q$	Unit electronic charge [C]
$Q_i$	Inversion charge per unit gate area [ $\text{C}/\text{cm}^2$ ]
$Q_B$	Total gate depletion charge [C]
$Q_{inv}$	Inversion charge [C]
$\theta_{eff}$	Mobility reduction factor

$\theta_1$	First order mobility reduction coefficient
$\theta_2$	Second mobility reduction coefficient

---

## **R**

RMS	Root Mean Square
RP-CVD	Reduced-Pressure Chemical Vapor Deposition
$R_{SD}$	Source/drain series resistance
$R_S$	Source resistance
$R_D$	Drain resistance
$r$	Backscattering rate near-source region

---

## **S**

SEG	Selective Epitaxial Growth
SEM	Scanning Electron Microscopy
SNM	Static Noise Margin
SNWT	Silicon NanoWire field-effect Transistor
SOI	Silicon-On-Insulator
SON	Silicon-On-Nothing
SRAM	Static Random Access Memory
STI	Shallow Trench Isolation
$S_Y$	Y-function slope
SS	Subthreshold swing [V/decade]

---

## **T, $\tau$**

TEM	Transmission electron microscopy
$T$	Temperature [K]
$T_{dep}$	Thickness of depletion layer
$t_{ox}$	Gate oxide thickness [cm]
$t_{Si}$	Silicon thickness [cm]

$t_r$	Rising time [s]
$t_f$	Falling time [s]
$\tau$	Average time between two collisions [s]
$\tau_n$	nMOSFET pull-down delay [s]
$\tau_p$	pMOSFET pull-up delay [s]

---

## U

---

## V

VDT	Voltage-Doing Transformation
$V_T$	Threshold voltage [V]
$V_{DD}$	Power-supply voltage [V]
$V_G$	Gate voltage [V]
$V_S$	Source voltage [V]
$V_D$	Drain voltage [V]
$V_{DS}$	Source–drain voltage [V]
$V_{Dsat}$	Drain saturation voltage [V]
$V_{in}$	Input voltage [V]
$V_{out}$	Output voltage [V]
$V_{fb}$	Flat-band voltage [V]
$V_{base}$	Gate pulse base level [V]
$V_{Tlong}$	Threshold voltage in a long-channel device [V]
$V_{bi}$	Built-in voltage [V]
$V_{thermal}$	Thermal voltage ( $= kT/q$ ) [V]
$v_s$	Average carrier velocity near the source edge [cm/s]
$v_{sat}$	Saturation velocity [cm/s]
$v_{\theta}$	Ballistic velocity of carriers [cm/s]
$v_{inj}$	Injection carrier velocity at the top of the barrier near the source edge [cm/s]

---

*List of symbols and abbreviations*

---

## **W**

$W$	Gate width [cm]
$W_d$	Depletion-layer depth [cm]
$W_{dm}$	Maximum depletion-layer depth [cm]
$W_{space}$	Lateral space between nanowires for multi-finger [cm]
$W_{pitch}$	Nanowire Pitch for multi-finger [cm]
$W_{NW}$	Nanowire width [cm]
$W_{fin}$	Fin width [cm]
$W_m$	Mask gate width [cm]
$W_{TOT}$	Total gate width [cm]
$W_{Top}$	Top-view width [cm]
$W_{sp}$	Spacer width [cm]

---

## **X**

$x_j$	Source/drain junction depth [cm]
-------	----------------------------------

---

## **Y, $\psi$**

$\psi_B$	Difference between Fermi level and intrinsic level
$\psi_S$	Surface potential [eV]

---

## **Z**

$\mathfrak{F}_n$	Fermi integral of the $n$ th order
------------------	------------------------------------

---



# **CHAPTER 1**

---

## *INTRODUCTION – MOSFET SCALING –*

---

Silicon-based large-scale integrated circuits (LSIs) have been rapidly developed in the past 40 years with an unprecedented growth of the semiconductor industry, bringing an enormous impact on the way people work and live. This evolution is owed to the continued downsizing of metal-oxide-silicon field-effect-transistors (MOSFETs). Recently, however, the conventional miniaturization has caused various problems such as threshold voltage roll-off, subthreshold leakage, gate leakage, etc.

In this chapter, firstly, the conventional scaling method and the basic operation of MOSFET are described. Then the specific features of short-channel MOSFETs are considered. The latter half of this chapter covers the proposed solutions and challenges to continue the scaling toward purpose of this thesis.

---

# CHAPTER 1 CONTENTS

## **1 Introduction – MOSFET Scaling –**

### 1.1 MOSFET Downsizing

#### 1.1.1 Basic CMOS Operation

#### 1.1.2 MOSFET Scaling

#### 1.1.3 CMOS Performance Indexes

### 1.2 Short Channel MOSFET

#### 1.2.1 Short Channel Effects

#### 1.2.2 Source/Drain Series Resistance in Short-Channel MOSFET

#### 1.2.3 Carrier Transport Mechanisms in Short-Channel MOSFET

### 1.3 Key Technologies to Improve MOSFET Performance

#### 1.3.1 Gate-All-Around Silicon Nanowire MOSFET

#### 1.3.2 Vertically-Stacked Channel MOSFET

### 1.4 Purpose and Contents of This Study

### 1.5 References

## 1.1 MOSFET DOWNSIZING

Since the invention of the CMOS (complementary MOS) in 1963, which both  $n$ -channel and  $p$ -channel MOSFETs are constructed simultaneously on the same substrate, the number of transistors on a chip has increased by MOSFET downsizing in accordance with Moore’s Law proposed by Gordon E. Moore in 1965 [1.1]. His prediction states that the number will double about every two years. That has happened fairly regularly up to the current time as shown in Figure 1.1 (a) [1.2]. In addition, the average transistor price has decreased markedly over the past four decades (Figure 1.1 (b)) [1.3]. Increasing transistor budgets and decreasing average price per transistor opens up the possibility for high-speed designs that were not technologically or economically feasible in the past (Figure 1.1 (c)) [1.2]. The speed improvements have been achieved by MOSFET scaling. In this section, the basic MOSFET operation principle and the scaling rule are described.

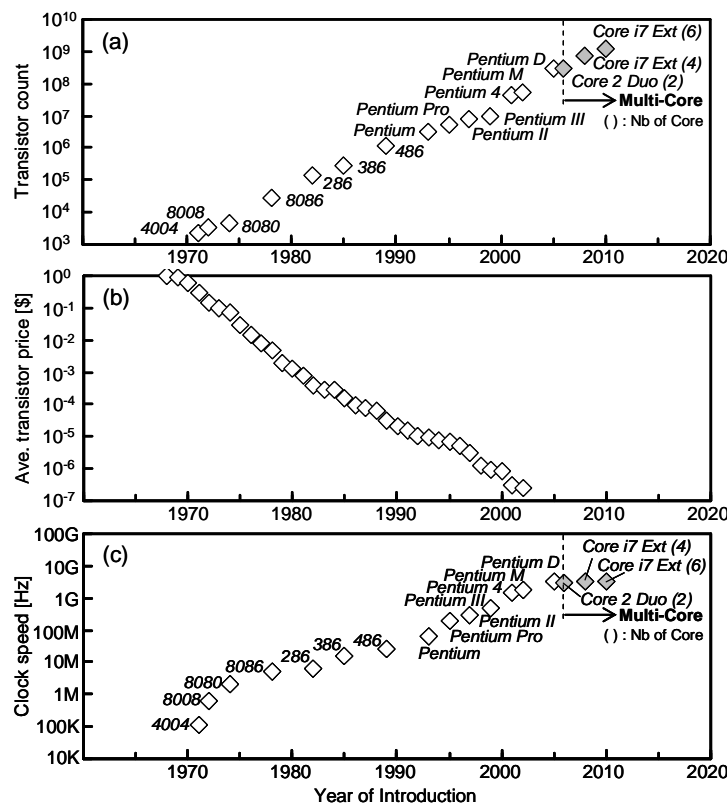


Figure 1.1 (a) Number of transistors in Intel’s microprocessor chips, (b) Average transistor price by year, (c) Clock speed of Intel’s microprocessor [1.2, 1.3].

### 1.1.1 Basic CMOS Operation

A schematic three-dimensional illustration of conventional CMOS transistors of the year early 2000 or earlier, consisting of an n-channel MOSFET (nMOSFET) and a p-channel MOSFET (pMOSFET) integrated on the same chip, is shown in Figure 1.2. The MOSFET is a four-terminal device with the terminals designed as *gate*, *source*, *drain* and *substrate* or *body*. The nMOSFET consists of a p-type silicon (Si) substrate into which n+ regions, the source and the drain, are formed (e.g., by ion implantation). The gate electrode is usually made of heavily doped polysilicon (poly-Si) and is insulated from the substrate by a thin silicon dioxide ( $\text{SiO}_2$ ) film, the gate oxide. The  $\text{SiO}_2$  film is usually formed by thermal oxidation of silicon substrate. The surface region under the gate oxide between the source and the drain is called the *channel* region and is critical for current conduction in a MOSFET. One of the main reasons for successfully developing MOSFET is the presence of the  $\text{SiO}_2$  film which is able to form a thermally stable and high quality interface between the gate oxide and the channel. To obtain low resistive contact, metal silicide is formed on the polysilicon gate as well as on the source and drain diffusion regions. A MOSFET is surrounded by a thick oxide called the field oxide to isolate it from the adjacent devices. The key physical parameters are gate length ( $L_G$ ), gate width ( $W$ ), source/drain junction depth ( $x_j$ ), gate oxide thickness ( $t_{ox}$ ), and channel dopant concentration ( $N_a, N_d$ ).

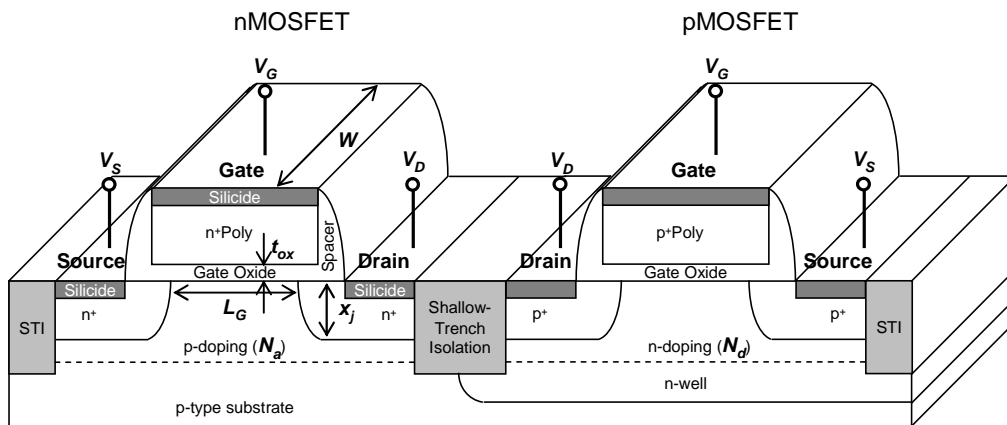


Figure 1.2 Three-dimensional view of basic CMOS structure.  $V_G$  is gate voltage,  $V_S$  is source voltage,  $V_D$  is drain voltage,  $L_G$  is gate length,  $t_{ox}$  is gate oxide thickness,  $N_a$  is acceptor impurity density,  $N_d$  is donor impurity density,  $x_j$  is junction depth

### ■ Drain–Source Current Model

In the MOSFET, an inversion charge layer at the silicon–gate oxide interface acts as a conducting channel. For example, in an nMOSFET, the substrate is  $p$ -type silicon and the inversion charge consists of electrons that form a conducting channel between the  $n^+$  ohmic source and the drain contacts. The onset of strong inversion is defined in terms of a threshold voltage ( $V_T$ ) being applied to the gate electrode relative to the other terminals. Depending on the gate voltage ( $V_G$ ) and source–drain voltage ( $V_{DS}$ ), a MOSFET can be biased in one of the three regions: linear region, saturation region, and subthreshold region, as shown in Figure 1.3.

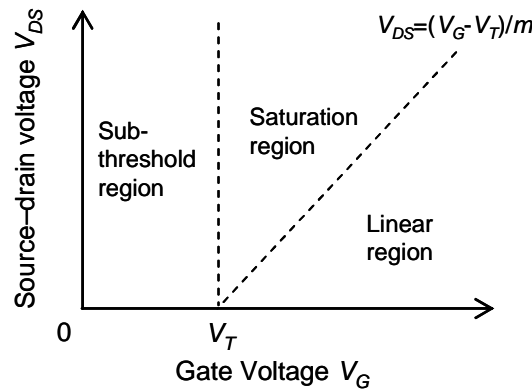


Figure 1.3 Three regions of a MOSFET operation in the  $V_{DS}$ – $V_G$  plane [1.4].

Here the drain–source current ( $I_{DS}$ ) model for long-channel MOSFETs is described. One of the key assumption is the *gradual–channel approximation*, which assumes that the transverse field in the channel is much larger than the longitudinal field, that is one-dimensional. This allows us to express  $I_{DS}$  as [1.4]

$$I_{DS} = \mu_{eff} \frac{W}{L_G} \int_0^{V_{DS}} (-Q_i(V)) dV, \quad (1.1)$$

where  $\mu_{eff}$  is the effective mobility of carriers and  $Q_i$  is the inversion charge per unit gate area. The drain–source current based on the gradual–channel approximation is valid for most of the  $V_{DS}$  regions except beyond saturation voltage ( $V_{DSat}$ ). Beyond  $V_{DSat}$ ,  $I_{DS}$  stays constant at a saturation value ( $I_{DSat}$ ), independent of  $V_{DS}$ . In addition, the use of the *charge-sheet model*, which assumes that the inversion layer is a charge sheet as zero

thickness, allows us to simply express the  $I_{DS}$  in each  $V_{DS}$  region as the following equations:

$$I_{DS} = \mu_{\text{eff}} C_{\text{ox}} \frac{W}{L_G} (V_G - V_T) V_{DS} \quad \text{for } V_{DS} \leq V_G - V_T \text{ (linear region)} \quad (1.2)$$

$$I_{D\text{sat}} = \mu_{\text{eff}} C_{\text{ox}} \frac{W}{L_G} \frac{(V_G - V_T)^2}{2m} \quad \text{for } V_{DS} > V_{D\text{sat}} \text{ (saturation region)} \quad (1.3)$$

where  $C_{\text{ox}} (= \epsilon_{\text{ox}}/t_{\text{ox}})$  is the gate oxide capacitance per area,  $\epsilon_{\text{ox}}$  is the oxide permittivity of the gate oxide,  $m$  is the body-effect coefficient related to doping concentration and oxide thickness.

When the gate bias is below the threshold voltage and the semiconductor is in weak inversion or depletion, the corresponding drain current is called the subthreshold current. The subthreshold region tells how sharply the current drops with gate bias. Figure 1.4 shows schematic  $I_{DS} - V_G$  curves of nMOSFETs. The  $I_{DS}$  at  $V_G = 0$  and  $V_{DS} = V_{DD}$  is equivalent to the off-state current ( $I_{\text{OFF}}$ ), while the  $I_{DS}$  at  $V_G = V_{DS} = V_{DD}$  is equivalent to the on-state currents ( $I_{\text{ON}}$ ). Here, the  $V_{DD}$  is the power-supply voltage. The transition from one state to another defines the  $V_T$  of the MOSFET. In Figure 1.4 (a),  $I_{DS}$  on a linear scale appears to approach zero immediately below the threshold voltage. On a logarithmic scale, however, it is seen that the descending  $I_{DS}$  remains at nonnegligible levels for several tenths of a volt below  $V_T$  (Figure 1.4 (b)).

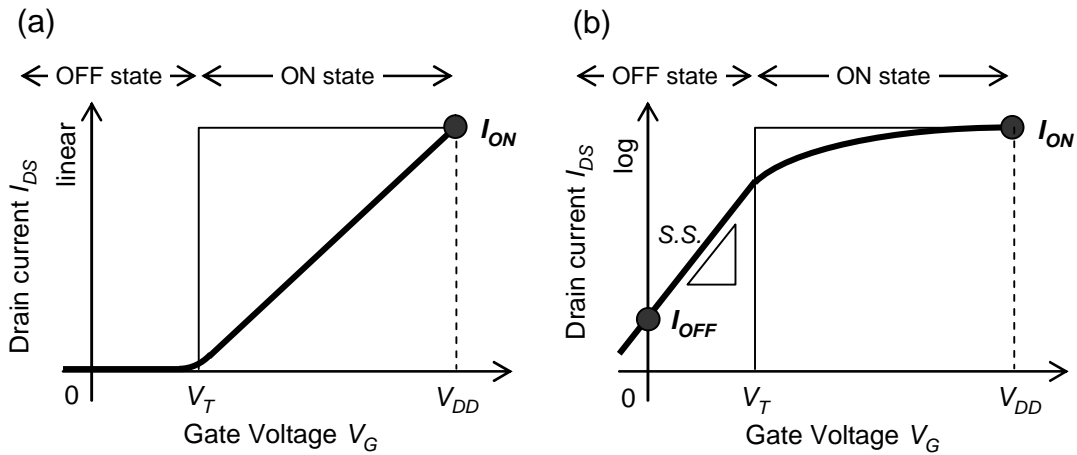


Figure 1.4 Typical  $I_{DS} - V_G$  characteristics of an nMOSFET at high drain voltages. The same current is plotted on both linear scale (a) and logarithmic scale (b).

In general, the current density in the semiconductor can be expressed by the sum of the drift current density and the diffusion current. In weak inversion and depletion, however, electron charge is small and thus, the drift current is low. The drain current is dominated by diffusion. Therefore, the inversion charge density ( $N_{INV}$ ) does not drop to zero abruptly. One can write the subthreshold current ( $I_{subth}$ ) a function of  $V_G$  as

$$I_{subth} = \mu_{eff} C_{ox} \frac{W}{L_G} (m-1) \left( \frac{kT}{q} \right)^2 e^{q(V_G - V_T)/mkT} (1 - e^{-qV_{DS}/kT}) \quad (\text{subthreshold region}), \quad (1.4)$$

where  $q$  is electronic charge,  $k$  is the Boltzmann constant, and  $T$  is temperature. The subthreshold current is independent of the drain voltage once  $V_{DS}$  is larger than a few  $kT/q$ , as would be expected for diffusion-dominated current transport. The dependence on gate voltage, on the other hand, is exponential. The subthreshold behaviors are primarily determined by fabrication technology considerations. The parameter to quantify how sharply the MOSFET is turned off by the gate voltage is called the subthreshold swing ( $SS$ ), defined as the gate-voltage change needed to induce a drain-current change of one order of magnitude. The  $SS$  thus can be written as

$$SS = \left( \frac{d \log_{10} I_{DS}}{dV_G} \right) = \ln(10) \frac{kT}{q} \left( 1 + \frac{C_{dm}}{C_{ox}} \right), \quad (1.5)$$

where  $C_{dm}$  is the maximum depletion-layer capacitance per area.

## ■ CMOS Inverter

The most basic component of digital static CMOS circuits is a CMOS inverter, which is composed by an nMOSFET and a pMOSFET as shown in Figure 1.5 (a). The source terminal of the nMOSFET is grounded, while that of the pMOSFET is connected to the  $V_{DD}$ . The gates of the two MOSFETs are connected as the input node, and the drains are connected as the output node. Here,  $C_L$  in Figure 1.5 is a lumped load capacitance of the output node (including the output capacitance  $C_{out}$  of the switching inverter, the input capacitance  $C_{in}$  of the next stage or stages it drives, and the wiring capacitance  $C_{wire}$ ). The current through the pMOSFET ( $I_P > 0$ ) flows from  $V_{DD}$  into the output node and tends to charge up the node voltage toward  $V_{DD}$  (i.e., pull-up), while the current through the nMOSFET ( $I_N > 0$ ) flows out of the output node into the ground and

tends to discharge the node voltage to zero (i.e., pull-down) as shown in Figure 1.5 (b) and (c). In such a system, the complementary nature of n- and pMOSFETs allows one and only one MOSFET to be conducting in one of the two stable states. Since only one of the MOSFETs is “on” in the steady state, there is little static current or static power dissipation. In principle, the power dissipation occurs only during switching transients when a charging or discharging current is flowing through the circuit [1.4].

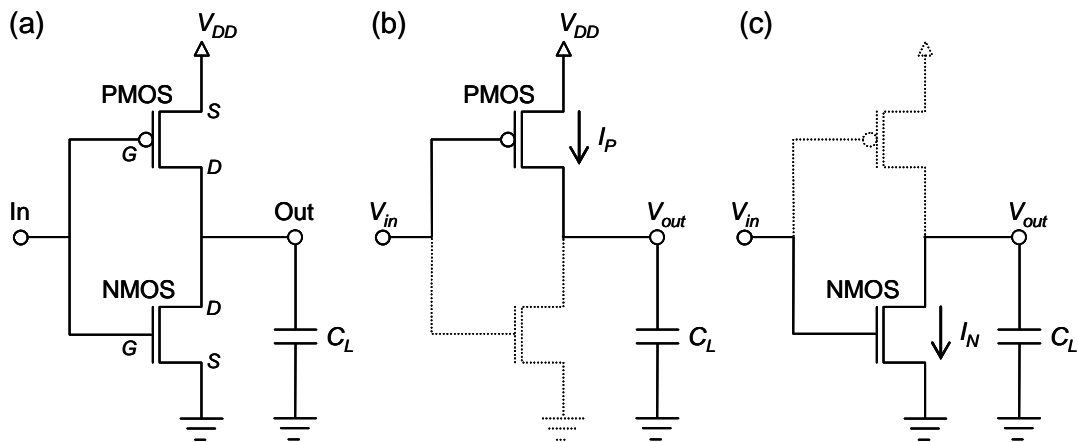


Figure 1.5 (a) Circuit diagram of CMOS inverter. (b) Charge and (c) discharge equivalent circuits.

### 1.1.2 MOSFET Scaling

The CMOS performance is basically evaluated by three indexes: its *switching speed*, *power consumption*, and *integration density*. These indexes have been successfully developed in the past 40 years. This progress has been achieved on the basis of MOSFET scaling rule. As the channel length decreases, the depletion width ( $W_d$ ) of the source and drain becomes comparable to the channel length. This will cause short-channel effects (as described in detail in Section 1.2). Because the short-channel effects complicate device operation and degrade device performance, these effects should be eliminated or minimized so that a physical short-channel device can preserve the electrical long-channel behavior. The most-ideal scaling rule to avoid the short-channel effects is simply to reduce all device dimensions (both horizontal and vertical) and voltages and increase channel doping level by the same factor ( $\kappa > 1$ ) as



shown in Figure 1.6, so that the electric field remains unchanged and the depletion width of the source and drain is reduced. This scaling is called “constant-field scaling” proposed by R. Dennard in 1974 [1.5]. The scaling rule is summarized in Table 1.1. In the scaled MOSFETs, the current equations (1.2, 1.3) can be rewritten as

$$I'_{DS} = \mu_{eff} \frac{\epsilon_0 \epsilon_{ox}}{(t_{ox}/\kappa)} \frac{W/\kappa}{L_G/\kappa} \left( \frac{V_G - V_T - mV_{DS}/2}{\kappa} \right) (V_{DS}/\kappa) = \frac{I_{DS}}{\kappa} \quad (\text{linear region}) \quad (1.6)$$

$$I'_{DS} = \mu_{eff} \frac{\epsilon_0 \epsilon_{ox}}{(t_{ox}/\kappa)} \frac{W/\kappa}{L_G/\kappa} \left( \frac{V_G - V_T}{\kappa} \right)^2 / 2m = \frac{I_{DS}}{\kappa}. \quad (\text{saturation region}) \quad (1.7)$$

Since the current is reduced by the factor of  $\kappa$ , the channel current per unit of channel width is unchanged by scaling. This is consistent with the same sheet density of carriers moving at the same velocity. As a result, the switching speed, the power consumption, and the integration density are improved by factor of  $\kappa$ ,  $1/\kappa^2$ , and  $\kappa^2$ , respectively.

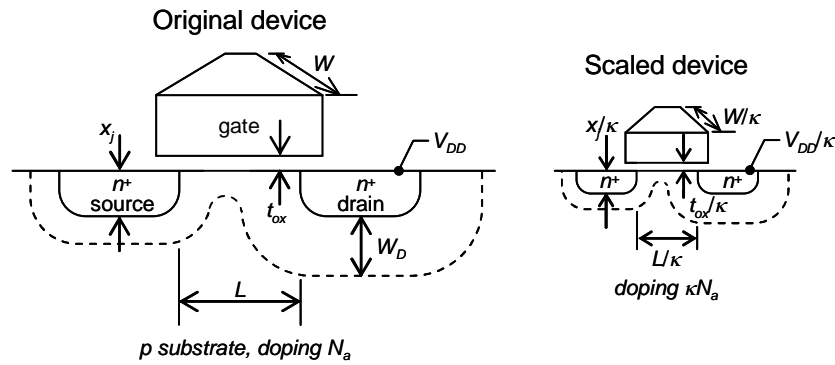


Figure 1.6 Principles of MOSFET constant-electric-field scaling.

In reality, because of the unwillingness to depart from the standardized voltage levels of the previous generation, the power-supply voltage was seldom scaled in proportion to channel length. Even though constant-field scaling provides a basic guideline to the design of scaled MOSFETs, the requirement of reducing the voltage by the same factor as the device physical dimension is too hard. Moreover, there are several factors that scale neither with the physical dimensions nor with the operating voltage. The primary reason for the nonscaling effects that neither the thermal voltage ( $V_{thermal} = kT/q$ ) nor the silicon band gap ( $E_g$ ) changes with scaling. Because of the exponential dependence of subthreshold current (see the equation (1.4)), the threshold

voltage cannot be scaled down significantly without causing a substantial increase in the off-current. In fact, even if the threshold voltage is held unchanged, the off-current per device still increases by a factor  $\kappa$  (from the  $C_{ox}$  factor) when the physical dimensions are scaled down by  $\kappa$ . Note that the  $SS$  factor remains essentially the same since  $SS$  is proportional to  $1+C_{dm}/C_{ox}$  (see the equation (1.5)) and both capacitances are scaled up by the same factor  $\kappa$ . In addition, the process difficulties for aggressively scaled MOSFETs also limit the scaling. With the practical limitations, other scaling rules have been proposed, including constant-voltage scaling and generalized scaling [1.4]. This allows the various device parameters to be adjusted independently as long as the overall behavior is preserved. These nonideal factors, which hinder constant-field scaling, result in some form of a penalty as shown in Table 1.1, especially power consumption. Therefore, it is important to understand how factors affect the performance of a CMOS LSI chip in order to obtain an optimized device structure.

*Table 1.1 Constant-field scaling and generalized scaling of MOSFET device and circuit parameters.*

	Device and Circuit Parameters	Multiplicative Factor ( $\kappa > 1$ )	
		Constant-field Scaling	Generalized Scaling
Scaling assumptions	Device dimensions ( $t_{ox}, L, W, x_j$ )	$1/\kappa$	$1/\kappa$
	Doping concentration ( $N_a, N_d$ )	$\kappa$	$\alpha\kappa$
	Voltage ( $V$ )	$1/\kappa$	$\alpha/\kappa$
Derived scaling behavior of device parameters	Electric field ( $E$ )	1	$\alpha$
	Carrier velocity ( $v$ )	1	$\alpha$ 1
	Depletion-layer width ( $W_d$ )	$1/\kappa$	$1/\kappa$
	Capacitance ( $C = \epsilon A/t$ )	$1/\kappa$	$1/\kappa$
	Inversion/layer charge density ( $Q_i$ )	1	$\alpha$
	Current, drift ( $I$ )	$1/\kappa$	$\alpha^2/\kappa$ $\alpha/\kappa$
Derived scaling behavior of circuit parameters	Circuit delay time ( $\tau \sim CV/I$ )	$1/\kappa$	$1/\alpha\kappa$ $1/\kappa$
	Power dissipation per circuit ( $P \sim VI$ )	$1/\kappa^2$	$\alpha^3/\kappa^2$ $\alpha^2/\kappa^2$
	Power/delay product per circuit ( $P\tau$ )	$1/\kappa^3$	$\alpha^2/\kappa^3$
	Circuit density ( $\propto I/A$ )	$\kappa^2$	$\kappa^2$
	Power density ( $P/A$ )	1	$\alpha^3$

### 1.1.3 CMOS Performance Indexes

The need for devices that consume a minimum amount of power was a major driving force behind the development of CMOS technologies. As a result, CMOS devices are best known for low power consumption due to the unique characteristic of zero standby power. This enables higher integration levels and makes them the technology of choice for most LSI applications. However, continuing aggressive scaling of MOSFETs and the resulting circuit density growth lead inevitably to a further increase of power consumption of CMOS integrated circuits recently. Therefore, for optimizing the performance, simply knowing that CMOS devices may use less power than equivalent devices from other technologies does not help much. It is necessary to understand the relationship between switching characteristics, integration density, and power dissipation in terms of MOSFET dimensions.

#### ■ Switching Characteristics

Realistic benchmarking of the switching delay for CMOS circuits is essential to quantify technology requirements in order to continue its historical scaling trend. In the research stage, it is important to establish the connection of the device-level targets with circuit-level performance. In 1995, M. Bohr has proposed a MOSFET speed metric as an approximated gate delay [1.6]. This metric assumes a transistor circuit as shown in Figure 1.7. This circuit can be easily imagined from Figure 1.5 (b) or (c). Transistor A and B are identical. The gate delay is defined as the time it takes node C to make a voltage swing equal to  $V_{DD}$ . The only capacitance on node C is the gate capacitance  $C_G$  of transistor B, which is defined as gate area times gate oxide capacitance per unit area ( $C_{ox}$ ). It is important to note that physical gate length  $L_G$  as opposed to electrical channel length  $L_{eff}$  is used to calculate  $C_G$  because  $L_G$  will include both channel and overlap capacitance. The on-state drive current  $I_{ON}$  of transistor A charges or discharges this capacitor. The gate delay can thus be approximated by the equation:

$$\tau \approx \frac{C_G \times V_{DD}}{I_{ON}}. \quad (1.8)$$

Historically, this expression (1.8) has been widely used as a benchmark of the

MOSFET speed [1.7]. This is because one can easily quantify the relative performance without fabricating a circuit. The only information needed from a MOSFET to estimate its  $CV/I$  gate delay is  $V_{DD}$ ,  $L_G$ ,  $I_{ON}$ , and  $C_{ox}$ . The equation (1.8) can be rewritten by using the equation (1.3):

$$\tau \approx \frac{(C_{ox}WL_G) \times V_{DD}}{\mu_{eff} C_{ox} \frac{W}{L_{eff}} \frac{(V_{DD} - V_T)^\alpha}{2m}} = (L_{eff} + 2L_{ov})L_{eff} \frac{2m}{\mu_{eff}} \frac{V_{DD}}{(V_{DD} - V_T)^\alpha}, \quad (1.9)$$

where  $L_{ov}$  is the gate overlap length and the power of  $\alpha$  ( $1 < \alpha < 2$ ) indicates the degree of velocity saturation in short-channel MOSFETs. It is clear that the gate delay is strongly depends on the gate length. This is a reason that  $I_{ON}$  enhancement as a function of the gate length is often used as a metric of a MOSFET speed. Note that this gate delay is independent on the gate width because both  $C_G$  and  $I_{ON}$  are linearly proportional to the gate width.

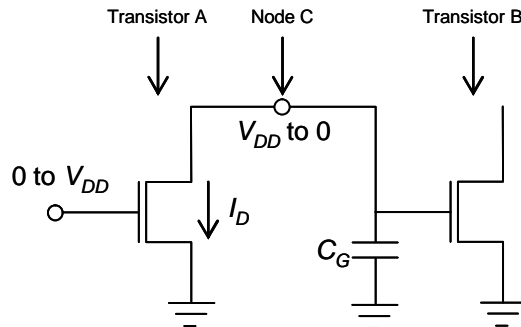


Figure 1.7  $CV/I$  performance metric [1.6].

However, in actual CMOS circuits, the load capacitance is not so simple. The difference of geometrical dependence among each capacitance sources leads to the gate delay estimation error. Here we discuss an effect of the gate width independent components. When the gate capacitance in the equation (1.8) is replaced by a lumped load capacitance  $C_L$ , the equivalent circuit can be modified as shown in Figure 1.8. The load capacitance can separate three major components.

1. The output capacitance  $C_{out}$  that results from the drain diffusion of the driving transistor A.
2. The input capacitance  $C_{in}$  that is the gate capacitance of the transistor B being

driven by the transistor A, including the intrinsic and the overlap components.

3. The wiring capacitance  $C_{wire}$  that results from interconnects to the gates being driven.

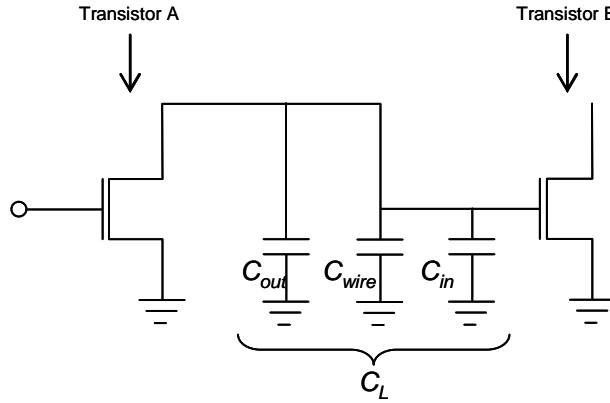


Figure 1.8 Equivalent circuit with wiring capacitance.

In general, the output of a transistor may drive more than one stage. In that case, the fan-out  $FO$  is 2, 3, ..., which means that each inverter in the chain is driving 2, 3, ... stages in parallel. The lumped load capacitance  $C_L$  thus can be written by

$$C_L = C_{out} + C_{wire} + C_{in} \times FO. \quad (1.9)$$

Here  $C_{out}$  and  $C_{in}$  are linearly proportional to the gate width, while  $C_{wire}$  is independent on that. The gate delay of the equation (1.8) then can be rewritten by the equation (1.9):

$$\begin{aligned} \tau &\approx \frac{C_L \times V_{DD}}{I_{ON}} = \frac{(C_{out} + C_{wire} + C_{in} \times FO) \times V_{DD}}{I_{ON}} \\ &= \frac{(C_{out} + C_{in} \times FO) \times V_{DD}}{I_{ON}} + \frac{C_{wire} \times V_{DD}}{I_{ON}} \\ &= \frac{C_L(W) \times V_{DD}}{I_{ON}} + \frac{C_{wire} \times V_{DD}}{I_{ON}}, \end{aligned} \quad (1.10)$$

where  $C_L(W)$  is the gate width dependent capacitance, which consists of the p-n junction capacitance and the gate capacitance including the intrinsic and overlap components. Since both  $C_L(W)$  and  $I_{ON}$  are linearly proportional to the gate width, the gate width effect is canceled out in the first term. On the other hand, the second term has the gate width dependence. As the gate width increases, the delay decreases. However, the

reduction in the delay must be traded off against the increased area (and power) when the width is increased.

Moreover, accuracy of the  $CV/I$  metric in approximating delay time is degraded as device scaling progresses [1.8–1.11]. The problem of the  $CV/I$  metric is that the MOSFETs in a real CMOS logic gate chain usually do not operate at the bias point ( $V_{GS} = V_{DS} = V_{DD}$ ) which gives  $I_{ON}$  because an inverter is driven by output from a previous stage whose waveform has a finite rise or fall time associated with it as shown in Figure 1.9. The peak current is typically 80–90% of maximum on-current  $I_{ON}$  at  $V_G = V_{DS} = V_{DD}$ . The exact percentage depends on the detailed device parameters such as mobility, velocity saturation, short-channel effects and series resistance. In particular, the contribution of drain-induced barrier lowering (DIBL) due to the short-channel effects has been pointed out as shown in Figure 1.9 (b) [1.8–1.11]. The difference of  $I_{DS}$ – $V_{DS}$  curves between with and without a degraded DIBL results in different bias-point trajectories during switching. Though  $I_{ON}$  is kept at the same level, the inverter chain built by devices with the degraded DIBL switches at a lower speed. To evaluate of the delay of a short-channel MOSFET, it is important to consider both the current level and the DIBL.

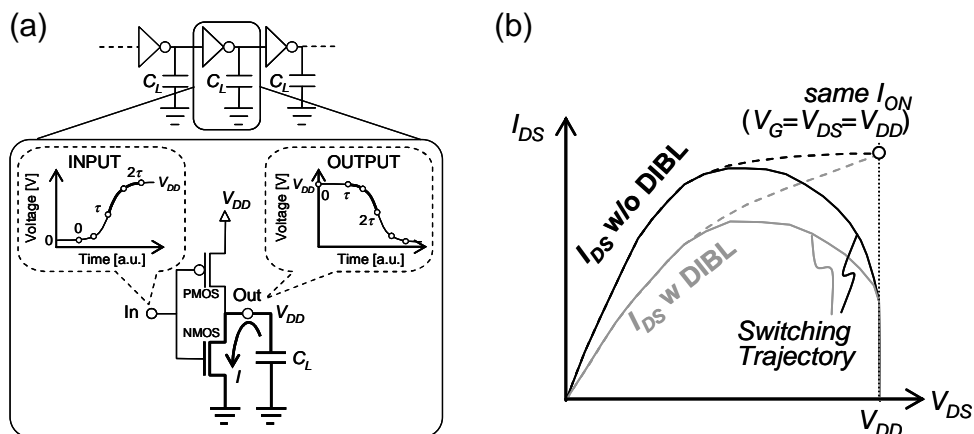


Figure 1.9 (a) Operation of a CMOS inverter in inverter chain. (b)  $I_{DS}$ – $V_{DS}$  curve and trajectories with and without a degraded DIBL for nMOSFET [1.11].

■ **Integration density**

Integration density means that what number of MOSFETs is fabricated on a chip. As shown in Figure 1.1 (a), the number has been dramatically increased in the last forty years owing to MOSFET area scaling. Figure 1.10 shows a sample layout of a CMOS inverter based on lambda-based design rules [1. 15]. The lambda unit is fixed to half of the minimum available lithography of the technology, typically the minimum gate length ( $L_G=2\lambda$ ). The layout clearly shows that the source/drain active area occupies a large area in a MOSFET, which is determined by the source/drain length and the gate width. The former is limited by the feature size of the process technology used (e.g. contact size, space between contact and gate poly). The latter depends on the carrier mobility ratio between n- and pMOSFET and the current level needed. Regarding the integration density, the key consideration is how to obtain high current level in smaller gate width as the feature size is fixed.

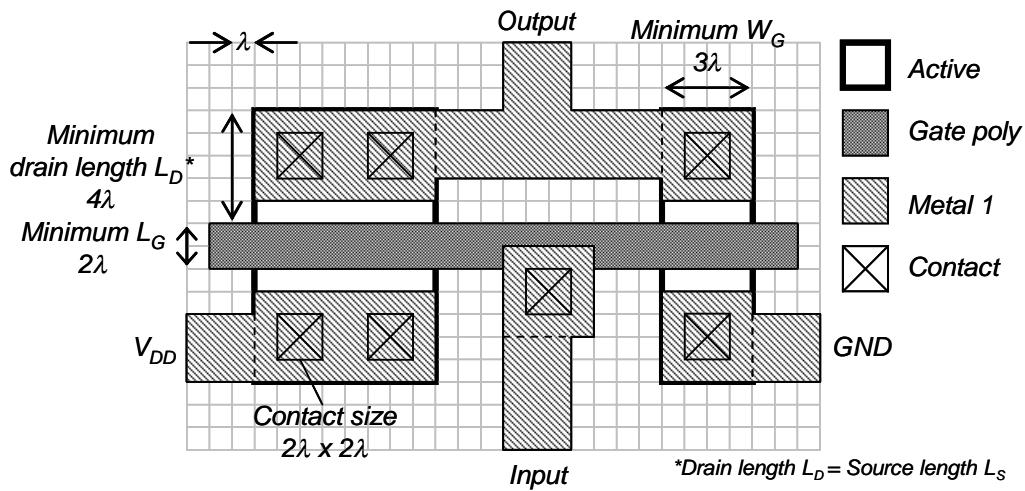


Figure 1.10 Layout of a CMOS inverter based on lambda-based design rules [1. 15]

■ **Power Consumption**

There are three major sources of power consumption in digital CMOS circuits which are summarized in the following equation [1.12]:

$$\begin{aligned}
 P_{consum} &= P_{switching} + P_{short-circuit} + P_{leakage} \\
 &= \alpha f_{clk} C_L V_{DD}^2 + I_{sc} V_{DD} + I_{leak} V_{DD}
 \end{aligned}
 \tag{1.11}$$

The first term represents the switching component of dynamic power, where  $C_L$  is the load capacitance,  $f_{clk}$  is the clock frequency, and  $\alpha$  is the node transition activity factor (the average number of times the node makes a power consuming transition in one clock period). The second term is due to the direct-path short circuit current,  $I_{sc}$ , which arises when both the n- and pMOSFET are simultaneously active, conducting current directly from supply to ground. Finally, the leakage component of static power is negligible in principle. This is one of the primary advantages of CMOS system. CMOS circuits do not dissipate power if they are not switching.

However, the continuing MOSFET scaling and the resulting circuit density growth has led to unacceptable level of static power consumption recently. Figure 1.11 shows the power consumption for CMOS logic circuits. As MOSFETs get smaller with each new process technologies, their channel lengths become shorter and the static power consumption increases over the dynamic power consumption. Nowadays, reduction of the static power consumption has become a major challenge for deep submicron CMOS. Total static power consumption can be obtained as

$$P_{static} (= P_{leakage}) = n \sum I_{leak} \times V_{DD} = n(I_{subth} + I_{gate} + I_{GIDL}) \times V_{DD}, \quad (1.12)$$

where  $n$  is the number of transistors in the off-state,  $I_{gate}$  is the gate tunneling current, and  $I_{GIDL}$  is the gate-induced drain leakage (GIDL) current. The leakage currents can be divided in to three main groups:  $I_{subth}$ ,  $I_{gate}$ , and  $I_{GIDL}$ . The increase of  $I_{subth}$  is due to the nonscaling effects and short-channel effects (see in Section 1.2). The increase of  $I_{gate}$  is due to the aggressively scaled  $t_{ox}$  which causes exponential increase of the tunneling current when the  $t_{ox}$  is scaled down to less than 2 nm as shown in Figure 1.11. This gate leakage can be reduced by replacing gate silicon dioxide ( $\text{SiO}_2$ ) to high- $\kappa$  material. Practically, high- $\kappa$  technology has been introduced to the 45 nm process technology microprocessor since 2007 by Intel Corporation [1.13]. The  $I_{GIDL}$  is caused by band-to-band tunneling in the gate-to-drain overlap region when a large gate-to-drain voltage is biased and the band bending then is larger than the silicon band gap. Lightly doped drain (LDD) structure has been studied as a solution for the GIDL [1.14, 1.15]. Figure 1.12 shows the summary of leakage current components. In actual fact, the



off-state leakages become more and more problematic in a scaled MOSFET (as explained in detail in Section 1.2).

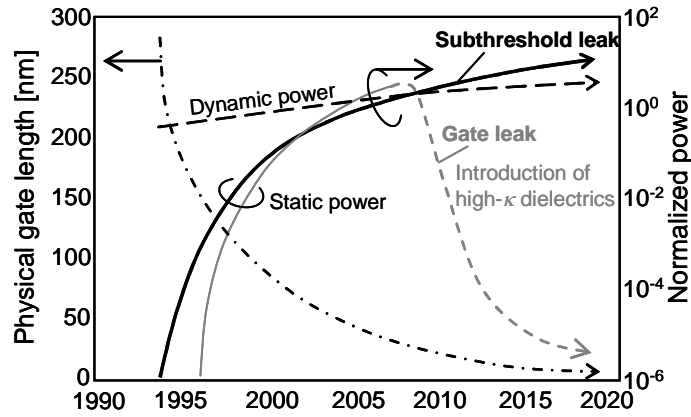


Figure 1.11 Sources of leakage current increase as the technology causes gate lengths to shrink. Data from ITRS [1.6]

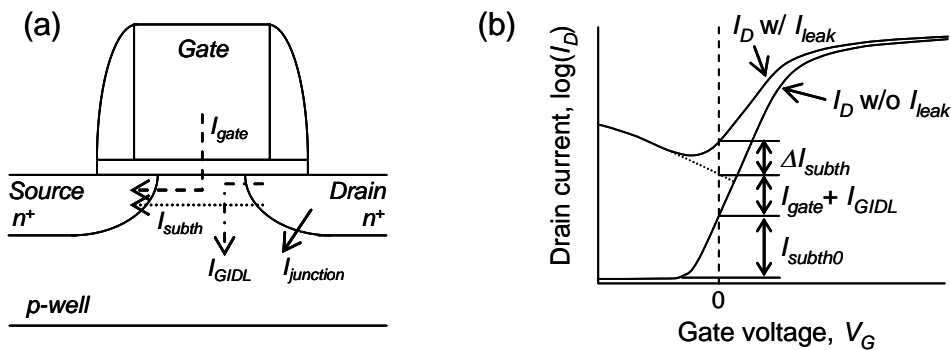


Figure 1.12 (a) Leakage current components in a nMOSFET, (b)  $I_D$ - $V_G$  curves with and without leakage currents.  $I_{subth0}$  is the initial subthreshold current, while  $\Delta I_{subth}$  is the added current due to the short-channel effects.

In this section, we discussed the basic MOSFET operation, the scaling method, and the CMOS performance indexes. CMOS LSI has been developed owing to the diminishing size of MOSFET. Especially, the impact on the gate length and width to CMOS performances was discussed in the latter half. To improve the whole performance, we have to consider the switching characteristics, the integration density,

and the power dissipation at a same time. The diminishing gate length contributes the gate delay reduction, while causing the power dissipation increase due to the short-channel effects. On the other hand, the diminishing gate width can reduce device area leading to higher integration density, while causing the gate delay increase if the gate width independent capacitances are not negligible. To make the most of the geometrical effects, the key issues will be summarized to the following two points:

1. How can we suppress the short-channel effects?
2. How can we increase the effective gate width in a given layout area?

In the next section, we will discuss the short-channel effects in detail.

## **1.2 SHORT-CHANNEL MOSFET**

Short-channel MOSFETs differ in many important aspects from long-channel devices. This section covers the features of short-channel devices that especially are important for current MOSFETs.

### **1.2.1 Short-Channel Effects**

The key difference between a short-channel and a long-channel MOSFET is that the field pattern in the depletion region of a short-channel MOSFET is two-dimensional. In other words, the gradual-channel approximation breaks down for short-channel devices. The two-dimensional field pattern arises from the proximity of source and drain regions. The source-drain distance is comparable to the MOS depletion width in the vertical direction, and the source-drain potential has a strong effect on the band bending over a significant portion of the device. This phenomenon will cause the device parameter changes which can be summarized as follows: (1)  $V_T$  roll-off, (2) subthreshold swing degradation, and (3) DIBL degradation.

#### **■ Threshold voltage roll-off**

One way to describe it is to consider the net charge (ionized acceptors or donors) in the depletion region of the device. The field lines terminating on these fixed charges



The voltage-doing transformation (VDT) has been proposed to replace the influence of the lateral drain–source field by an equivalent reduction in channel doping concentration [1.17, 1.18]. On the basis of this model, the threshold voltage roll-off can be written as follows:

$$SCE \equiv |\Delta V_T| = 0.64 \frac{\epsilon_s}{\epsilon_{ox}} EI \times \Phi_D \quad (1.14)$$

where

$$EI = \left( 1 + \frac{x_j^2}{L_{eff}^2} \right) \frac{t_{ox}}{L_{eff}} \frac{W_{dm}}{L_{eff}} \quad (1.15)$$

is the Electrostatic Integrity for planar bulk MOSFET,  $\epsilon_s$  is the semiconductor permittivity, and  $\epsilon_{ox}$  is the oxide permittivity. The VDT was proven to be successful in describing the  $V_T$  roll-off for all CMOS technologies from CMOS 1.2  $\mu\text{m}$  down to CMOS 65 nm based on a comparison to numerical simulations and experimental data.

#### ■ Subthreshold swing degradation

The physics of the short-channel effect can be understood from a different angle by considering the potential barrier at the surface between the source and drain, as shown in Figure 1.14. Under off conditions, this potential barrier prevents electron current from flowing to the drain. The surface potential is mainly controlled by the gate voltage. When the gate voltage is below the threshold voltage, there are only a limited number of electrons injected from the source over the barrier and collected by the drain (subthreshold current). In the long-channel case, the potential barrier is flat over most part of the channel. Source and drain fields only affect the very ends of the channel. As the channel length is shortened, however, the source and drain fields penetrate deeply into the middle of the channel, which lowers the potential barrier between the source and drain as shown Figure 1.14 (b). The region of maximum potential barrier shrinks to a single point near the center of the channel. This causes a substantial increase of the subthreshold current.

Here the equation 1.5 for the subthreshold swing for long-channel devices, which comes from the direct derivation of the drain current expression, can be rewritten as a

function of the surface potential  $\psi_s$ ,

$$S.S. = \frac{kT}{q} \ln(10) \cdot \left( \frac{\partial V_G}{\partial \psi_s} \right) = \frac{kT}{q} \ln(10) \cdot \left( 1 + \frac{1}{C_{ox}} \frac{\partial Q_B}{\partial \psi_s} \right), \quad (1.16)$$

It is clear that the potential barrier lowering in short-channel device will have an impact on subthreshold swing. On the basis of the VDT model, the subthreshold swing behavior with the gate length can be rewritten as follows [1.18]:

$$S.S. = \frac{kT}{q} \ln(10) \cdot \left[ 1 + \frac{1}{C_{ox}} \frac{\partial Q_B}{\partial \psi_s} + \frac{\epsilon_s}{\epsilon_{ox}} \frac{t_{ox}}{L_{eff}} \frac{x_j}{L_{eff}} \left( 1 + \frac{3}{4} \frac{W_{dm}}{L_{eff}} \right) \sqrt{1 + 2 \frac{V_{DS}}{\Phi_D}} \right]. \quad (1.17)$$

Figure 1.15 shows the subthreshold swing calculated by using MASTAR MOSFET modeling software based on the VDT model [1.19]. It is clear that the subthreshold swing increases as decreasing the gate length.

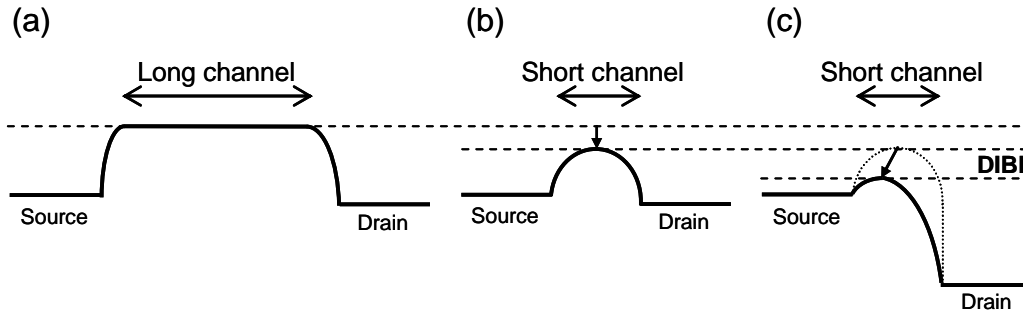


Figure 1.14 Surface potential lowering due to the short-channel effects: (a) a long-channel MOSFET, (b) a short-channel MOSFET at low drain bias, (c) a short-channel MOSFET at high drain bias.

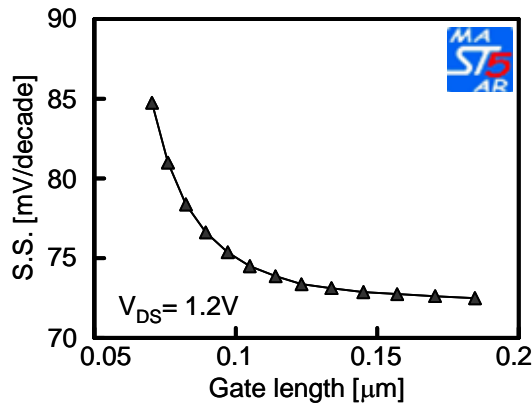


Figure 1.15 Subthreshold swing calculated by using MASTAR MOSFET modeling software [1.19]:  $N_a = 10^{18} \text{ cm}^{-3}$ ,  $x_j = 30 \text{ nm}$ ,  $t_{ox} = 1.3 \text{ nm}$ ,  $V_{DD} = 1.2 \text{ V}$ ,  $W = 1 \mu\text{m}$ .

■ **Drain-induced barrier lowering**

When a high drain voltage is applied to a short-channel device, the barrier height is lowered even more, and the point of maximum barrier also shifts toward the source end as shown in Figure 1.14 (c). The lowering of the source barrier causes an injection of extra carriers, thereby increasing the current substantially. As a result, the threshold voltage decreases. This effect is referred to as drain-induced barrier lowering (DIBL). On the basis of the VDT model, the DIBL behavior can be rewritten as follows [1.18]:

$$DIBL = 0.80 \frac{\epsilon_s}{\epsilon_{ox}} EI \times V_{DS} . \quad (1.18)$$

Figure 1.15 shows the DIBL calculated by using MASTAR MOSFET modeling software based on the VDT model [1.19]. The DIBL increases in short-channel MOSFET as well as the subthreshold swing.

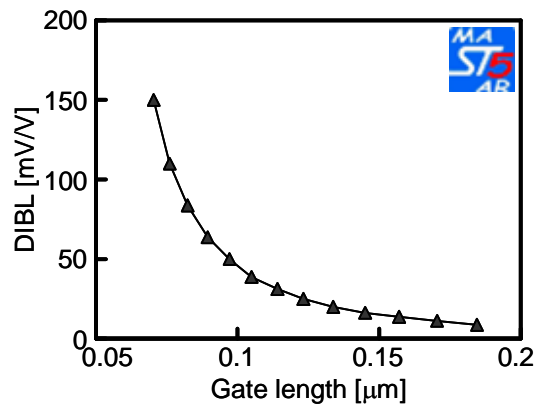


Figure 1.16 DIBL calculated by using MASTAR MOSFET modeling software [1.19]:  $N_a=10^{18} \text{ cm}^{-3}$ ,  $x_j=30 \text{ nm}$ ,  $t_{ox}= 1.3 \text{ nm}$ ,  $V_{DD}= 1.2 \text{ V}$ ,  $W=1 \mu\text{m}$ .

Consequently, the threshold voltage for a short-channel device can be rewritten as follows:

$$V_T = V_{Tlong} - SCE - DIBL , \quad (1.19)$$

where  $V_{Tlong}$  is the threshold voltage in a long-channel device. Figure 1.17 shows the threshold roll-off calculated by using MASTAR MOSFET modeling software based on the VDT model [1.19].

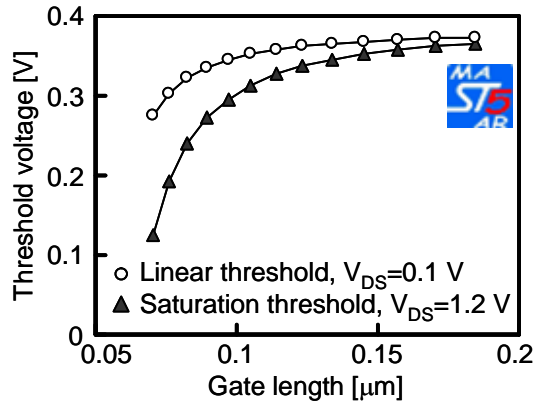


Figure 1.17  $V_T$  roll-off calculated by using MASTAR MOSFET modeling software [1.19]:  $N_a=10^{18} \text{ cm}^{-3}$ ,  $x_j=30 \text{ nm}$ ,  $t_{ox}=1.3 \text{ nm}$ ,  $V_{DD}=1.2 \text{ V}$ ,  $W=1 \mu\text{m}$ .

Here, we should reconsider the static power consumption in short-channel CMOS logic gates. The increase of off-state current is the sum of these short-channel effects as shown in Figure 1.18. The subthreshold current for a short-channel device can be rewritten as follows [1.18]:

$$\text{Log}(I_{subth}) = \text{Log}(I_{Tr}) - (V_{Tlong} - SCE - DIBL) / SS, \quad (1.20)$$

where  $I_{Tr}$  is the transistor current corresponding to the threshold voltage. With gate length and threshold voltage scaled down the subthreshold leakage current increases exponentially. In order to suppress the increase, it is clear that we have to avoid increasing the three factors: SCE, DIBL, and  $SS$ . Now, we can easily understand which physical parameters are important from the equations 1.14, 1.15, 1.17, and 1.18;  $t_{ox}/L_{eff}$ ,  $x_j/L_{eff}$ , and  $W_{dm}/L_{eff}$ . Thinning of gate oxide was one of the easiest solutions technologically. Until now, aggressive scaling of the gate oxide ( $\text{SiO}_2$ ) thickness thus has continued. However, this resulted in rapid increase of the tunneling current when the gate oxide thickness is scaled down to less than 2 nm as shown in Figure 1.11. This gate leakage can be reduced by replacing gate silicon dioxide ( $\text{SiO}_2$ ) to high- $\kappa$  material. To form shallow junctions, the use of Silicon-On-Insulator (SOI) wafer is one of the most effective solutions. The source/drain junction depth in SOI thin body device is terminated by the buried oxide. Moreover, the thin body thickness can limit the maximum depletion-layer depth. These devices will be discussed in section 1.4.

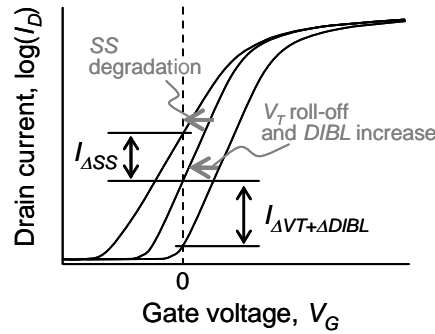


Figure 1.18 Off-current increase due to the short-channel effects.

### 1.2.2 Source/Drain Series Resistance in short-channel MOSFET

In the discussion of MOSFET current thus far, it was assumed that the source and drain regions were perfectly conducting. In reality, as the current flows from the channel to the terminal contact, there is a voltage drop in the source and drain regions due to the finite silicon receptivity and metal contact resistance as shown in Figure 1.19.

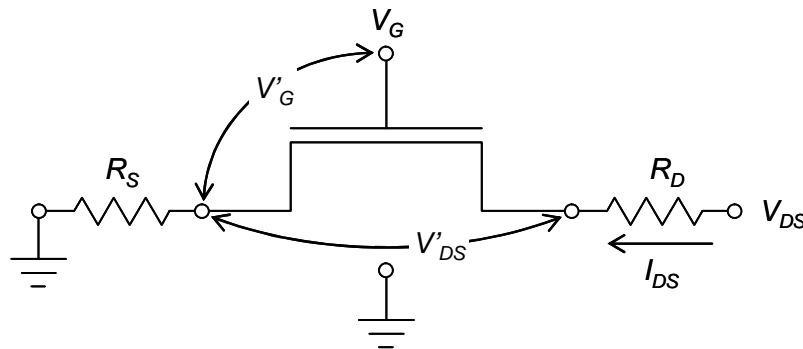


Figure 1.19 Equivalent circuit of MOSFET with source and drain resistance [1.4].

In a long-channel device, the source–drain parasitic resistance is negligible compared with the channel resistance. In a short channel device, however, the source–drain series resistance can be an appreciable fraction of the channel resistance and can therefore cause significant current degradation. The most severe current degradation by series resistance occurs in the linear region (Low  $V_{DS}$ ) when the gate voltage is high because the MOSFET channel resistance is the lowest under such bias conditions. The MOSFET current in the saturation region is least affected by the resistance degradation of



source–drain voltage,  $I_{DS}$  is essentially independent of  $V_{DS}$  in saturation. The saturation current is only affected through gate–source voltage degradation by voltage drop between the source contact and the source end of the channel [1.4]:

$$V'_G = V_G - R_S I_{DS} . \quad (1.21)$$

In aggressively scaled MOSFETs, however, the saturation current degradation becomes more and more problematic. Figures 1.20 and 1.21 show the on-current degradations due to the source/drain series resistance. This degradation implies that further improvements in  $I_{ON}$  by shortening the gate length cannot be expected when the channel resistance becomes comparable to the source and drain resistance. Nowadays, the source/drain series resistance is a major concern for the MOSFET scaling. Shallow junctions in the source/drain regions are needed to minimize the short-channel effects as discussed in subsection 1.2.1. ITRS predicts that source/drain extension junction depth below sub-50 nm CMOS will be scaled further down around 10 nm to maintain acceptable short channel performance, but this may lead to a high series resistance problem [1.7, 1.20]. In other words, further down-scaling without improvement of  $I_{ON}$  is meaningless even if short-channel effects are completely suppressed by introducing shallow junction technologies (e.g. source/drain extension, SOI wafer, etc.). It is important to design MOSFET structure effective in suppression of both short-channel effects and source/drain resistance.

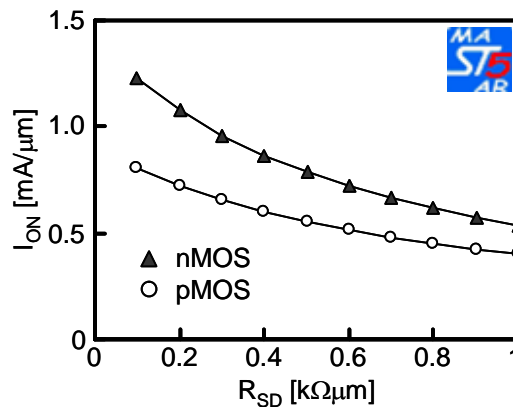


Figure 1.20 On-currents as a function of source/drain series resistance. All plots are calculated by using MASTAR MOSFET modeling software [1.19]:  $N_a=10^{18}cm^{-3}$ ,  $t_{ox}= 1.3$  nm,  $V_{DD}= 1.2$  V,  $L_G=50$  nm,  $W=1\mu m$ .

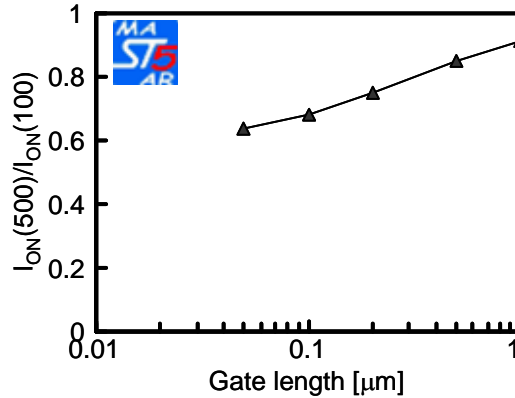


Figure 1.21 On-current lowering ratio of  $R_{SD} = 500 \Omega \cdot \mu\text{m}$  to  $100 \Omega \cdot \mu\text{m}$  as a function of gate length. All plots are calculated by using MASTAR MOSFET modeling software [1.19]:  $N_a = 10^{18} \text{cm}^{-3}$ ,  $t_{ox} = 1.3 \text{nm}$ ,  $V_{DD} = 1.2 \text{V}$ ,  $W = 1 \mu\text{m}$ .

### 1.2.3 Carrier Transport Mechanisms in short-channel MOSFET

In short channel devices, the short-channel effects become problematic. On the other hand, carrier transport also has gate length dependence. Precise understanding of correlation between low-lateral-field mobility and high-lateral field velocity, which is more directly related to on-current, is important. In analyzing the carrier transport mechanisms depending on the gate length, we go back to the general equation of the saturation current. We start with the generalized form

$$I_{ON} \approx WqN_{INV}^{source} \cdot v_s \quad (1.22)$$

where  $q$  is the elemental charge,  $N_{INV}^{source}$  is the inversion charge density near the source edge, and  $v_s$  is the average carrier velocity near the source edge [1.21]. While  $qN_{INV}$  is simply determined by the maximum value at the source as  $C_{ox}(V_G - V_T)$ , the determination mechanism of  $v_s$  is dependent on the gate length. So the only critical parameter is  $v_s$ . Figure 1.22 shows the schematic diagrams of carrier transport models to determine  $I_{ON}$ . In long-channel MOSFETs, the carrier mobility  $\mu$  is the solely important factor in determining the velocity  $v$ . The  $v$ - $\mu$  relationship is given by  $v = \mu * E_{lateral}$ , where  $E_{lateral}$  is the lateral electric field, as shown in Figure 1.23. However, the linear  $v$ - $\mu$  relationship breaks down when the gate length becomes shorter. As the lateral

electric field is increased, the average carrier velocity and the average carrier energy increase as well. When the carrier energy increases beyond the optical phonon energy, the probability of emitting an optical phonon increases abruptly. This mechanism causes the carrier velocity to saturate with increasing electric field as shown in Figure 1.24 [1.22, 1.23]. As velocity saturation phenomenon begins to occur,  $\mu$  dependence of  $v$  becomes weaker. As far as carrier scattering events in the channels sufficiently occur and the stationary transport dominate the carrier transport, the carrier transport model as shown in Figure 1.22 (a) basically holds even under the existence of velocity saturation.

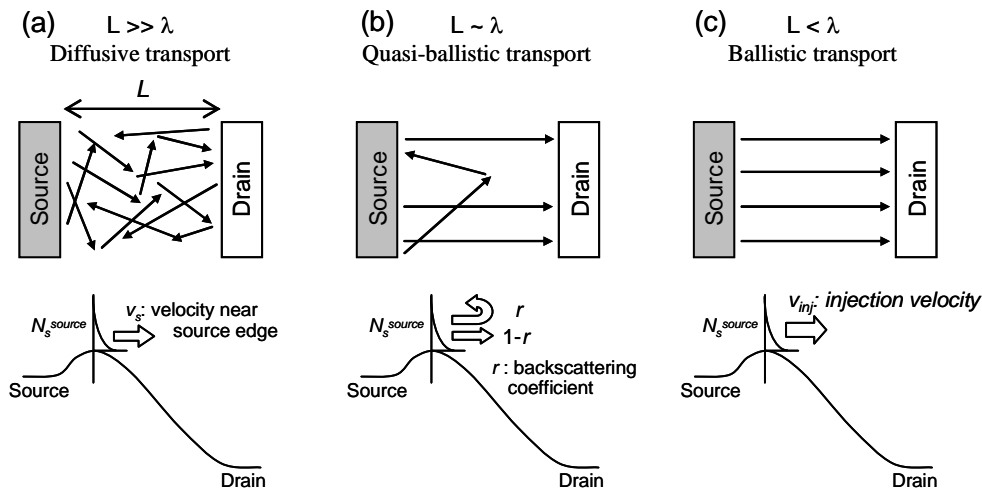


Figure 1.22 Schematic diagrams of carrier transport models to determine  $I_{ON}$ . (a) Conventional transport model. (b) Quasi-ballistic transport model. (c) Full-ballistic transport model [1.24, 1.25].

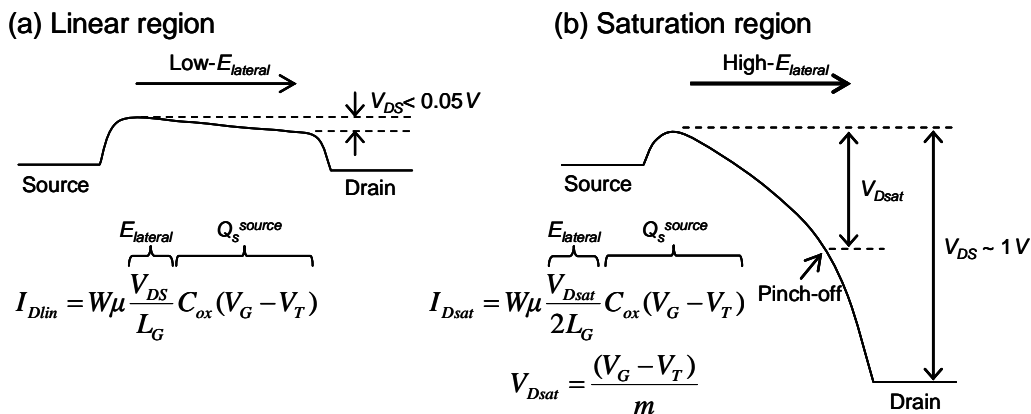


Figure 1.23 Channel potential profiles under conditions of carrier mobility  $\mu$  and velocity  $v$ . (a) Linear region. (b) Saturation region.

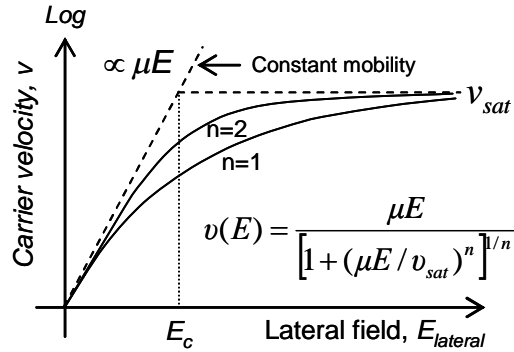


Figure 1.24 Velocity–field relationship for electrons ( $n=2$ ) and holes ( $n=1$ ) by the empirical form inserted [1.22]. The critical field  $E_c = v_{sat}/\mu$ .

As the channel length becomes shorter, nonstationary transport becomes more dominant, where sufficient numbers of scattering events do not occur inside the channels. This situation, as shown in Figure 1.22 (b), has been formulated as quasi-ballistic transport by Lundstrom *et al.* [1.21]:

$$I_{ON} = qN_{INV}^{source} \cdot v_{inj} \cdot \frac{1-r}{1+r}, \quad (1.23)$$

where  $v_{inj}$  is the injection velocity at the top of the barrier near the source edge, and  $r$  is the backscattering rate near-source region. The fraction  $r$  of the carriers are scattered back to the source, as shown in Figure 1.22 (b). Hence the effective velocity of carriers at the barrier, called virtual source velocity, is determined by this fraction. Lundstrom’s theory uses assumption that only scattering events that take place in the vicinity of the virtual source are responsible for backscattering of carriers to the source. Once a carrier passes the point where the potential has dropped by  $kT/q$  from the barrier top, the probability of return to the source is negligible. Hence, the  $r$  depends on the ration between the backscattering mean free path of carriers,  $\lambda$ , and the distance over which the potential drops by the thermal voltage, the so-called critical length of scattering,  $l$ :

$$r = \frac{l}{l + \lambda}. \quad (1.24)$$

The notion of mobility in short-channel devices, where the scattering mean free path is comparable to the channel length, is subject of controversy. However, a

phenomenological mobility can always be extracted at low  $V_{DS}$ . Assuming that the mobility is constant across the channel and that the carriers at the top of the barrier are in a near-equilibrium condition, Rahman related this mobility to the backscattering mean free path by matching the low  $V_{DS}$  drift-diffusion equation with the MOSFET scattering model [1.22]:

$$\lambda = \left( \frac{2\mu}{v_\theta} \frac{kT}{q} \right) \frac{\mathfrak{F}_0(\eta_F)}{\mathfrak{F}_{-1}(\eta_F)}, \quad (1.25)$$

where  $v_\theta$  is the ballistic velocity of carriers which in the non-degenerate limit is equal to the thermal velocity,  $\eta_F = (E_F - \varepsilon)/kT$  is the reduced Fermi energy,  $\varepsilon$  is the minimum band energy, and  $\mathfrak{F}_n$  is the Fermi integral of the  $n$ th order. This equation (1.25) means that in order for the ballistic efficiency to increase, the low-field mobility should be increased. Since  $r$  is related to  $\mu$ , the enhancement of mobility can be still important in increasing  $I_{ON}$  under quasi-ballistic transport regime.

Furthermore, when channel length becomes much shorter, probably down to less than 10 nm in Si MOSFETs, and no carrier-scattering events occur inside the channel, the carrier transport is dominated by full ballistic transport, as shown in Figure 1.22(c). Here,  $I_{ON}$  in MOSFETs under this ballistic transport, which have also been formulated by Natori [1.24], is simply represented by

$$I_{ON} = qN_s^{source} \cdot v_{inj}. \quad (1.26)$$

Thus the enhancement of  $v_{inj}$  is necessary to increase  $I_{ON}$  of ballistic MOSFETs, while the carrier mobility loses its meaning.

Recently, the  $v$ - $L_G$  relationships have been experimentally investigated to clarify the effectiveness of  $\mu$  enhancement to improve  $I_{ON}$  [1.27]. Figure 1.25 shows the experimental results of  $L_G$  dependence of velocity. It was found the velocity is not completely saturated even below  $L_G = 50$  nm and still increases with a slope of  $L_G^{-0.45}$ . This can be assigned to the velocity overshoot phenomenon near the source edge due to contribution of quasi-ballistic carriers. Note that the mobility enhancement is still effective at  $L_G = 30$  nm.

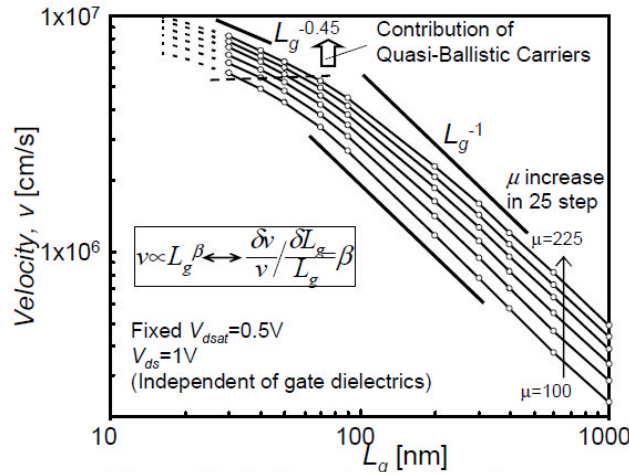


Figure 1.25  $L_G$  dependence of velocity with  $\mu$  as parameter [1.27].

In this section, we discussed several effects in short-channel MOSFETs. To suppress the off leakage current caused by the short channel effects, the minimization of  $t_{ox}$ ,  $x_j$ , and  $W_{dm}$  is effective. However, the shallow junction leads to  $I_{ON}$  degradation due to the high source/drain series resistance. To avoid this trade-off, it is important to design MOSFET structure effective in suppression of both short-channel effects and source/drain resistance. Moreover, although  $\mu$  dependence of  $v$  becomes weaker in short-channel MOSFETs, the  $\mu$  enhancement can be still important in increasing  $I_{ON}$  under quasi-ballistic transport regime.

### 1.3 KEY TECHNOLOGIES TO IMPROVE MOSFET PERFORMANCE

This section introduces some solutions and challenges to continue the scaling toward purpose of this thesis. First, we consider a leading edge of CMOS technology. Figure 1.26 shows cross section of n- and pMOSFETs for 32 nm technology fabricated by Intel Corporation in 2009 [1.28]. The key device features are summarized in Table 1.2. The foundation of the 32 nm process technology is the second generation high- $\kappa$ /metal gate MOSFET to suppress the short-channel effects without increasing gate leakage. The equivalent oxide thickness (EOT) of the high- $\kappa$  dielectric has been

reduced from 1.0 nm on 45 nm to 0.9 nm on the 32 nm process while gate length has been reduced to 30 nm. Using a replacement metal gate flow, that is a gate-last process, enables stress enhancement techniques to be in place before removing the poly gate from the transistor. This 32 nm technology also uses 4<sup>th</sup> generation SiGe strained silicon for pMOSFET resulting in linear drive current exceeding nMOSFET. Moreover, the raised S/D regions and 2<sup>nd</sup> generation trench contacts technologies enables reduced S/D access resistance.

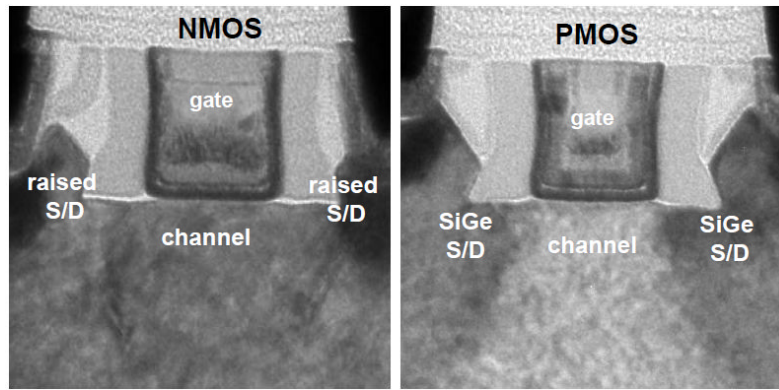


Figure 1.26 Cross section of Intel's NMOS and PMOS with 4th generation strained silicon, 2nd generation high- $\kappa$ /metal gate, and raised S/D regions for 32 nm technology [1.28].

Table 1.2 Key device features of Intel 32 nm logic technology [1.28].

	NMOS	PMOS	
			<ul style="list-style-type: none"> <li>❑ 30 nm gate length with 112.5 nm contacted gate pitch</li> </ul>
$L_G$ [nm]	30	30	<ul style="list-style-type: none"> <li>❑ 2<sup>nd</sup> generation high-<math>\kappa</math>/metal gate                             <ul style="list-style-type: none"> <li>✓ 0.9 nm EOT</li> <li>✓ Replacement metal gate approach                                     <ul style="list-style-type: none"> <li>- Enables stress enhancement techniques</li> </ul> </li> <li>✓ Replacement high-k approach                                     <ul style="list-style-type: none"> <li>- Improved performance</li> </ul> </li> </ul> </li> </ul>
EOT [nm]	0.9	0.9	
$I_{Dsat}$ [mA/mm] $V_{GS}=V_{DS}=1.0V$	1.62	1.37	
$I_{Dlin}$ [mA/mm] $V_{GS}=1.0V$ $V_{DS}=0.05V$	0.231	0.240	<ul style="list-style-type: none"> <li>❑ 4<sup>th</sup> generation SiGe strained silicon PMOS device                             <ul style="list-style-type: none"> <li>✓ Increased Ge concentration</li> <li>✓ Closer proximity to channel for enhanced mobility</li> </ul> </li> </ul>
$I_{OFF}$ [nA/mm]	100	100	<ul style="list-style-type: none"> <li>❑ Raised NMOS S/D region                             <ul style="list-style-type: none"> <li>✓ Improved external resistance</li> </ul> </li> </ul>
$V_{Tsat}$ [V]	0.115	-0.18	
DIBL [mV/V]	~200	~200	<ul style="list-style-type: none"> <li>❑ 2<sup>nd</sup> generation trench contacts                             <ul style="list-style-type: none"> <li>✓ Reduced contact resistance</li> <li>✓ Used as local interconnects</li> </ul> </li> </ul>
SS [mV/dec]	~100	~100	

These technologies are introduced along the performance enhancement strategies mentioned above. Note that most of these technologies are needed due to the short-channel effects. For a given short channel characteristic and constant  $I_{OFF}$ , the gate length scaling through increased threshold voltage degrades drive current. The improvement in drive current owing to the shorter gate length is offset by the reduction in overdrive voltage ( $V_G - V_T$ ). Therefore, mobility enhancement becomes a key engineering factor with minimal impact to leakage. Moreover, suppression of the short-channel effects demands rapid development of high- $\kappa$ /metal gate technology to minimize EOT and the raised S/D technology to obtain low S/D resistance with shallow junction as well as several channel doping technologies. In addition, increasing the impurity concentration in the channel region is also necessary to suppress the short-channel effects. However, this causes degradation of carrier mobility due to impurity scattering, which result in obstruction to increase the drive current [1.29]. Moreover, random dopant fluctuation in such short channel results in variation of the threshold voltage [1.30]. To continuously improve CMOS performance, comprehensive reforms of the CMOS scaling strategy will be required to achieve high immunity of short-channel effects.

### **1.3.1 Gate-All-Around Silicon Nanowire MOSFET**

Fully-depleted (FD) silicon-on-insulator (SOI) MOSFETs are considered as possible successors for bulk MOSFETs because their thin body dimensions provide geometric electrostatic confinement for controlling short-channel effects as well as less stringent requirements of EOT scaling over conventional bulk Si. Figure 1.27 shows a typical planar FDSOI MOSFET structure. The thin layer of silicon is separated from buried oxide (BOX) film, thus electrically isolating the devices from the underlying silicon substrate. In this structure, the source and drain junction capacitance is almost entirely eliminated. Here FD structure means that the silicon body film is thin enough that the entire film is depleted before the threshold condition is reached. An important merit of SOI technology is that it provides the cornerstone for new FD device structures such as multi-gate MOSFETs, which includes more than one gate into a single device as



shown in Figure 1.28 [1.32].

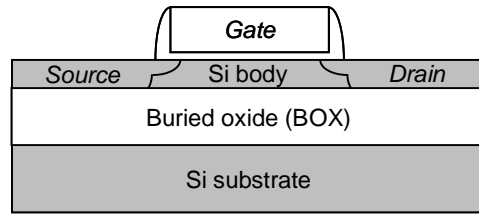


*Figure 1.27 Cross-section of a planar FDSOI MOSFET.*

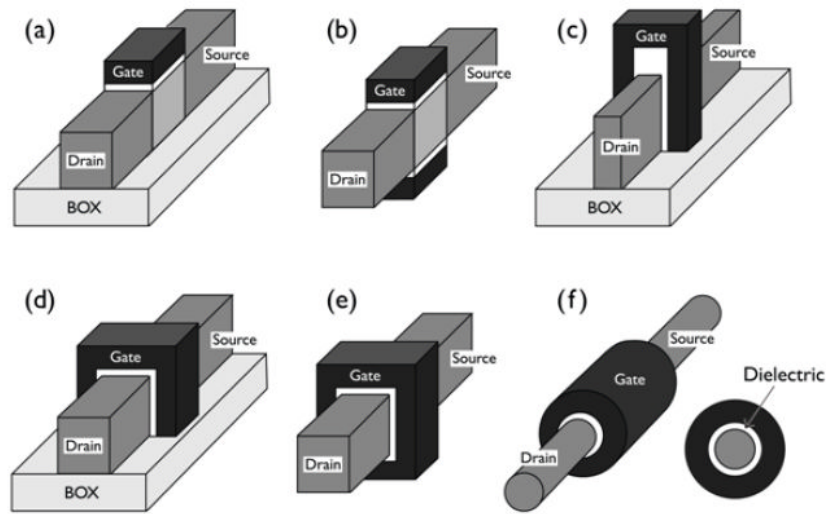


*Figure 1.28 Various SOI device: (a) Single gate SOI FET, (b) double gate planar SOI FET, (c) double gate non-planar FinFET, (d) tri-gate FET, (e) quadruple-gate (or gate-all-around) FET, and gate-all-around (or surrounding gate) FET (nanowire FET).*

Figure 1.29 displays the electric field lines from the drain in different MOSFET structures. More is the penetration of field lines from the drain towards the source, greater is the interference of the drain on the function of the gate. The conventional MOSFET geometry, shown in Figure 1.29 (a), can hardly be scaled down because of strong permeation of the field lines towards the source. The behavior of FDSOI structure of Figure 1.29 (b) is not encouraging because the buried oxide does not terminate the drain field lines. Only in the double-gate (DG) MOSFET structure shown in Figure 1.29 (c), the field lines are not able to reach near the source [1.31]. Hence the effect of the drain field on the channel is minimized providing far superior scalability.

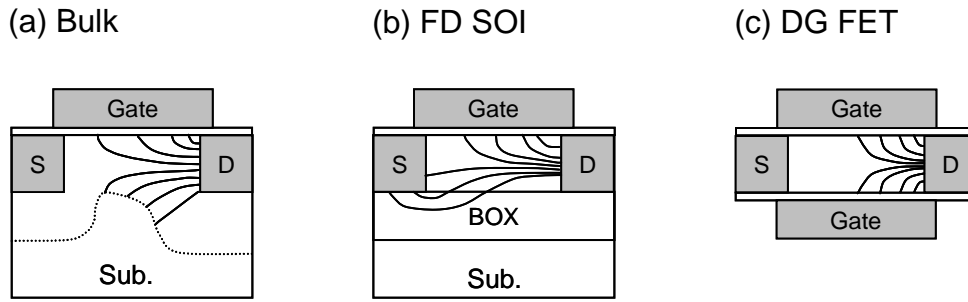


Figure 1.29 Illustration of electric field lines from drain of different device types: (a) bulk, (b) FD SOI, and (c) double gate (DG).

Yan *et al.* proposed a unique scaling theory for double-gate SOI MOSFETs as a design guideline [1.33]. According to their theory, the device should be designed maintaining

$$\alpha = \frac{L_{eff}}{2\lambda}, \quad (1.27)$$

where  $\lambda$  is the so-called natural length which governs the influence of lateral field on the channel potential and depends on device geometry and boundary conditions. To This natural length is an easy guide for choosing device structure and parameters, and has simple physical meaning that a small natural length corresponds to superb short channel effect immunity. Table 1.3 shows the natural length for different gate configurations [1.32]. Here a small  $\alpha$  gives degraded short-channel effect immunity. For instance, to achieve  $SS < 75$  mV/decade and  $DIBL < 50$  mV/V,  $\alpha$  needs to be larger than 2.2 for all devices when the gate oxide is 2 nm and the channel doping concentration is  $1 \times 10^{18} \text{cm}^{-3}$  [1.34]. Figure 1.30 shows the maximum allowed silicon film thickness (and device width in a four-gate device with  $W = t_{si}$ ) to avoid short-channel effects [1.35]. As a consequence, gate-all-around (GAA) silicon nanowire MOSFETs (SNWTs) have the best short-channel effect immunity among all the FDSOI architectures for the same body dimensions. The experimental data reported by Bangsaruntip *et al.* also shows better short-channel immunity for GAA SNWTs than that of FDSOI by as shown in Figure 1.31 [1.36].

Table 1.3 Natural length in devices with different geometries [1.32].

Single gate	$\lambda_1 = \sqrt{\frac{\epsilon_{si} t_{si} t_{ox}}{\epsilon_{ox}}}$
Double gate	$\lambda_2 = \sqrt{\frac{\epsilon_{si} t_{si} t_{ox}}{2\epsilon_{ox}}}$
Quadruple gate (square section)	$\lambda_4 \cong \sqrt{\frac{\epsilon_{si} t_{si} t_{ox}}{4\epsilon_{ox}}}$
Surrounding gate (circular section)	$\lambda_o \cong \sqrt{\frac{2\epsilon_{si} t_{si}^2 \ln(1 + 2t_{ox}/t_{si})}{16\epsilon_{ox}} + \epsilon_{ox} t_{si}^2}$

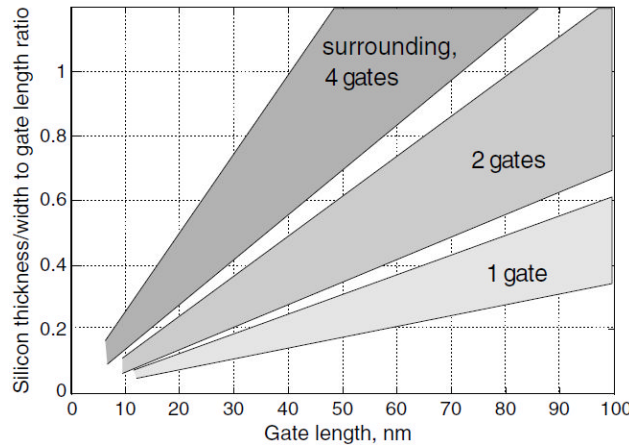


Figure 1.30 Maximum allowed Si thickness and device width vs. gate length to avoid short-channel effects in single-, double- and quadruple-gate SOI MOSFETs [1.35].

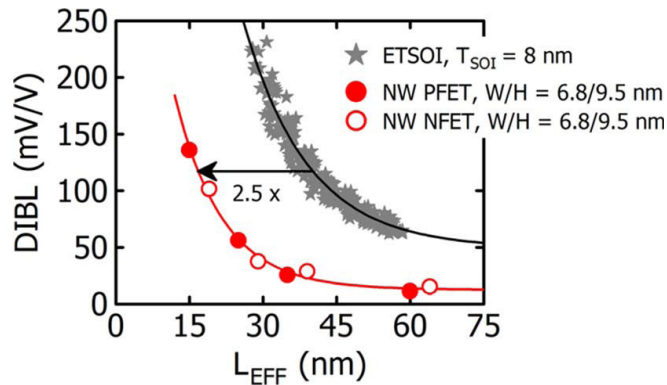


Figure 1.31 Comparison of DIBL of elliptical GAA SNWTs (width  $W = 6.8$  nm and height  $H = 9.5$  nm) and single-gate ETSOI FETs (SOI thickness  $t_{si} = 8$  nm) with similar body dimensions. [1.36].

### 1.3.2 Vertically-Stacked Channel MOSFET

In a GAA SNWT, the current drive is essentially equal to the sum of the currents flowing along all the interfaces covered by the gate electrode [1.32]. To drive large currents, multi-finger pattern are need as shown in Figure 1.32. When an ideal current transport (without corner effect, volume inversion effect, and so on) are considered in rectangular GAA SNWT, the current level depends on the width  $W_{NW}$  and height  $H_{NW}$ , of a nanowire, the top and bottom surface mobility  $\mu_{top}$ , the side surface mobility  $\mu_{side}$ , and the number of the nanowires for given layout area. The on-current in GAA SNWT with multi-finger are given by

$$I_{ON}^{nanowire} = n \times (2W_{NW}\mu_{top} + 2H_{NW}\mu_{side}) \frac{C_{ox}}{L_{eff}} \frac{(V_{DD} - V_T)^\alpha}{2m}, \quad (1.28)$$

where  $n$  is the number of the nanowires and the power of  $\alpha$  ( $1 < \alpha < 2$ ) indicates the degree of velocity saturation in short-channel MOSFETs. Considering a nanowire pitch  $W_{pitch}$ , the current per unit device width is given by

$$\frac{I_{ON}^{nanowire}}{W_{pitch}} = \frac{I_{ON}^{planar}}{W} \cdot \frac{2W_{NW}\mu_{top} + 2H_{NW}\mu_{side}}{\mu_{top}W_{pitch}}, \quad (1.29)$$

where  $I_{ON}^{planar}$  is the current in the single-gate, planar MOSFET occupying the same area as the multi-finger device as shown in Figure 1.32.

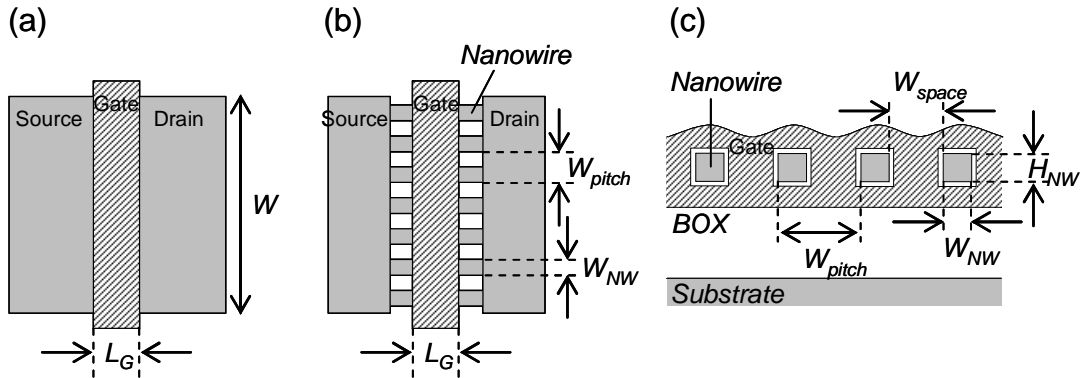


Figure 1.32 MOSFET layout; (a) planar MOSFET, (b) GAA SNWT with multi-finger, and (c) cross-section of GAA SNWT.

To realize a benefit of the multi finger layout, the current of GAA SNWT per layout surface normalized to planar MOSFET are calculated with several dimensions.

Here we assume the nanowire direction of  $\langle 110 \rangle$ , the top surface orientation of (100), and the sidewall surface orientation of (110). The values of the mobility for (100) and (110) used thus are  $300 \text{ cm}^2/\text{Vs}$  and  $150 \text{ cm}^2/\text{Vs}$ , respectively. Figure 1.33 shows its nanowire pitch dependence. The nanowire width  $W_{NW}$  is equal to a half of the pitch width. Because of that, the currents of GAA SNWT approach to the planar one as increase the pitch. If the cross section of the nanowire is square ( $W_{NW} = H_{NW}$ ), the current is independent on the pitch, and we have  $I_{ON}^{nanowire} = 1.5x I_{ON}^{planar}$ . In actual case, since each nanowires are wrapped by the gate dielectrics and the space between them must be filled by gate metal, the space between nanowires  $W_{space}$  may need at least 15 nm. In that case, the diminishing cross-section to obtain the better short-channel effect immunity is traded off against the current density gain. When the space is equal to 15 nm, there is no gain of the current density for GAA SNWT with  $W_{NW} = 5 \text{ nm}$  and  $H_{NW} = 10 \text{ nm}$  to the planar one, for instance.

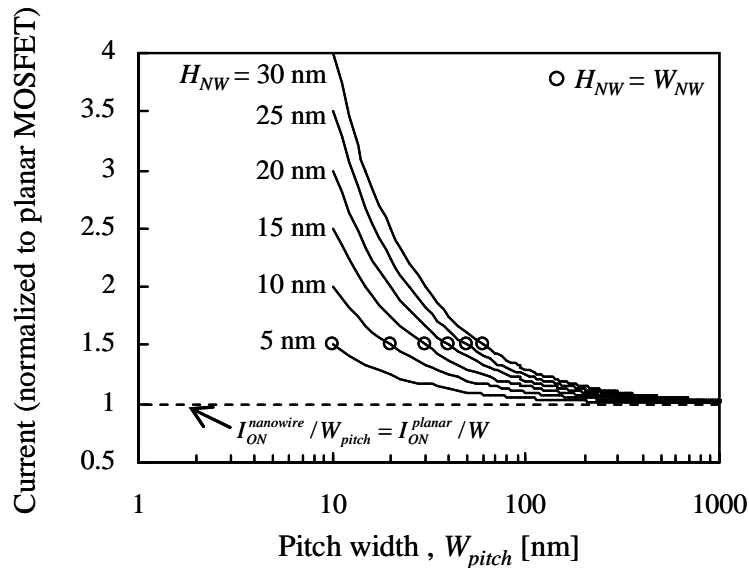


Figure 1.33 Normalized current of a rectangular GAA SNWT as a function of multi-finger pitch width.  $W_{NW} = W_{pitch}/2$ . The top interface mobility is  $300 \text{ cm}^2/\text{Vs}$  and sidewall mobility is  $150 \text{ cm}^2/\text{Vs}$ .

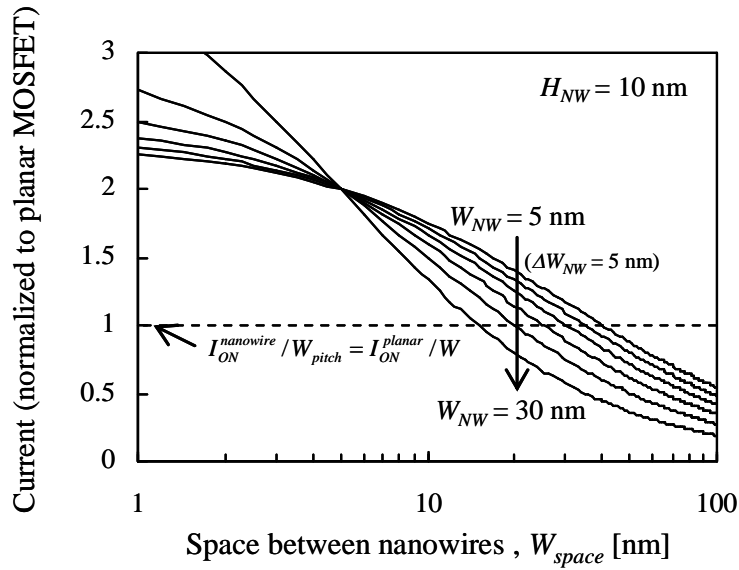


Figure 1.34 Normalized current of a rectangular GAA SNWT as a function of space between nanowires.  $H_{NW}=10$  nm. The top interface mobility is  $300$   $\text{cm}^2/\text{Vs}$  and sidewall mobility is  $150$   $\text{cm}^2/\text{Vs}$ .

To obtain larger current density per a given layout with high immunity of the short-channel effects, the vertical integration of nanowires is effective as shown in Figure 1.35. In this structure, the current density can be proportionally increased to the stacking level (three levels in the case of Figure 1.35) without the layout surface area penalty as seen in Figure 1.36. This structure enables to achieve both high integration density and low power dissipation. Note that since this current increment is due to the effective surface enlargement, the intrinsic gate delay cannot be directly reduced as discussed in Subsection 1.13. The propagation delay, however, can be improved as the interconnect capacitance becomes larger. The suppressed short channel effects are also effective to reach the ideal switching trajectory.

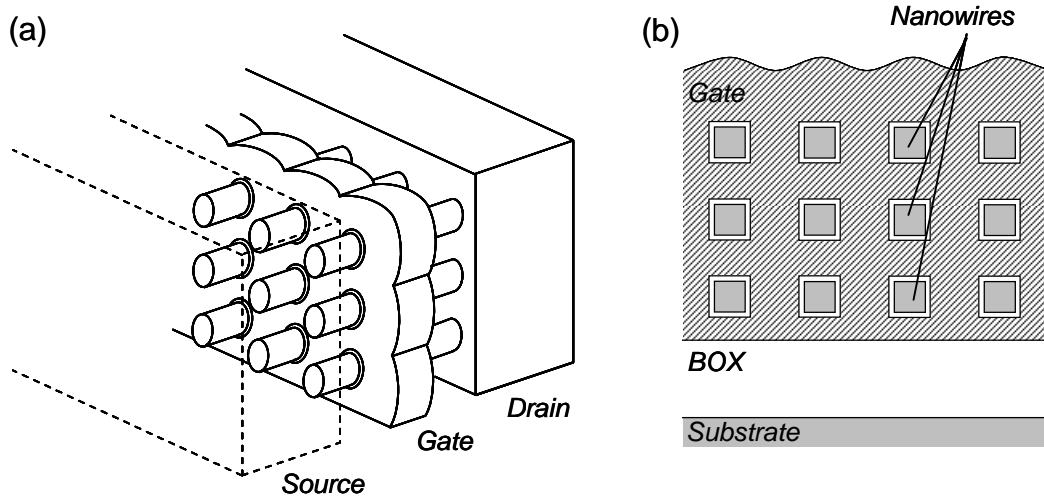


Figure 1.35 Structure of vertically-stacked GAA SNWT(a) and its cross-section (b)

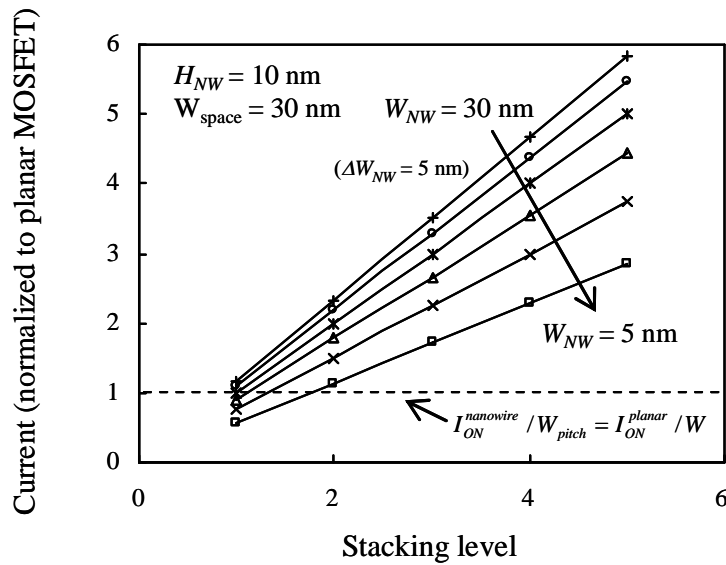


Figure 1.36 Normalized current of a rectangular GAA SNWT as a function of staking level of nanowires.  $H_{NW}=10$  nm.  $W_{space}=30$  nm. The top interface mobility is  $300$   $cm^2/Vs$  and sidewall mobility is  $150$   $cm^2/Vs$ .

## 1.4 PURPOSE AND CONTENTS OF THIS STUDY

The operation speed and integration density of a microprocessor chip have doubled every two or three years in line with Moore’s law. For each generation, in order

to achieve the target performance, prospective problems were analyzed in detail and solved by introducing new technologies. Looking back at the history, it seems that many problems result from the short-channel effects. Now we are faced with the critical issue of power dissipation due to subthreshold leakage. This power dissipation, which surpasses dynamic power consumption, can no longer be ignored. Therefore comprehensive reform of the CMOS scaling strategies is required to continuously improve speed, integration density, and power dissipation of LSI all at the same time.

The purpose of this thesis thus is to characterize vertically-stacked GAA SNWT as one of the most promising MOSFETs for future CMOS circuits. The superior immunity to short-channel effects and the high integration density can be straightforwardly expected from this structure. However, the body dimensions must be considered with drive current enhancement. In addition, it is possible that the thick source/drain regions of the vertically-stacked channel MOSFET need special treatments in the fabrication process to obtain low access resistance. As other critical issue in this type of three dimensional devices, body bias techniques are not available for power management of digital circuits. Thus the studies are classified into three issues:

- How do we achieve low access resistance with uniform doping profile in the thick source/drain regions?
- How are the carrier transport properties of vertically-stacked nanowire channels?
- How can we realize the controllability and flexibility of the threshold voltage?

Figure 1.37 shows the outline of this thesis. First, the basic device fabrication process of vertically-stacked channel structure is presented and specific technological issues are evidenced in Chapter 2. Next, the electrical characterization methods are described in detail in Chapter 3. Chapter 4 covers the studies source/drain resistance reduction technique for thick source/drain regions in vertically-stacked channel devices. Chapter 5 covers the carrier transport properties of vertically-stacked GAA SNWTs in detail, especially the dimension effects and the impacts on the fabrication process. Chapter 6 covers the studies of the threshold voltage tuning technique by the independently separated gates. The studies referred to in each chapter were done in



order to achieve CMOSFET with high performance, high integration density, and low power dissipation for future generation. Details are as follows.

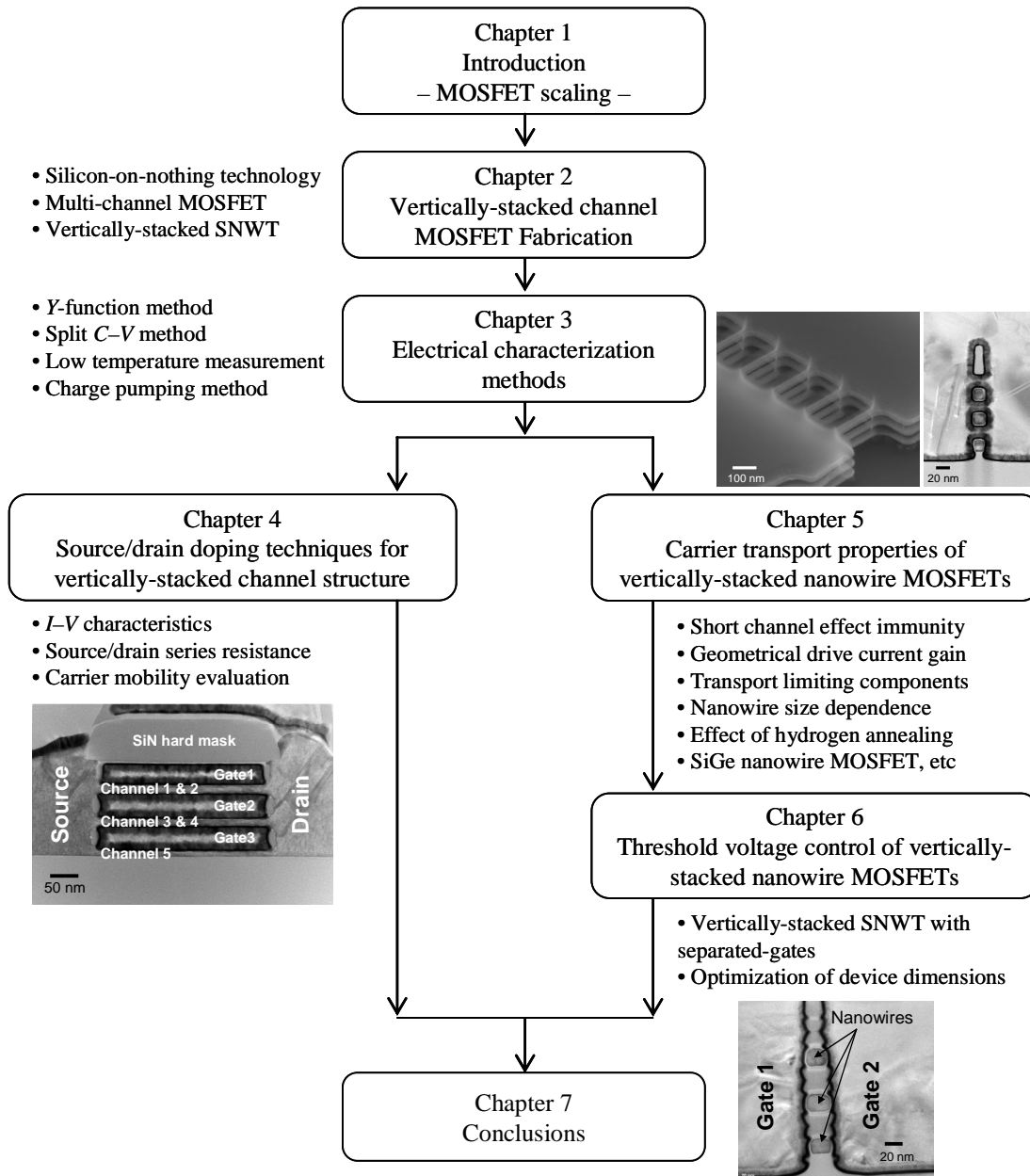


Figure 1.37 Outline of each chapter in this thesis.

**a) Source/drain doping techniques for vertically-stacked channel structure (Chapter 4)**

The reduction of parasitic access resistances serially connected at source and

drain region of MOSFETS are one of the challenging technology to meet the performance required in the roadmap as discussed in Chapter 1. The voltage drops at the resistances reduces the applied voltages at the drain and gate electrodes in the transistors, resulting in the decrease in the overdrive voltage to lower the on-current. These resistances also cause degradation in the time constant, commonly referred as RC delay, to lower the switching speed. Therefore, as the channel resistance reduces with the scaling in the gate length, the parasitic series resistance should be further reduced not to increase its proportion in the total resistance at on-state. In addition, the vertically-stacked channel structure suffers from the uniformity of the doping profile due to the thick source/drain regions.

In Chapter 4, a novel process to decrease the resistivity of the source and drain regions is presented using *in situ* doped selective epitaxial growth in combination with conventional ion-implantation as a novel process for source and drain formation. The effect of source and drain formation process on the series resistance and carrier mobility will be discussed through electrical characteristics.

***b) Carrier transport properties of vertically-stacked nanowire MOSFETs (Chapter 5)***

Recently, short channel GAA SNWTs have been successfully fabricated with diameter of less than 10 nm using several top-down CMOS compatible processes [1.37–1.39]; they showed excellent short-channel effects immunity. On the other hand, transport property degradation in SNWTs was also reported by several groups [1.40–1.42]. However, the mobility behavior when the width is reduced has been remained unclear. Carrier transport in nanowire is commonly discussed in terms of two main mechanisms; one is one-dimension transport model, and the other is a facet-dominated transport model. The former can be adapted to sub-10 nm diameter, and the latter to more than 20 nm one. In the range of between them, the mixed transport properties are expected. The range of between them is production-friendly, provided that the short-channel effects under aggressively scaled gate length are suppressed, while carrier transport model becomes complicate due to the mixed properties.

In Chapter 5, carrier transport limiting components for vertically-stacked GAA SNWTs will be discussed in detail to obtain better performance with suppressing short channel effects.

c) **Threshold voltage control of vertically-stacked nanowire MOSFETs (Chapter 6)**

Another issue for the vertically-stacked SNWTs is how to control the threshold voltage. For various CMOS applications and power management, it is important to achieve controllable and flexible threshold voltage in a transistor. As one of the possible techniques for three-dimensional devices, separated-gate structures have been proposed [1.43, 1.44]. In Chapter 5, the possibility of the flexible threshold voltage for vertically-stacked GAA SNWTs with separated gate will be discussed.

Finally, in Chapter 7, the results obtained in these studies are summarized and conclusions are presented. The perspective of vertically-stacked GAA SNWTs for future LSI applications is described.

## **1.5 REFERENCE**

- [1.1] G. E. Moore, "Cramming more components onto integrated circuits," *Electronics*, Vol. 38, No. 8, 1965.
- [1.2] Data source: <http://www.intel.com/technology/timeline.pdf>
- [1.3] G. E. Moore, "No Exponential is Forever: But "Forever" Can be Delayed!," in *ISSCC Tech. Dig.*, Feb. 2003, vol.1, pp.20–23.
- [1.4] Y. Taur and T. H. Ning, *Fundamental of Modern VLSI Devices*, 2<sup>nd</sup> edition, Cambridge University Press, 2009.
- [1.5] R. H. Dennard, F. H. Gaensslen, H-N, Yu, V. L. Rideout, E. Bassous, and A. R. LeBlanc, "Design of ion-implanted MOSFET's with very small physical dimensions," *IEEE J. Solid-State Circuits*, vol. SC-9, no. 5, pp. 256–268, 1974.
- [1.6] M. Bohr, "MOS Transistor: Scaling and Performance Trends," *Semiconductor International*, vol. 18, no. 6, pp.75–80.

- [1.7] International Technology Roadmap for Semiconductors (ITRS): <http://www.itrs.net/reports.html>
- [1.8] M. H. Na, E. J. Nowak, W. Haensch, and J. Cai, “The effective drive current in CMOS inverters,” in *IEDM Tech. Dig.*, 2002, pp. 121–124.
- [1.9] E. Yoshida, Y. Momiyama, M. Miyamoto, T. Saiki, M. Kojima, S. Satoh, and T. Sugii, “Performance Boost using a New Device Design Methodology Based on Characteristic Current for Low-Power CMOS,” in *IEDM Tech. Dig.*, 2006, pp. 195–198.
- [1.10] L. Wei, F. Boeuf, D. Antoniadis, T. Skotnicki, and H.-S. P. Wong, “Exploration of Device Design Space to Meet Circuit Speed Targeting 22nm and Beyond,” in extended abstracts of SSDM, 2009, pp.808–809.
- [1.11] T. Skotnicki and F. Boeuf, “How Can High Mobility Channel Materials Boost or Degrade Performance in Advanced CMOS,” in *VLSI Tech. Dig.*, 2010, pp. 153–154.
- [1.12] T. Sakurai, “Perspectives of power-aware electronics (Plenary),” in *Proc. ISSCC Dig. Tech. Papers*, 2003, pp. 26–29.
- [1.13] K. Mistry, C. Allen, C. Auth, B. Beattie, D. Bergstrom, M. Bost, M. Brazier, M. Buehler, A. Cappellani, R. Chau, C.-H. Choi, G. Ding, K. Fischer, T. Ghani, R. Grover, W. Han, D. Hanken, M. Hattendorf, J. He, J. Hicks, R. Huessner, D. Ingerly, P. Jain, R. James, L. Jong, S. Joshi, C. Kenyon, K. Kuhn, K. Lee, H. Liu, J. Maiz, B. McIntyre, P. Moon, J. Neiryneck, S. Pae, C. Parker, D. Parsons, C. Prasad, L. Pipes, M. Prince, P. Ranade, T. Reynolds, J. Sandford, L. Shifren, J. Sebastian, J. Seiple, D. Simon, S. Sivakumar, P. Smith, C. Thomas, T. Troeger, P. Vandervoorn, S. Williams, and K. Zawadzki, “A 45nm Logic Technology with High-k+Metal Gate Transistors, Strained Silicon, 9 Cu Interconnect Layers, 193nm Dry Patterning, and 100% Pb-free Packaging,” in *IEDM Tech. Dig.*, 2007, pp. 247–250.
- [1.14] S. A. Parke, J.E. Moon, H. C. Wann, P. K. Ko, and C. Hu, “Design for suppression of gate-induced drain leakage in LDD MOSFET’s using a quasi-two-dimensional analytical model,” *IEEE Trans. Electron Devices*, vol. 39,

- no. 7, pp. 1694–1703, 1992.
- [1.15] K. Tanaka, K. Takeuchi, and M. Hane, "Practical FinFET design considering GIDL for LSTP (Low Standby Power) devices," in *IEDM Tech. Dig.*, 2005, pp. 980–983.
- [1.16] Scalable CMOS (SCMOS) Design Rules (Based on *MOSIS* design: <http://www.mosis.com/> )
- [1.17] T. Skotnicki, G. Merckel, and T. Pedron, "The voltage-doping transformation: A new approach to the modeling of MOSFET short-channel effects," *IEEE Electron Device Lett.*, vol. 9, no. 3, pp. 109–112, 1988.
- [1.18] T. Skotnicki, C. F.-Beranger, C. Gallon, F. Boeuf, S. Monfray, F. Payet, A. Pouydebasque, M. Szczap, A. Farcy, F. Arnaud, S. Clerc, M. Sellier, A. Cathignol, J.-P. Schoellkopf, E. Perea, R. Ferrant, and H. Mingam, "Innovative Materials, Devices, and CMOS Technologies for Low-Power Mobile Multimedia," *IEEE Trans. Electron Devices*, vol. 55, no. 1, pp. 96–130, 2008.
- [1.19] *MASTAR4 Code and User Guide*. Available: <http://www.itrs.net/models.html>
- [1.20] S. Thompson, P. Packan, T. Ghani, M. Stettler, M. Alavi, I. Post, S. Tyagi, S. Ahmed, S. Yang, and M. Bohr, "Source/Drain extension scaling for 0.1mm and below channel length MOSFETs," in *Proc. Symp. VLSI Tech.*, 1998, pp. 132–133.
- [1.21] M. Lundstrom and Z. Ren, "Essential physics of carrier transport in nanoscale MOSFETs," *IEEE Trans. Electron Devices*, vol. 49, no. 1, pp. 133–141, 2002.
- [1.22] S. M. Sze and Kwok K. Ng, *Physics of Semiconductor Devices*, 3<sup>rd</sup> edition, John Wiley & Sons, Inc., Hoboken, New Jersey, 2007.
- [1.23] M. Saitoh and K. Uchida, "Universal relationship between low-field mobility and high-field carrier velocity in high- $\kappa$  and SiO<sub>2</sub> gate dielectric MOSFETs," in *IEDM Tech. Dig.*, 2006, pp. 261–264.
- [1.24] K. Natori, "Ballistic metal–oxide–semiconductor field effect transistor," *J. Appl. Phys.*, vol. 76, no. 8, pp. 4879–4890, Oct. 1994.
- [1.25] S. Takagi, T. Irisawa, T. Tezuka, T. Numata, S. Nakaharai, N. Hirashita, Y. Moriyama, K. Usuda, E. Toyoda, S. Dissanayake, M. Shichijo, R. Nakane, S. Sugahara, M. Takenaka, and N. Sugiyama, "Carrier-Transport-Enhanced Channel

- CMOS for Improved Power Consumption and Performance, ” *IEEE Trans. Electron Devices*, vol. 55, no. 1, pp. 21–38, 2008.
- [1.26] A. Rahaman and M. S. Lundstrom, “A compact scattering model for the nanoscale double gate MOSFET,” *IEEE Trans. Electron Devices*, vol. 49, no. 3, pp. 481–489, 2002.
- [1.27] K. Tatsumura, M. Goto, S. Kawanaka, and A. Kinoshita, “Correlation between low-field mobility and high-field carrier velocity in quasi-ballistic-transport MISFETs scaled down to  $L_g=30$  nm,” in *IEDM Tech. Dig.*, 2009, pp. 465–468.
- [1.28] P. Packan, S. Akbar, M. Armstrong, D. Bergstrom, M. Brazier, H. Deshpande, K. Dev, G. Ding, T. Ghani, O. Golonzka, W. Han, J. He, R. Heussner, R. James, J. Jopling, C. Kenyon, S-H. Lee, M. Liu, S. Lodha, B. Mattis, A. Murthy, L. Neiberg, J. Neiryneck, S. Pae, C. Parker, L. Pipes, J. Sebastian, J. Seiple, B. Sell, A. Sharma, S. Sivakumar, B. Song, A. St. Amour, K. Tone, T. Troeger, C. Weber, K. Zhang, Y. Luo, S. Natarajan, “High Performance 32nm Logic Technology Featuring 2nd Generation High-k + Metal Gate Transistors,” in *IEDM Tech. Dig.*, 2009, pp. 659–662.
- [1.29] S. Takagi, A. Toriumi, M. Iwase, and H. Tango, “On the Universality of Inversion Layer Mobility in Si MOSFET’s: Part I—Effects of Substrate Impurity Concentration,” *IEEE Trans. Electron Devices*, vol. 41, no. 12, pp. 2357–2362, Dec. 1994.
- [1.30] K. Nishinohara, N. Shygyo, and T. Wada, “Effects of microscopic fluctuations in dopant distributions on MOSFET threshold voltage,” *IEEE Trans. Electron Devices*, vol. 39, no. 3, pp. 634–639, Mar. 1992.
- [1.31] T. Ernst, R. Ritzenthaler, O. Faynot, and S. Cristoloveanu, “A model of fringing field in short-channel planar and triple-gate SOI MOSFETs,” *IEEE Trans. Electron Devices*, vol. 54, no. 6, pp. 1366–1375, June. 2007.
- [1.32] J. P. Coling, “Multi-gate SOI MOSFETs,” *Microelectronic Engineering*, vol. 84, pp. 2071–2076, 2007.
- [1.33] R.-H. Yan, A. Ourmazd, and L. F. Lee, “Scaling the Si MOSFET: from bulk to SOI to bulk,” *IEEE Trans. Electron Devices*, vol. 39, no. 7, pp. 1704–1710, July. 1992.
- [1.34] C.-W. Lee, S.-R.-N. Yun, C.-G. Yu, J.-T. Park, J.P. Colinge, “Device design guidelines

- for nano-scale MuGFETs,” *Solid-State Electronics*, vol. 51, pp. 505–510, 2007.
- [1.35] J. P. Coling, “Multiple-gate SOI MOSFETs,” *Solid-State Electronics*, vol. 48, pp. 897–905, 2004.
- [1.36] S. Bangsaruntip, G. M. Cohen, A. Majumdar, and J. W. Sleight, “Univesality of short-channel effects in undoped-body silicon nanowire MOSFETs,” *IEEE Electron Device Lett.* vol. 31, no. 9, pp. 903–905, Sept. 2010.
- [1.37] S. Bangsaruntip, G.M. Cohen, A. Majumdar, Y. Zhang, S. U. Engelmann, N. C. M. Fuller, L. M. Gignac, S. Mittal, J. S. Newbury, M. Guillorn, T. Barwicz, L. Sekaric, M. M. Frank, and J. W. Sleight, “High performance and highly uniform gate-all-around silicon nanowire MOSFETs with wire size dependent scaling,” in *IEDM Tech. Dig.*, 2009, pp. 297–300.
- [1.38] M. Li, K.H. Yeo, S.D. Suk, Y.Y. Yeoh, D.-W. Kim, T.Y. Chung, K. S. Oh, and W.-S. Lee, “Sub-10 nm gate-all-around CMOS nanowire transistors on bulk Si substrate,” in *VLSI Tech. Dig.*, 2009, pp. 94–95.
- [1.39] G. Bidal, F. Boeuf, S. Denorme, N. Loubet, J.L. Huguenin, P. Perreau, D. Fleury, F. Leverd, S. Lagrasta, S. Barnola, T. Salvetat, B. Orlando, R. Beneyton, L. Clement, R. Pantel, S. Monfray, G. Ghibaudo, and T. Skotnicki, “High velocity Si-nanodot: a candidate for SRAM applications at 16 nm node and below,” in *VLSI Tech. Dig.*, 2009, pp. 240–241.
- [1.40] S. D. Suk, M. Li, Y. Y. Yeoh, K. H. Yeo, K. H. Cho, I. K. Ku, H. Cho, W. J. Jang, D.-W. Kim, D. Park, and W.-S. Lee, “Investigation of nanowire size dependency on TSNWFET,” in *IEDM Tech. Dig.*, 2007, pp. 891–894.
- [1.41] M. Saitoh, Y. Nakabayashi, H. Itokawa<sup>1</sup>, M. Murano, I. Mizushima<sup>1</sup>, K. Uchida, and T. Numata, “Short-Channel Performance and Mobility Analysis of <110>- and <100>-Oriented Tri-Gate Nanowire MOSFETs with Raised Source/Drain Extensions,” in *VLSI Tech. Dig.*, 2010, pp. 169–170.
- [1.42] J. Chen, T. Saraya, K. Miyaji, K. Shimizu, and T. Hiramoto, “Experimental Study of Mobility in [110]- and [100]-Directed Multiple Silicon Nanowire GAA MOSFETs on (100) SOI,” in *VLSI Tech. Dig.*, 2008, pp. 32–33.
- [1.43] Y. X. Liu, M. Masahara, K. Ishii, T. Tsutsumi, T. Sekigawa, H. Takahima, H.

Yamauchi and E. Suzuki, “Flexible Threshold Voltage FinFETs with Independent Double Gates and an Ideal Rectangular Cross- Section Si-Fin Channel”, in *IEDM Tech. Dig.*, 2003, pp. 986–989.

- [1.44] C. Dupré, A. Hubert, S. Bécu, M. Jublot, V. Maffini-Alvaro, C. Vizioz, F. Aussenac, C. Arvet, S. Barnola, J.-M. Hartmann, G. Garnier, F. Allain, J.-P. Colonna, M. Rivoire, L. Baud, S. Pauliac, V. Loup, T. Chevolleau, P. Rivallin, B. Guillaumot, G. Ghibaud, O. Faynot, T. Ernst, and S. Deleonibus, “ 15nm-diameter 3D Stacked Nanowires with Independent Gate Operation:  $\Phi$ FET,” in *IEDM Tech. Dig.*, 2008, pp. 749–752.



# **CHAPTER 2**

## ***VERTICALLY- STACKED CHANNEL MOSFETS FABRICATION***

# CHAPTER 2 CONTENTS

## **2 Vertically-Stacked Channel MOSFET Fabrication**

- 2.1 Silicon-On-Nothing Technology
- 2.2 Process Step Overview for Multi-Channel MOSFET
- 2.3 Process Step Overview for Vertically-Stacked Nanowire MOSFET
- 2.4 Key Steps
  - 2.4.1 High-k/Metal Gate Stacks
  - 2.4.2 SiGe Epitaxy and Etching
- 2.5 Conclusions
- 2.6 References

## 2.1 SILICON-ON-NOTHING TECHNOLOGY

Silicon-On-Nothing (SON) architecture have been proposed allowing extremely thin buried oxides and Silicon films to be fabricated and thereby better resisting to short-channel effects [2.1–2.3]. The process is based on the use of a sacrificial SiGe layer that is selectively removed versus the silicon as shown in Fig. 2.1. The tunnel under the silicon film is then filled with the oxide. Silicon film and buried oxide are defined by epitaxy that opens access to extremely thin films. Extensions are physically limited by the silicon film thickness preserving a good control of shorts channel effects. In the same time, source and drain remain in continuity with the substrate, limiting self-heating and lowering  $R_{SD}$ . The use of thin buried oxide allows the control of the fringing field. Moreover, this architecture is co-integrable with bulk one [2.3].

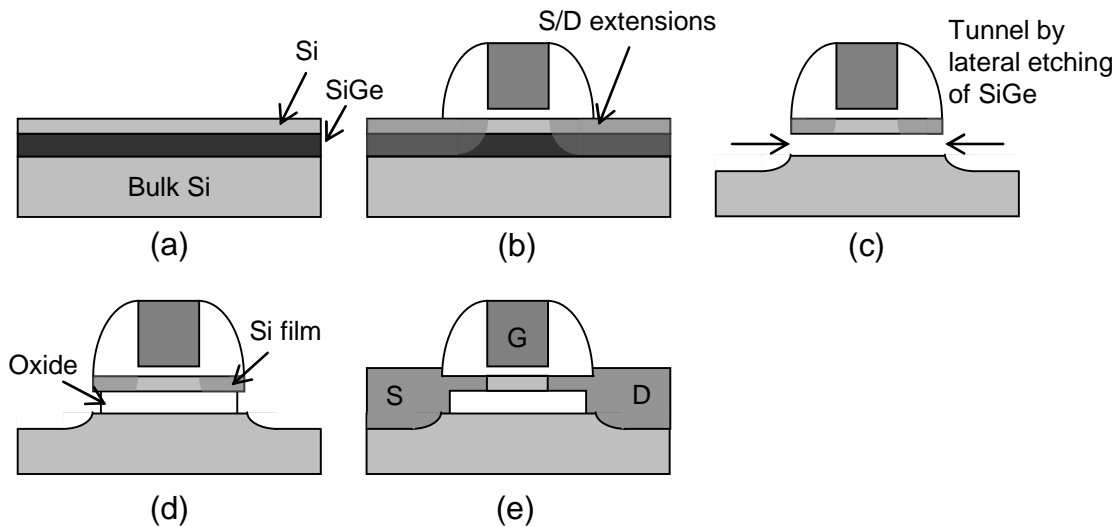


*Figure 2.1 Fabrication process of the SON MOSFET: (a) epitaxy of SiGe and Si layers on isolated bulk wafer; (b) conventional CMOS process steps until formation of the nitride spacers; (c) formation of the shallow trenches in the S/D regions and formation of the tunnel under the Si film; (d) filling the tunnel with oxide (optional step); (e) selective epitaxy of S/D regions, implantation and RTA.*

Vertically-stacked channel structure has been derived from SON and GAA concepts. The use of sacrificial SiGe layers enables silicon channel to be piled up. In this study, two types of stacked channel MOSFETs were fabricated; one is multi-channel MOSFET, another is vertically-stacked nanowire FET.

## **2.2 PROCESS STEP OVERVIEW FOR MULTI-CHANNEL MOSFET**

The fabrication process of MCFETs, which is based on the principles developed for Silicon-On-Nothing FETs, has been developed by Bernard [2.2–2.4]. Figure 2.2 shows an overview of the MCFET process flow. First, a (25-nm-Si and 30-nm-Si<sub>0.8</sub>Ge<sub>0.2</sub>) superlattice structure was epitaxially grown on a 20-nm thick SOI substrate (step 1). The grown Si layers will be used as channels for MCFETs. 5nm of high-temperature oxide (HTO) and 80nm of silicon nitride (Si<sub>3</sub>N<sub>4</sub>) are deposited as a hard mask on the top of the stack. After a gate photolithography, the superlattice is then anisotropically etched down to the bottom SOI layer (step 2). Since  $L_G$  is defined at this etching step, a vertical etching profile is an important requirement for this technology in order to suppress the variability of the  $L_G$  among the stacked Si channels. To introduce internal spacers, the SiGe layers are partially etched selectively to the Si ones (step 2.1). The depth of the SiGe recess determines the thickness of the future internal spacers. Then, HTO and Si<sub>3</sub>N<sub>4</sub> layers are deposited in the cavities with a thickness ratio optimized for the following spacers etch (step 2.2 and 2.3). An anisotropic/isotropic etch sequence of the deposited dielectrics allows one to access the silicon layers for further S/D epitaxy (step 2.4). After the wet cleaning to remove entirely the dielectrics on the sides of silicon layers, crystalline Si S/D was selectively grown with a natural “flat” shape induced by the presence of the internal spacers (step 3). The S/D were then ion-implanted. The channel width was defined by the active-area patterning and etching, giving access to the SiGe layers. The SiGe layers are selectively removed using pure CF<sub>4</sub> at high pressure and low microwave power in a remote plasma tool. The high- $k$ /metal gate stack (HfO<sub>2</sub>/TiN/N<sup>+</sup> poly-Si) was deposited in the obtained cavities. A

second gate etch is subsequently carried out followed by the formation of external silicon nitride spacers to avoid any short-cut between the gate and the S/D. After the dopant activation anneal, the top of S/D are silicided (with nickel) to reduce the series resistances, followed by a standard back-end-of-the-line (BEOL) process (for contacts and interconnections).

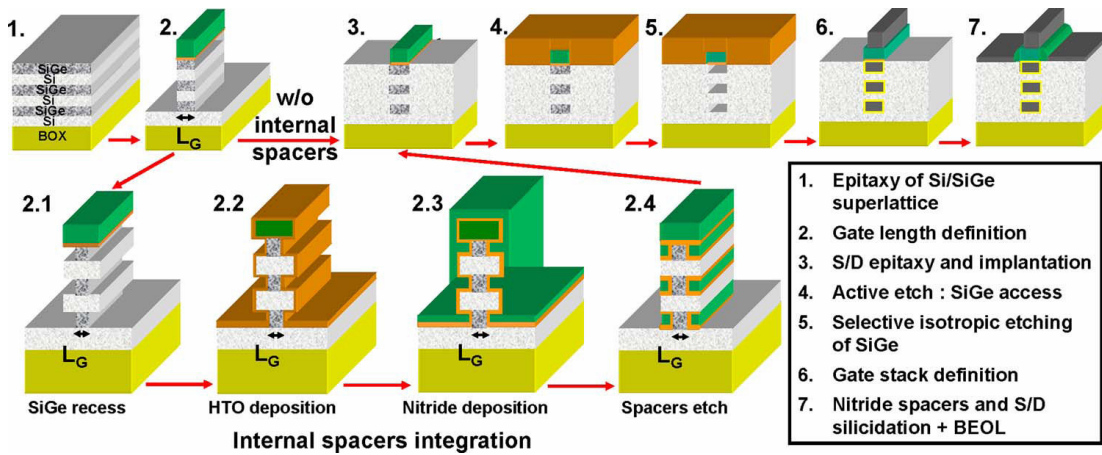


*Figure 2.2 MCFET fabrication process overview [2.2].*

Figure 2.3 shows the cross-sectional transmission electron microscopy (TEM) images of the fabricated MCFETs along the Si channel and width direction. Here, two SiGe/Si alternating layers, resulting in five Si channels in parallel, were designed for fabrication. Channels 1 and 2 are activated at the top and bottom interfaces of the superior silicon island, whereas channels 3 and 4 have similar formations within the intermediate Si island. Channel 5 is responsible for conduction as the top of the original Si film. The sixth possible channel, which can be activated at the bottom of the Si film by substrate (back-gate) biasing, is not investigated in this work. The resulting channel thickness was 10 nm for all channels. The measured equivalent oxide thickness (EOT) in inversion was  $\sim 2.5$  nm. The gate lengths of the MCFETs range from 500 to 70 nm.

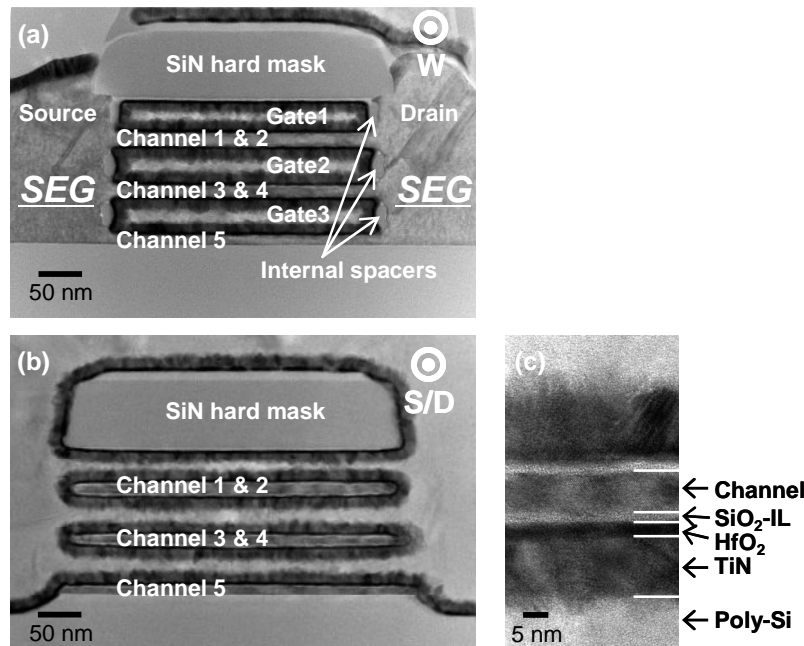
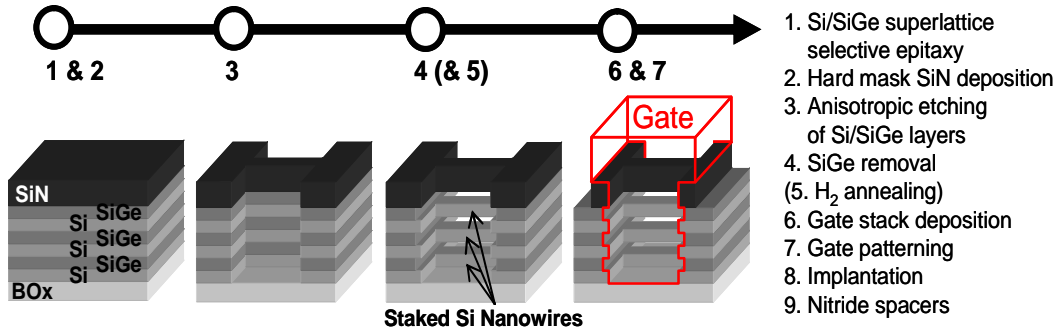


Figure 2.3 Fabricated multi channel FET (MCFET) along (a) channel length and (b) width direction. (c) is the enlarged image of the gate stack.

## 2.3 PROCESS STEP OVERVIEW FOR VERTICALLY-STACKED NANOWIRE MOSFET

Figure 2.4 illustrates briefly the process flow for making vertically stacked silicon nanowire MOSFET [2.5, 2.6]. First, a (30-nm Si / 30-nm Si<sub>0.8</sub>Ge<sub>0.2</sub>)x3 superlattice was epitaxially grown on (100) SOI substrate (step1). 5nm of HTO and 40nm of Si<sub>3</sub>N<sub>4</sub> are deposited as a hard mask on the top of the stack (step 2). Hybrid DUV/ebeam-lithography and resist trimming were combined to define narrow lines. A damascene process was used: cavities were patterned thanks to anisotropic dry plasma etching of the superlattice (step 3). SiGe layers between Si ones were then etched isotropically (step 4). Optionally, an hydrogen annealing process (at 750 °C and 20 Torr for 2 min) was applied to obtained circular cross-sectional shape of nanowires (step 5). The obtained cavities were then filled with the gate stack (HfO<sub>2</sub>/TiN/N<sup>+</sup> poly-Si) (step 6). The gate length is thus defined by the cavity length. Chemical Mechanical Polishing (CMP) of poly-silicon and the thick HTO hard mask deposition for S/D implantation

were carried out followed by the gate patterning (step 7). After gate etching, S/D implantation, spacers formation, and the dopant activation anneal were performed. The nickel silicide was formed on the top of Source / Drain area. The fabrication ended with a standard BEOL process.



*Figure 2.4 Vertically-stacked nanowire MOSFET fabrication process overview [2.5].*

Figure 2.5 shows their cross-sectional TEM and SEM images. We successfully fabricated narrow nanowires by using e-beam lithography and isotropic plasma etching of SiGe sacrificial layers. Good uniformity of the nanowires in a 200-mm-wafer has been also achieved as shown in Figure 2.6. The width ( $W_{NW}$ ) of rectangular shape nanowire ranges from 5 nm up to 30 nm and the height ( $H_{NW}$ ) is 15 nm as seen in Figure 2.7 and Figure 2.8. The smallest nanowire with 5-nm- $W_{NW}$  was formed by  $H_2$  annealing. Thanks to the vertically-stacked channel structures, large surface gains ( $W_{eff}/W_{Top}$ ) have been achieved as shown in Table 2.1. Superior on-state currents per surface unit can be achieved in those devices.

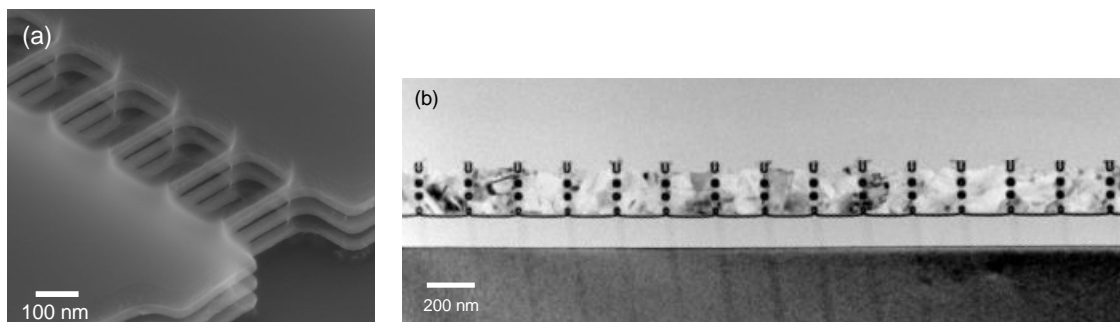


*Figure 2.5 Fabricated vertically-stacked silicon nanowires: (a) a top-view SEM image, (b) a cross-section TEM image.*

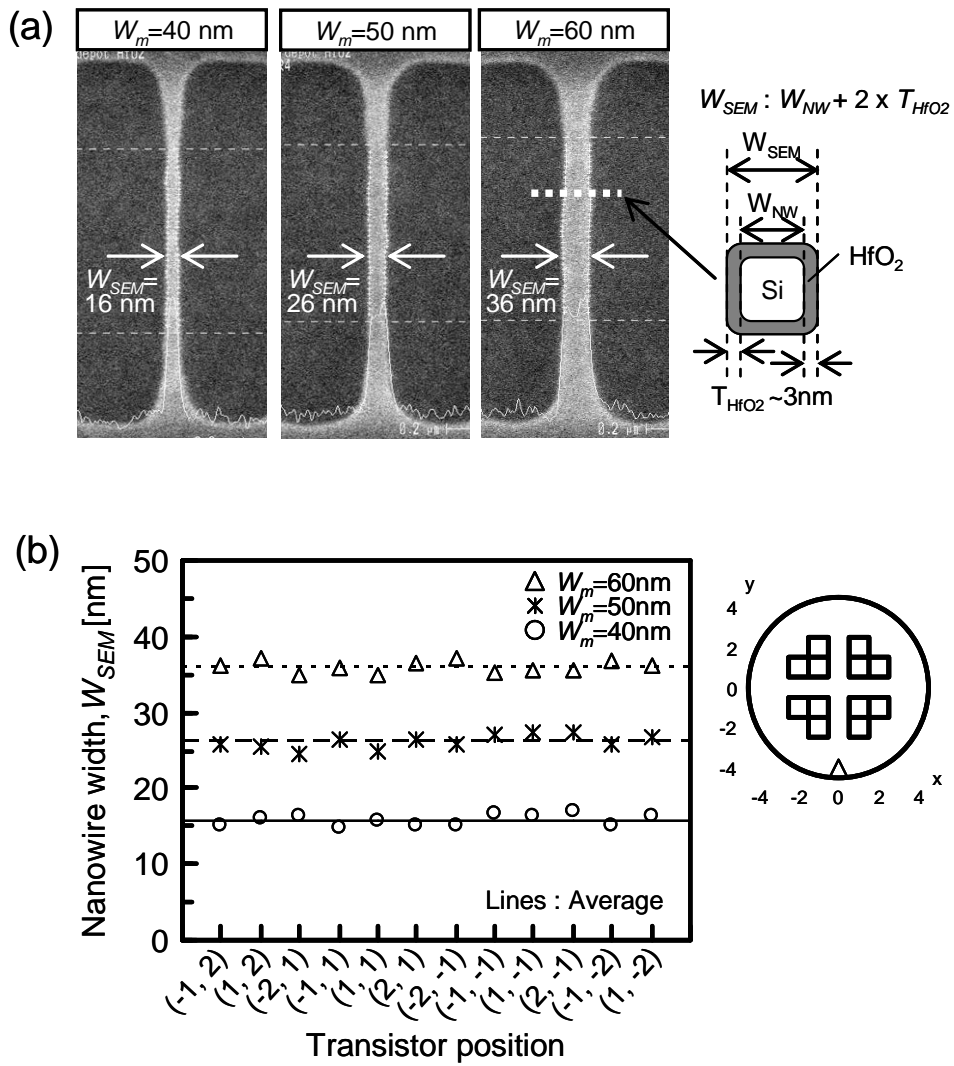


Figure 2.6 (a) Top-view SEM images of silicon nanowires after  $HfO_2$  deposition with width  $W_{SEM} = 16, 26,$  and  $36$  nm. (b) Variation of nanowire width in a 200-nm-wafer. The variations are less than  $\pm 1.5$  nm. The thickness of  $HfO_2$  on side walls ( $3\text{nm} \times 2$ ) is included in the values of  $W_{SEM}$ .  $W_m$  is the mask width.



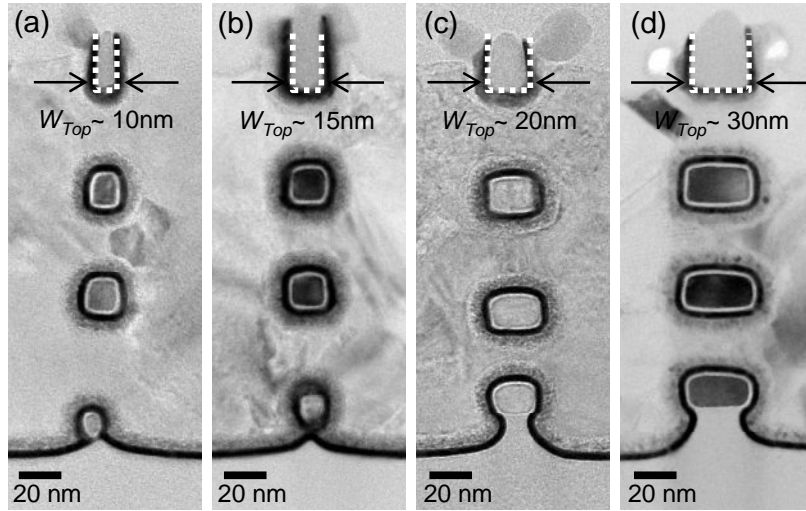


Figure 2.7 Cross-sectional TEM images of vertically-stacked silicon nanowire MOSFET with top-view width  $W_{Top} = 10, 15, 20$  and  $30$  nm.

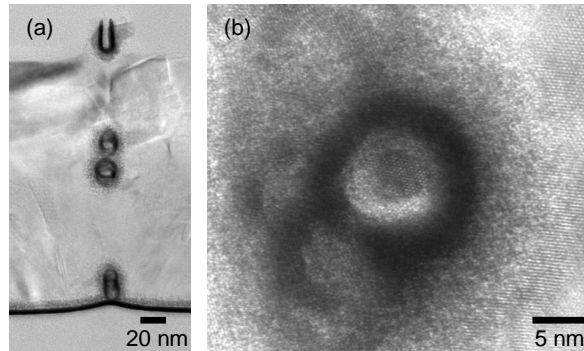
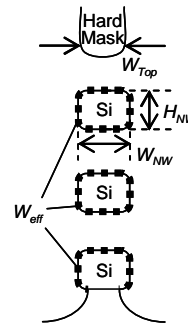


Figure 2.8 (a) Cross-sectional TEM image of vertically-stacked silicon nanowire MOSFET with top-view width  $W_{Top} = 5$  nm. (b) Enlarged image of 5-nm-diameter nanowire.

Table 2.1 Nanowire width with various definitions and surface gain factor  $W_{eff}/W_{Top}$ .

$W_m$ [nm]	40	45	50	60
$W_{Top}$ [nm]	10	15	20	30
Max. $W_{NW}/H_{NW}$ [nm]	11/14	15/14	21/15	32/15
$W_{eff}$ [nm]	102	130	171	227
$W_{eff}/W_{Top}$	10.2	8.7	8.5	7.6



The NWs are [110]-oriented and horizontally arrayed with 50 or 10 parallel wires. The physical wire lengths ( $L_{NW}$ ) are in the 42 – 607 nm range as shown in Figure 2.9. Effective gate length ( $L_{eff}$ ) and source/drain resistance ( $R_{SD}$ ) were extracted thanks to the Y-function-based technique as shown in Chapter 3. Differences between  $L_{NW}$  and  $L_{eff}$  were less than 10 nm. This means that the source/drain implantation and activation annealing are well-controlled. The resulting  $R_{SD}$  are 159  $\Omega \cdot \mu m$  for NMOS and 161  $\Omega \cdot \mu m$  for PMOS.

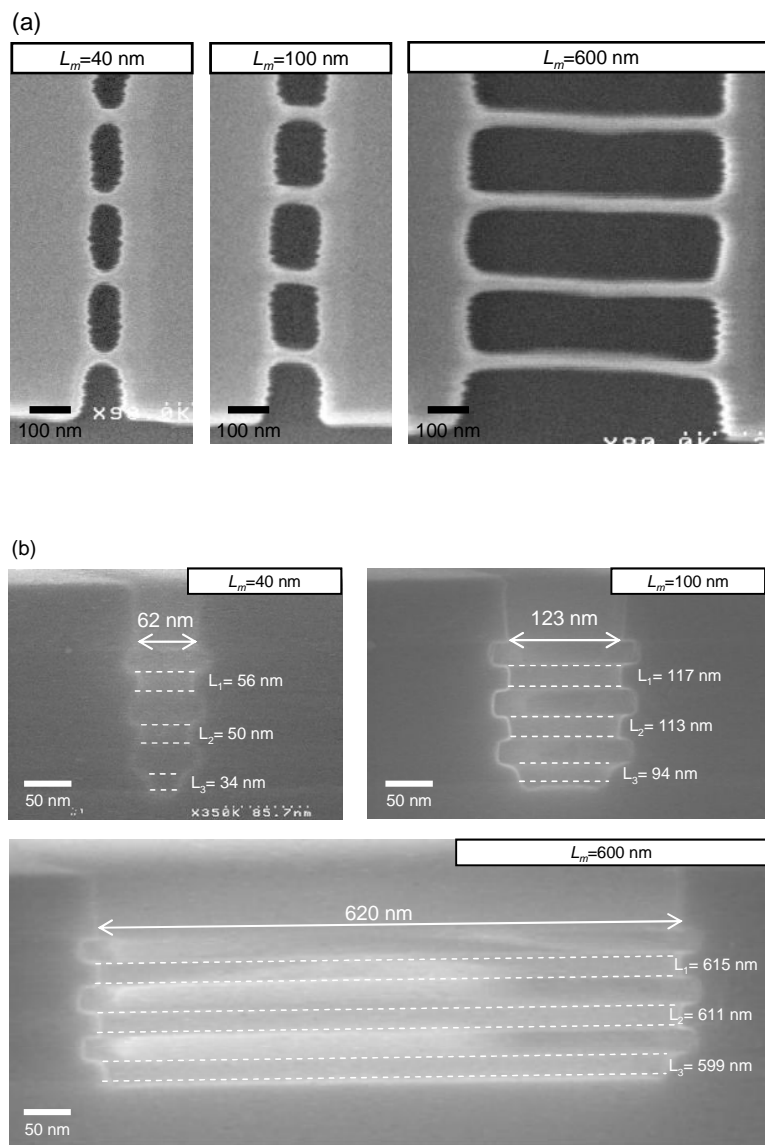


Figure 2.9 Top-view (a) and cross-section (b) of SEM images of vertically-stacked silicon nanowire MOSFET with mask length  $L_m = 40, 100,$  and  $600$  nm.

## 2.4 KEY STEPS

In the processes of two type of vertically-stacked channel MOSFETs, the following technologies were commonly used.

### 2.4.1 SiGe Epitaxy and Etching

#### ■ Si<sub>0.8</sub>Ge<sub>0.2</sub>/Si superlattice epitaxial growth

Si<sub>0.8</sub>Ge<sub>0.2</sub>/Si epitaxial growth is processed in the Epi Centura Reduced-Pressure Chemical Vapor Deposition (RP-CVD) industrial cluster tool [2.7]. The Si layers are grown at 700°C and the SiGe ones at 650°C. Such a low growth temperature enables to grow quite thick layers without any elastic relaxation of the strain through the formation of surface undulations [2.1]. Pure dichlorosilane (SiH<sub>2</sub>Cl<sub>2</sub>) is used as the source of Si and germane (GeH<sub>4</sub>) diluted at 2% in H<sub>2</sub> as the source of Ge. The number of vertically aligned channels is determined by that of the grown SiGe/Si layers and is practically limited by the possible superlattice relaxation due to the compressively strained SiGe layers.

#### ■ Anisotropic plasma etching of Si<sub>0.8</sub>Ge<sub>0.2</sub>/Si superlattice

Hybrid lithography with Deep UV (248nm wavelength) (equipment: ASM 300) and ebeam (equipment: LEICA VB6HR) was used to define the initial photo-resist patterns. The whole stack with Si<sub>3</sub>N<sub>4</sub>/SiO<sub>2</sub> Hard Mask (HM) is etched in an applied material reactor (Applied Material Centura tool). The etching process is divided into five steps as seen in Table 2.1.

*Table 2.2 Process description of anisotropic etching of SiGe/Si superlattice*

Step description	Plasma chemistry	Step type
Resist trimming (optional)	Cl <sub>2</sub> /O <sub>2</sub>	Adjusted Time
Resist cure (optional)	HBr	Time= 60s
Oxide hard mask etch	CF <sub>4</sub> /CH <sub>2</sub> F <sub>2</sub> /He	Time=15s
Hard Mask etch	CF <sub>4</sub> /CH <sub>2</sub> F <sub>2</sub> /O <sub>2</sub> /He	Endpoint
Si/SiGe multilayer main etch	Cl <sub>2</sub> /HBr/O <sub>2</sub>	Endpoint + over etch

### 2.4.2 High- $\kappa$ /Metal Gate Stacks

High- $\kappa$  dielectrics and metal gate are strongly required to achieve small EOT with low gate leakage current density. TiN/HfO<sub>2</sub> has been chosen as a gate stack for both n- and p-MOS. 3 nm of HfO<sub>2</sub> and 10 nm of TiN are deposited in the cavities by uniform deposition methods of Atomic Layer Deposition (ALD) and Chemical Vapor Deposition (CVD), respectively. The thick N<sup>+</sup> polysilicon layers (CVD) are used to fill in the cavities and connect the vertically-stacked gates. Figure 2.10 shows cross-sectional TEM image of silicon nanowire with 3nm-thick-HfO<sub>2</sub> and 10nm-thick-TiN gate stack. A SiO<sub>2</sub>-like interfacial layer was observed. This layer is grown by the thermal process after the gate deposition. The resulting equivalent oxide thickness (EOT) is ~1.7 nm.

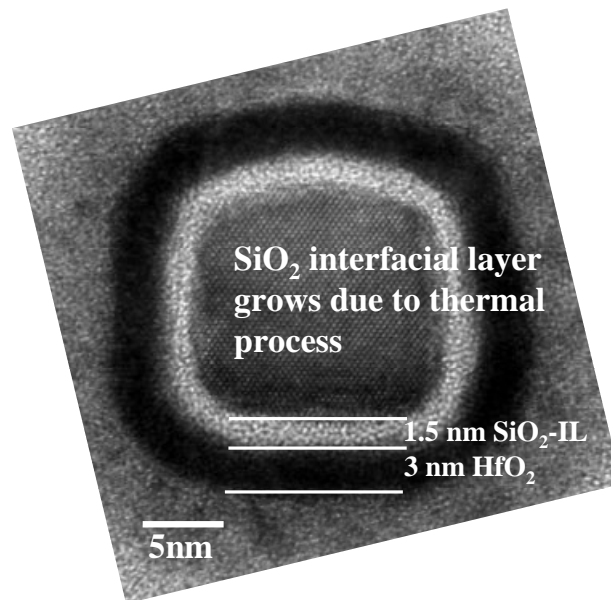


*Figure 2.10 Cross-sectional TEM image of vertically-stacked silicon nanowire with high- $\kappa$ /metal gate.*

## 2.5 CONCLUSIONS

In this chapter, the fabrication process of the vertically-stacked channel MOSFETs were described. The use of sacrificial SiGe layers enables silicon channel to be piled up. The gate stacks were uniformly surrounded owing to ALD and CVD process.

## 2.6 REFERENCES

- [2.1] A.J. Pidduck, D.J. Robbins, A.G. Cullis, W.Y. Leong, A.M. Pitt, “Evolution of surface morphology and strain during SiGe epitaxy”, *Thin Solid Films*, Vol. 222, Issue 1-2, pp. 78-84, 1992.
- [2.2] E. Bernard, T. Ernst, B. Guillaumot, N. Vulliet, T.C. Lim, O. Rozeau, F. Danneville, T. Skotnicki, S. Deleonibus, O. Faynot, “Novel internal spacers 50nm gate length Multi-Channel MOSFET (MCFET) with TiN/HfO<sub>2</sub> gate stack”, *IEEE Electron Device Letters*, 2009.
- [2.3] E. Bernard, T. Ernst, B. Guillaumot, N. Vulliet, P. Coronel, T. Skotnicki, S. Deleonibus, O. Faynot, “Multi-Channel Field Effect Transistors (MCFET) - Part I: Electrical performances and current gain analysis”, to be published in *IEEE Transactions on Electron Devices*, 2009.
- [2.4] E. Bernard, T. Ernst, B. Guillaumot, N. Vulliet, P. Coronel, T. Skotnicki, S. Deleonibus, O. Faynot, “Multi-Channel MOSFET (MCFET) structures - Part II : Analysis of the gate stack and the series resistances influence on the performances”, *IEEE Transactions on Electronic Devices*, 2009.
- [2.5] C. Dupré, A. Hubert, S. Bécu, M. Jublot, V. Maffini-Alvaro, C. Vizioz, F. Aussenac, C. Arvet, S. Barnola, J.-M. Hartmann, G. Garnier, F. Allain, J.-P. Colonna, M. Rivoire, L. Baud, S. Pauliac, V. Loup, T. Chevolleau, P. Rivallin, B. Guillaumot, G. Ghibaudo, O. Faynot, T. Ernst, and S. Deleonibus, “15nm-diameter 3D Stacked Nanowires with Independent Gate Operation:  $\Phi$ FET,” in *IEDM Tech. Dig.*, 2008, pp. 749–752.
- [2.6] K. Tachi, M. Casse, D. Jang, C. Dupré, A. Hubert, N. Vulliet, V. Maffini-Alvaro, C. Vizioz, C. Carabasse, V. Delaye, J. M. Hartmann, G. Ghibaudo, H. Iwai, S. Cristoloveanu, O. Faynot, and T. Ernst, “Relationship between mobility and high- $k$  interface properties in advanced Si and SiGe nanowires,” in *IEDM Tech. Dig.*, pp.313–316, 2009, Baltimore, US.
- [2.7] J.M. Hartmann, M. Py, P.H. Morel, T. Ernst, N. Vulliet, B. Previtali and J.P. Barnes, “Cyclic Deposition / Etch processes for the formation of Si raised sources and

drains in advanced MOSFETs,” *ECS Trans.*, Vol. 33, No. 6, pp. 391–407, 2010.

# **CHAPTER 3**

## *ELECTRICAL CHARACTERIZATION METHODS*

# CHAPTER 3 CONTENTS

## **3 Electrical Characterization Methods**

- 3.1 Introduction
- 3.2  $Y$ -function Method
- 3.3 Split  $C$ - $V$  Method
- 3.4 Conclusions
- 3.5 References



### 3.1 INTRODUCTION

In order to analyze the performances of the MCFET architecture, it was necessary to extract its intrinsic parameters such as the threshold voltage, the carrier mobility or the series resistances. In the literature, a lot of extraction methods have been proposed: “Shift&Ratio”, “Mc Larty”, “Hamer”, “Y function” or “split-CV” (only for mobility extraction). They are all based on the exploitation of the  $I_D$ - $V_G$  characteristics. For our extractions, we preferentially used the Y function [3.1] and split-CV methods [3.2, 3.3]. Those latter are detailed in the following.

### 3.2 Y-FUNCTION METHOD

This method is based on the combined exploitation of the  $I_D$ - $V_G$  and  $g_m$ - $V_G$  characteristics. The MOSFET parameter extraction is performed within the strong inversion regime of the MOSFET linear region and, therefore, relies on the well known drain current expression given by equation (3.1):

$$I_D = \frac{W}{L} \mu_0 \cdot C_{ox} \cdot \frac{(V_G - V_T) \cdot V_D}{1 + \theta_1 \cdot (V_G - V_T)} \quad (3.1)$$

where  $W$  and  $L$  are the channel width and channel length,  $V_T$  is the threshold voltage,  $C_{ox}$  is the gate oxide capacitance,  $\mu_0$  is the low field mobility and  $\theta_1$  is the first mobility reduction coefficient which takes into account the influence of the series resistances (3.2).

$$\theta_1 = \theta_{1,0} + \frac{W}{L} \mu_0 \cdot C_{ox} R_{SD} \quad (3.2)$$

where  $\theta_{1,0}$  is the intrinsic mobility reduction factor.

The basic idea consists in constructing a function which is independent of the series resistances  $R_{SD}$ , i.e. which does not contain  $\theta_1$  (because  $R_{SD}$  strongly degrade the drain current especially in short channel devices). This can be achieved by dividing the current expression by the square root of the transconductance (3.3):

$$Y = \frac{I_D}{\sqrt{g_m}} = \sqrt{\beta \cdot V_D} \cdot (V_G - V_T) \quad (3.3)$$

where  $g_m$  and  $\beta$  are respectively the transconductance and gain factor of the transistor. Their expressions are given by equations (3.4) and (3.5) respectively:

$$g_m = \left. \frac{\partial I_D}{\partial V_G} \right|_{V_D} = \beta \cdot \frac{1}{[1 + \theta_1 \cdot (V_G - V_T)]^2} \quad (3.4)$$

$$\beta = \frac{W}{L} \cdot \mu_0 \cdot C_{ox} = \frac{S_Y^2}{V_D} \quad (3.5)$$

where  $S_Y$  is the Y function slope.

In the strong inversion regime, the Y function varies linearly with the gate voltage (Figure 3.1). The threshold voltage can then be obtained by the extrapolation of the linear part of the curve (intercept with the X-axis).

On the other hand, the low field mobility  $\mu_0$  can be extracted from the Y function slope as expressed in equation (3.6):

$$\mu_0 = \frac{S_Y^2}{C_{ox} \cdot V_D} \cdot \frac{L}{W} \quad (3.6)$$

For that, we only need to know the oxide capacitance  $C_{ox}$ , which is extracted by capacitance measurements ( $C_{GC}(V_G)$ ), and the effective gate length and width,  $L_{eff}$  and  $W$ . According to equation (3.7), the effective gate length can be obtained by plotting  $1/\beta$  as a function of the gate length and by taking the value for which  $1/\beta$  is null (Figure 3.2).

$$\frac{1}{\beta} = \frac{L - \Delta L}{W \cdot \mu_0 \cdot C_{ox}} \quad (3.7)$$

But this method supposes that the difference  $\Delta L$  between the effective gate length  $L_{eff}$  and the mask gate length  $L_m$  is constant, which is not always true. In order to circumvent this problem, another method based on the Shift&Ratio procedure has been set up by *Cretu et al* [1.4]. This latter is based on the variation of the Y function

between a short channel transistor and a long channel one (this method is not explained here). It should be noted that the Y function method allows a separate determination of the threshold voltage and the mobility.

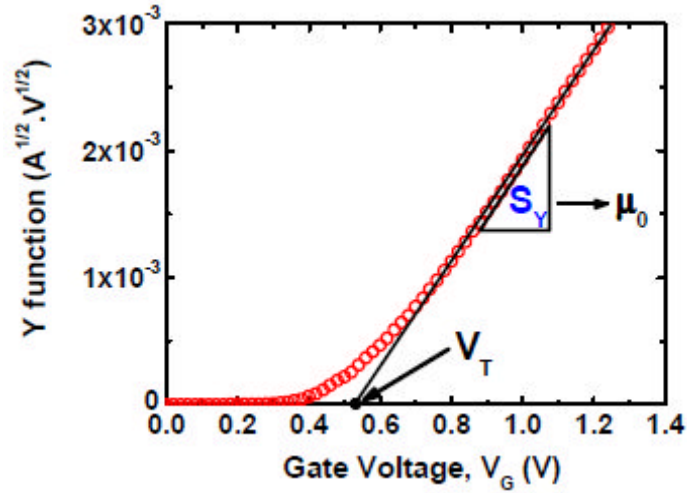


Figure 3.1 Y- function as a function of the gate voltage.

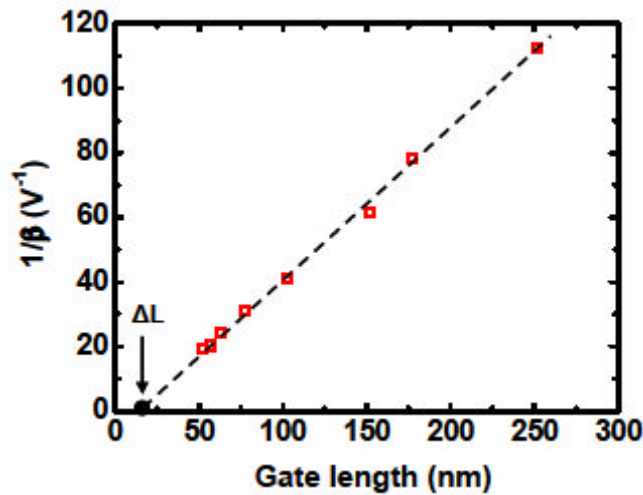


Figure 3.2 Extraction of the effective gate length.

After the extraction of the threshold voltage, we can calculate the mobility reduction factor  $\theta_{\text{eff}}$  defined by equation (3.8):

$$\theta_{\text{eff}} = \frac{S_Y^2}{I_D} - \frac{1}{V_G - V_T} \quad (3.8)$$

where  $\theta_2$  is the second mobility reduction coefficient taking into account the surface roughness.

Indeed, at high  $V_G$  ( $V_G \gg V_T$ ), the mobility is described by two attenuation factors (3.9):

$$\mu_{\text{eff}} = \frac{\mu_0}{1 + \theta_1 \cdot (V_G - V_T) + \theta_2 \cdot (V_G - V_T)^2} \quad (3.9)$$

For  $V_G \gg V_T$ ,  $\theta_{\text{eff}}$  is proportional to the gate voltage as shown by equation (3.10):

$$\theta_{\text{eff}}(V_G \gg V_T) = \theta_1 + \theta_2 \cdot (V_G - V_T) \quad (3.10)$$

So, by plotting  $\theta_{\text{eff}}$  as a function of the gate voltage, we can extract  $\theta_1$  (intercept with the Y-axis) and  $\theta_2$  (slope). Note that a low value for  $\theta_2$  indicates a good Si/SiO<sub>2</sub> interface (low surface roughness). From  $\theta_1$ , we can finally extract the series resistances. To do this,  $\theta_1$  is plotted as a function of  $\beta$ . The  $R_{SD}$  are then extracted from the slope of this curve (Figure 3.3).

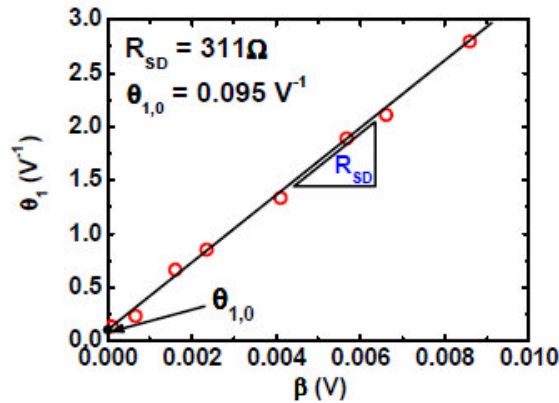


Figure 3.3 Extraction of the series resistances for 40nm to 600nm gate lengths MCFET devices ( $W = 500\text{nm}$ ).

The accuracy of the extraction can be improved by introducing the second mobility reduction coefficient  $\theta_2$  in the Y function (3.11) and by recalculating all the parameters.

$$Y_{\text{new}} = Y \cdot \sqrt{1 - \theta_2 \cdot (V_G - V_T)^2} \quad (3.11)$$

This correction is only necessary if  $\theta_2 \approx 1/(V_G - V_T)^2$ .

At the end of the extraction, we can compare the theoretical linear drain current calculated by using the extracted parameters and the experimental one. For that, we use the expression of the linear current given by equation (3.12).

$$I_D = \frac{W}{L_{\text{eff}}} \mu_0 \cdot C_{\text{ox}} \cdot \frac{(V_G - V_T) \cdot V_D}{1 + \theta_1 \cdot (V_G - V_T) + \theta_2 \cdot (V_G - V_T)^2} \quad (3.12)$$

Figure 3.4 shows the comparison the calculated curves with the measured data. As we can see, an excellent fit is obtained between the model and the experiments. The model is then well adapted even for short channel MOSFET devices ( $L_G < 100\text{nm}$ ).

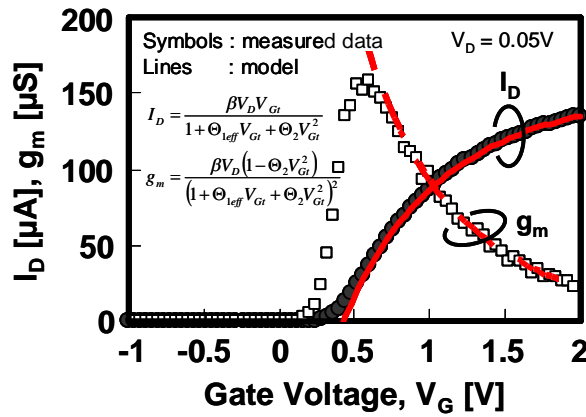


Figure 3.4 Measured and modeled  $I_{Dlin}-V_G$  and  $g_{mlin}-V_G$  characteristics of TiN/HfO<sub>2</sub> n-MCFETs. Gate length and width are 70 nm and 350 nm, respectively.

### 3.3 SPLIT C-V METHOD

This method is based on the combination of two capacitance measurements and one current-voltage measurement in order to obtain the effective mobility  $\mu_{\text{eff}}$  as a function of the inversion charge  $Q_{\text{inv}}$  or the effective electric field  $E_{\text{eff}}$ .

In a first time, the gate-to-channel capacitance  $C_{GC}$  is measured for different gate voltages. The inversion charge  $Q_{\text{inv}}$  at a given gate voltage  $V_G$  is then obtained by integrating this capacitance until the wished gate voltage (3.13).

$$Q_{\text{inv}}(V_G) = \frac{1}{L_{\text{eff}} \cdot W_{\text{eff}}} \cdot \int_{-\infty}^{V_G} C_{GC}(V_G) \cdot dV_G \quad (3.13)$$

In a second time, the gate-to-substrate capacitance  $C_{GB}$  is measured and integrated so as to obtain the depletion charge (3.14).

$$Q_{dep}(V_G) = \frac{1}{L_{eff} \cdot W_{eff}} \cdot \int_{V_{th}}^{V_G} C_{GB}(V_G) \cdot dV_G \quad (3.14)$$

The effective field is then calculated according to equation (2.15).

$$E_{eff} = \frac{\eta \cdot Q_{inv} + Q_{dep}}{\epsilon_{Si}} \quad (3.15)$$

where  $\eta$  is an empiric parameter equal to 1/2 for electrons and to 1/3 for holes.

Note that on SOI substrate  $C_{GB}$  measurement cannot be performed due to the presence of the BOX. But for ultra-thin films transistors on SOI with undoped channels and thick BOX (which is the case of our transistors), the depletion charge is negligible compared to the inversion charge and the effective field is solely determined from the inversion charge.

Finally, the effective mobility is obtained by dividing the drain current by the inversion charge (3.16):

$$\mu_{eff} = \frac{L_{eff}}{W_{eff}} \frac{I_D}{Q_{inv} \cdot V_D} = \frac{I_D \cdot L_{eff}^2}{Q_{invS} \cdot V_D} \quad (3.16)$$

where  $Q_{invS} = Q_{inv} \cdot W_{eff} \cdot L_{eff}$  is the measured inversion charge. As a consequence, the effective mobility is only dependant of the effective gate length.

The split C-V method is applicable to short channel devices [3.3], only if: the drain current is corrected by the series resistances, the capacitances are corrected from the parasitic capacitances and the effective gate length is correctly extracted.

The correction of the drain current by the  $R_{SD}$  is given by equation (3.17):

$$I_{D0} = \frac{I_D}{1 - \frac{R_s \cdot I_D}{V_D}} \quad (3.17)$$

where  $I_D$  is the measured current and  $I_{D0}$  the corrected current.

On the other hand,  $L_{eff}$  is extracted thanks to the measurement of  $C_{GC}$  for a short channel device with a gate length  $L_{eff\_short}$  and for a long channel device with a gate

length  $L_{\text{eff\_long}}$  (considered equal to the mask gate length). The effective gate length of the short channel device is then calculated according to equation (3.18).

$$L_{\text{eff\_short}} = \frac{C_{\text{inv0}}^{\text{short}}}{C_{\text{inv0}}^{\text{long}}} \cdot L_{\text{eff\_long}} \quad (3.18)$$

where  $C_{\text{inv0}} = C_{\text{GC}} - C_{\text{p}}$  is the maximum of the gate-to-channel capacitance corrected by the parasitic capacitances  $C_{\text{p}}$  (overlap and fringing capacitances). Finally, the inversion charge is calculated by using  $C_{\text{GC0}}$  (instead of  $C_{\text{CG}}$ ) which is the gate-to-channel capacitance corrected from the parasitic capacitances.

In order to accurately evaluate the transport properties, the effective mobility was extracted by split C-V technique with parasitic capacitance and  $R_{\text{SD}}$  corrections. Figure 3.5 shows the validity of the extraction. A good agreement when compared to other techniques was achieved.

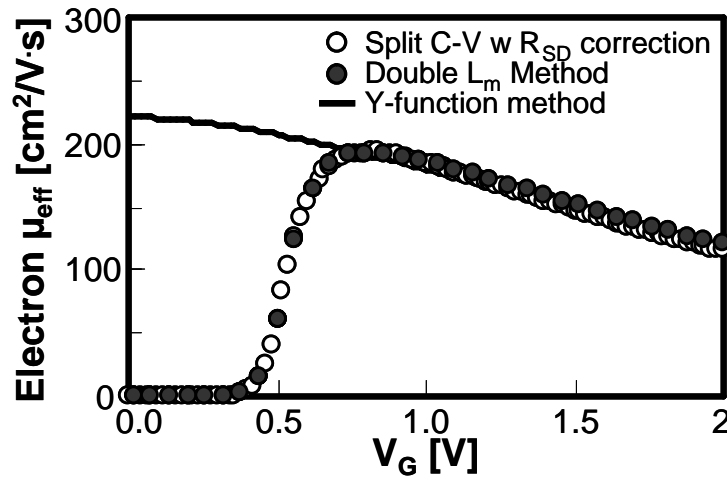


*Figure 3.5 Comparison of effective mobility extracted by split C-V, double  $L_m$  method, and from parameters extracted by Y-function method. The measured device is the stacked SNWTs with  $W_{\text{NW}}=15$  nm and  $L_{\text{eff}}=242$  nm. The device with  $L_{\text{eff}}=592$  nm was also used for double  $L_m$  method.*

### **3.4 CONCLUSIONS**

In this chapter, the two electrical characterization methods were described. The calculated  $I-V$  curve by Y-function method was well fitted to the measured data. This enables to precisely extract device parameters. Finally, good agreement of effective mobility when compared between Y-function method and split C-V technique was achieved.

### **3.5 REFERENCES**

- [3.1] G. Ghibaudo, "New Method for the Extraction of MOSFET Parameters", *Electronics Letters*, Vol. 24, Issue 9, pp. 543-545, 1988.
- [3.2] J. Koomen, "Investigation of the MOST channel conductance in weak inversion", *Solid-State Electronics*, Vol. 16, pp.801-810, 1973.
- [3.3] K. Romanjek, F. Andrieu, T. Ernst, G. Ghibaudo, "Improved Split C-V Method for Effective Mobility Extraction in sub-0.1- $\mu\text{m}$  Si MOSFETs", *IEEE Electron Device Letters*, Vol. 25, Issue 8, pp. 583-585, 2004.



# **CHAPTER 4**

## ***SOURCE/DRAIN DOPING TECHNIQUES FOR VERTICALLY-STACKED CHANNEL STRUCTURE***

# CHAPTER 4 CONTENTS

## 4 Source/Drain Doping Techniques for Vertically-Stacked Channel Structure

4.1 Introduction

4.2 Experimental Conditions

4.3 Electrical Characteristics

4.3.1  $I$ - $V$  Characteristics

4.3.2 Source/Drain Series Resistance Evaluation

4.3.3 Carrier Mobility Evaluation

4.3.4 Gate Length Scaling

4.4 Conclusions

4.5 References

## 4.1 INTRODUCTION

The reduction of parasitic access resistances serially connected at source and drain region of MOSFETS are one of the challenging technology to meet the performance required in the roadmap as discussed in Chapter 1. The voltage drops at the resistances reduces the applied voltages at the drain and gate electrodes in the transistors, resulting in the decrease in the overdrive voltage to lower the on-current. These resistances also cause degradation in the time constant, commonly referred as RC delay, to lower the switching speed. Therefore, as the channel resistance reduces with the scaling in the gate length, the parasitic series resistance should be further reduced not to increase its proportion in the total resistance at on-state.

MOSFETs with 3 dimensional channels (e.g. Fin FETs) severely suffer from the parasitic access resistance with scaling, as the cross-sectional area at the entrance from the source to channel becomes. Therefore, novel processes dedicated for 3 dimensional FETs should be implemented; to modify the shape of the source and drain region to reduce the current density or to further reduce the resistivity of the wiring. One example of the former process is selective epitaxy growth process to elevate the source and drain region to reduce the current density. Since the growth is selectively done only on Si surfaces, the source and drain regions can be modified without any short circuit to other electrodes. One of the concerns is the excess growth of the source and drain regions results in the increase in the gate to drain capacitances, to lower the switching speed. The later process includes recoil ion-implantation, plasma doping and refractory metal silicide technologies; those are aggressively under research.

As with vertically stacked multi channel devices [4.1–4.3], the later approach to reduce the resistivity of the source and drain region should be done as the source and drain regions are already grown to access to the channels. Therefore, a further increase in the doping concentration with higher activation ratio at source and drain regions are mandatory. In terms of the gate to drain capacitances, the use of oxide spacers with lower k-values between gate and drain regions are reported to be effective and a reduction in the intrinsic  $CV/I$  delay by 39 % has been achieved [4.1].

In this chapter, a novel process to decrease the resistivity of the source and drain regions of MCFET is presented using *in situ* doped selective epitaxial growth in combination with conventional ion-implantation (I/I) as a novel process for source and drain formation. The effect of source and drain formation process on the series resistance and carrier mobility will be discussed through electrical characteristics.

## 4.2 EXPERIMENTAL CONDITIONS

Three types of MCFETs with different S/D doping schemes, listed in Table 4.1, were investigated. For control MCFET samples, arsenic ions were implanted to the un-doped selective epitaxial growth (SEG) S/D (with a thickness of 200 nm) with a dose of  $10^{15} \text{ cm}^{-2}$  at 50 keV for *n*-MCFETs. For *p*-MCFETs, boron fluoride ions were implanted with a dose of  $10^{15} \text{ cm}^{-2}$  at 40 keV. For sample A, the source and drain regions were *in situ* doped during the SEG step. The dopant atoms ( $\sim 2 \times 10^{19} \text{ cm}^{-3}$ ) for the *in situ* doped SEG were phosphorus and boron for *n*- and *p*-MCFETs, respectively. For sample B, *in situ* doped SEG was combined with I/I.

*Table 4.1 Doping scheme*

	Un-doped SEG	<i>In situ</i> doped SEG	Ion implantation (I/I)
Control	✓		✓
Process A		✓	
Process B		✓	✓

## 4.3 ELECTRICAL CHARACTERISTICS

### 4.3.1 *I-V* Characteristics

Drive current (at  $|V_G - V_T| = 0.9 \text{ V}$  and  $|V_D| = 1.2 \text{ V}$ ) against standby current (at  $|V_G - V_T| = 0.3 \text{ V}$  and  $|V_D| = 1.2 \text{ V}$ ) for MCFETs with a  $L_G = 70 \text{ nm}$  is shown in Figure 4.1. The currents were normalized by a top-view width. A large enhancement in the drive

current with process A and B respectively, can be obtained with *in situ* doped SEG process compared to the control MCFET. This improvement applies for both *n*- and *p*-MCFETs. The mean drive currents of 2.4 and 1.2 mA/ $\mu$ m are achieved for *n*- and *p*-MCFETs with process B, respectively. These high current densities are due to the *in situ* doped SEG combined with I/I and 3-D configuration of vertically-stacked channels.

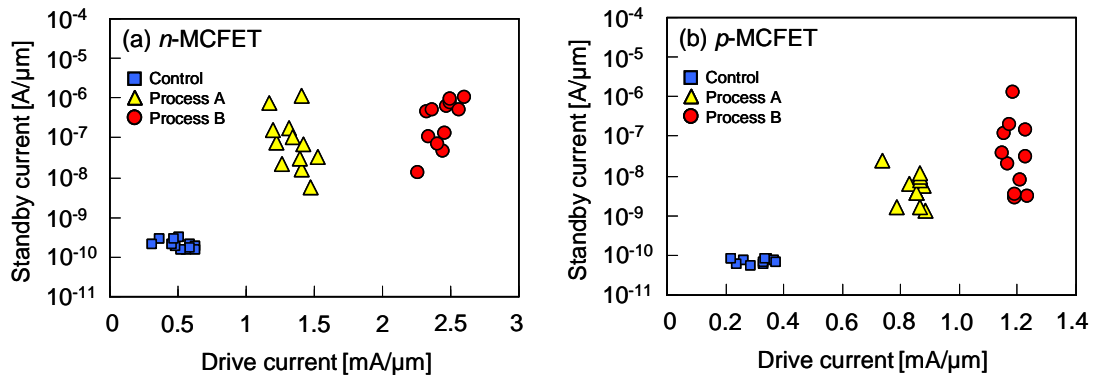


Figure 4.1 On-off relations of (a) *n*- and (b) *p*-MCFETs.

Although the variability in the drive current for *n*- and *p*-MCFET showed little dependence within the same process conditions, the standby currents tend to scatter and the mean value slightly increases with process A and B. The reason of the variability increase in the standby current might be originated from the residual defect in the *in situ* doped SEG. These defects, commonly observed in highly doped silicon, produce generation centers which degrade the on/off junction property.

The threshold voltage dependence on the  $L_G$  is shown in Figure 4.2. Enhanced roll-off properties were observed with sample A and B, where *in situ* doped SEG was adopted. This suggests the influence of the dopant diffusion to lower the abruptness of the junction.

The dependence of the on-current per a unit width ( $\mu$ m) on the  $L_G$ , for both *n*- and *p*-MCFETs, is shown in Figure 4.3. Here, the total width ( $W_{TOT}$ ) of the channels was used for the normalization. The  $I_{ON}(L_G)$  dependence clearly demonstrates the scaling achieved with *in situ* SEG process compared to those with the control MCFETs. Especially one can see the merits of process B, which enables further enhancement in

the  $I_{ON}$  when  $L_G$  is scaled down below 100 nm.

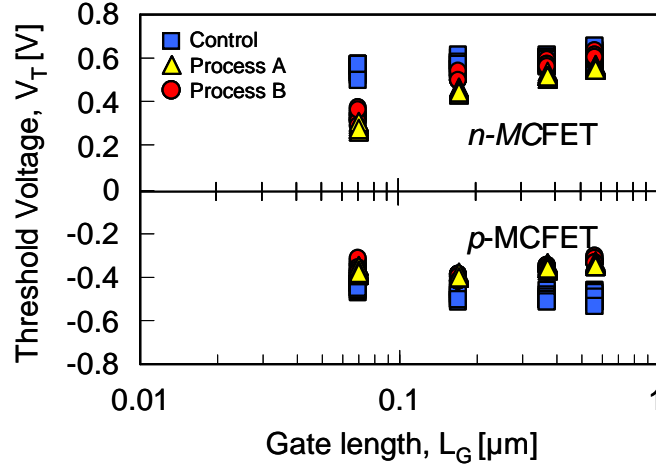


Figure 4.2 Threshold voltage roll-off characteristics of MCFETs with  $L_G$  scaling.

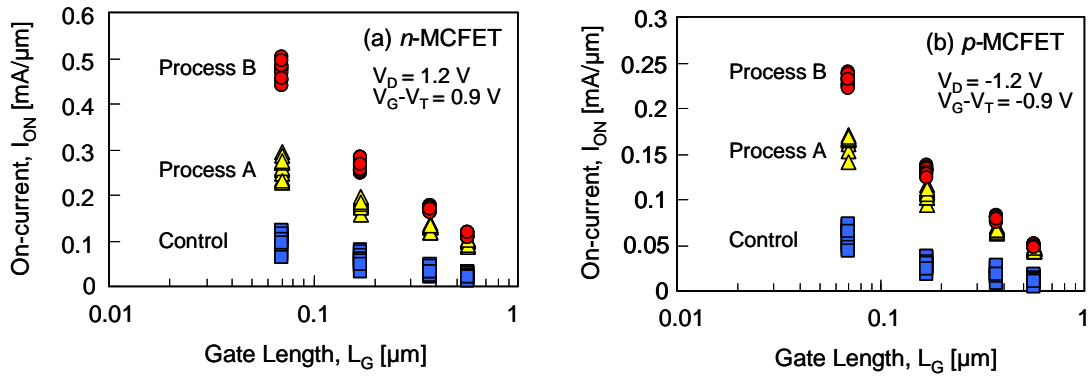


Figure 4.3 On-current dependency on the gate length for (a)  $n$ - and (b)  $p$ - MCFETs.

### 4.3.2 Source/Drain Series Resistance Evaluation

The access resistance values are evaluated through electrical measurements of the transistors by Y-function based methods (see Chapter 3). Figure 4.4 shows typical modeling results of the transconductance of multi channel FETs with different  $L_G$ . One can confirm a fairly nice modeling with the above equations.

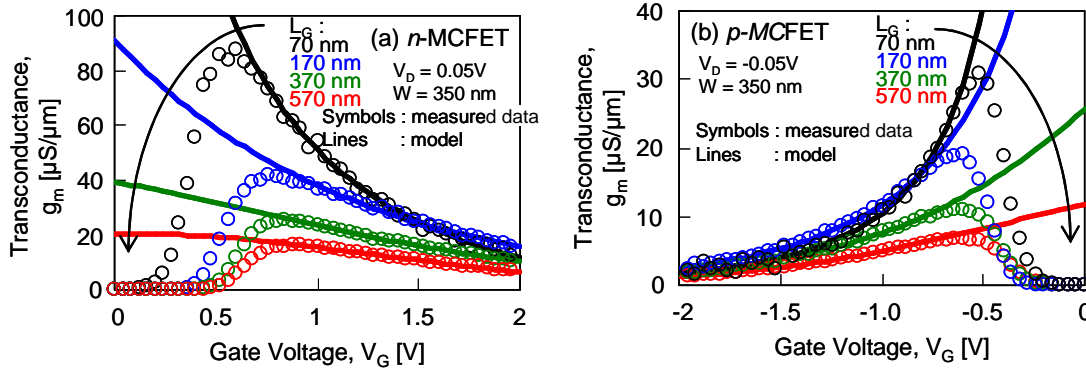


Figure 4.4 Transconductance of the (a) *n*- and (b) *p*-MCFETs. Solid lines represent the fitted model.

$R_{SD}$  can be extracted from the slope in the relation between  $\Theta_{I_{eff}}$  and  $\beta$  as is shown in Figure 4.5. The good linearity in  $\Theta_{I_{eff}}$  vs.  $\beta$  curves, for all the  $L_G$  down to 70 nm, indicates that  $R_{SD}$  is identical among different  $L_G$ . The extracted values of  $R_{SD}$  normalized for a unit channel width ( $\mu\text{m}$ ), for the control sample and MCFETs with process A and B were 4.5, 3.6 and 0.4  $\text{k}\Omega\text{-}\mu\text{m}$  for *n*-MCFET and 5.2, 3.2 and 1.2  $\text{k}\Omega\text{-}\mu\text{m}$  for *p*-MCFET, respectively. Note the remarkable  $R_{SD}$  reduction which has been successfully obtained by combining in situ doped SEG with I/I for both *n*- and *p*-MCFETs (process B). The relatively large  $R_{SD}$  in the control sample may be attributed to un-optimized doping profile in un-doped SEG, so that ion implantation with multiple acceleration energy appears to be necessary.

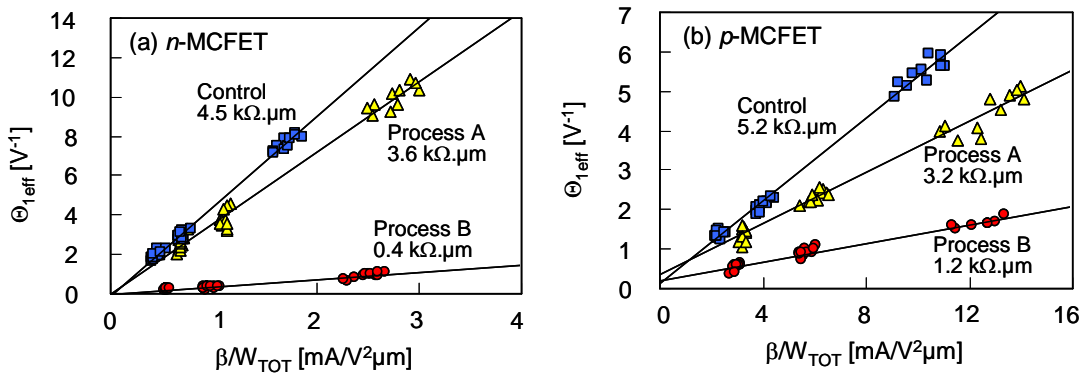


Figure 4.5  $\Theta_{I_{eff}}$  vs.  $\beta$  curves of the fabricated (a) *n*- and (b) *p*-MCFETs.

On the other hand, *in situ* doped SEG process facilitates and improves the processing of vertically aligned MCFETs S/D-channel junctions. The additional I/I into *in situ* doped SEG further reduces the  $R_{SD}$  by 90 % and 60% for n- and p-MCFET, respectively. The origin of the reduction is still unclear, however, for n-MCFET the better positioning and uniformity of the doped S/D and the high solubility of implanted arsenic atoms in silicon compared to that of phosphorus atoms may increase the activation rate, leading to a decrease in  $R_{SD}$ .

### 4.3.3 Carrier Mobility Evaluation

Besides the  $R_{SD}$  values, the effect of junction formation process affects the effective mobility  $\mu_{eff}$  in the channel, in particular when neutral defects are formed during I/I steps. A degraded  $\mu_{eff}$  is commonly observed for small  $L_G$ . We here investigate the  $\mu_{eff}$  of the MCFETs and compared the influence of the junction formation process. The  $\mu_{eff}$  was extracted by a modified split C-V method in order to exclude the parasitic capacitance, which may become dominant in scaled  $L_G$ . Figure 4.6 shows examples of gate-to-channel capacitances  $C_{GC}$  ( $V_G$ ) curves of the MCFETs with process A and B, indicating that the parasitic capacitances were identical among different  $L_G$ , so that the inversion carrier density can be extracted.

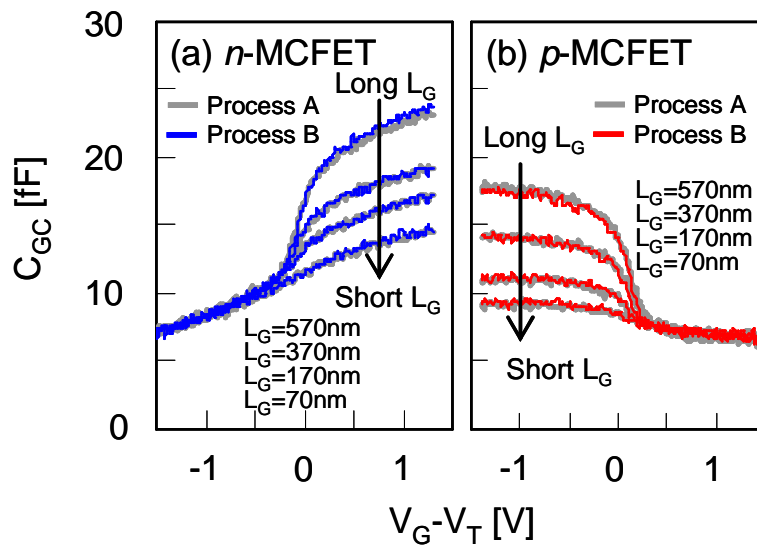


Figure 4.6  $C_{GC}$  characteristics with various  $L_G$  for (a) n- and (b) p-MCFETs.



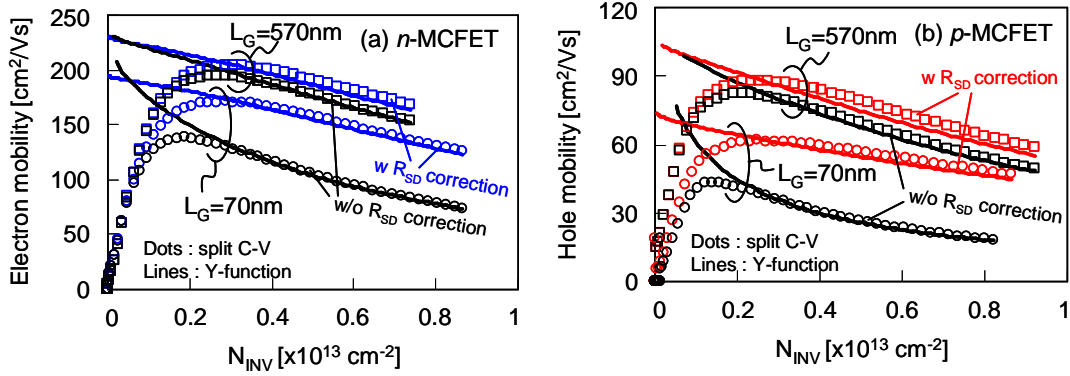


Figure 4.7  $\mu_{eff}$  of the MCFETs with different  $L_G$  of 570 and 70 nm.

Additionally,  $R_{SD}$  correction for  $\mu_{eff}$  extraction is necessary as the output conductance is strongly degraded by the parasitic resistance. Figure 4.7 (a) and (b) show the  $\mu_{eff}$  of  $n$ - and  $p$ -MCFETs of  $L_G=70$  and 570 nm with process B with and without RSD correction, respectively. The contribution of  $R_{SD}$  on the  $\mu_{eff}$  is obviously more prominent when the  $L_G$  is scaled, as the ratio of the  $R_{SD}$  to the total resistance increases. The  $\mu_{eff}$  calculated by Y-function method agrees well with the  $\mu_{eff}$  extracted by split C–V method in the region of high carrier density, confirming the correctness of the extracted  $\mu_{eff}$ . Process A results in slightly higher mobility values, as illustrated in Figure 4.7.

One can observe a degraded  $\mu_{eff}$  with smaller  $L_G$  for both  $n$ - and  $p$ -MCFETs even after  $R_{SD}$  correction. This fact implies the existence of another mechanism degrading the  $\mu_{eff}$  in the direction of channel. Figure 4.8 compares the low-field mobility  $\mu_0$  values in MCFETs with process B and C. A distinct degradation in the  $\mu_0$  with  $L_G$  scaling can be observed for both  $n$ - and  $p$ -MCFETs. Using the model proposed by Bidal *et al.*[4.4], a  $L_G$ -dependent limiting mobility,  $\mu_0(L_G)$ , can be postulated as

$$\frac{1}{\mu_0(L)} = \frac{1}{\mu_{max}} + \frac{\alpha_\mu}{L_G}, \quad (3.7)$$

where  $\mu_{max}$  and  $\alpha_\mu$  are the maximum mobility in long channel MCFETs and the mobility degradation factor, respectively. Using this model with the two fitting parameters,  $\mu_0$  at further scaled  $L_G$  can be predicted as shown in Figure 4.8. Although no  $\mu_0$  difference is expected at  $L_G$  of 10 nm, the mean  $\mu_{max}$  showed smaller values with process B compared to those with process A, suggesting the influence of  $I/I$ .

On the other hand, the  $\alpha_{\mu}$  values were found to be similar in the range of 0.09~0.10 and 0.22~0.24 nm-Vs/cm<sup>2</sup> for *n*- and *p*-MCFETs, respectively. Therefore, the degraded  $\mu_{eff}$  in the low carrier density region can be considered to be originated by Coulomb scattering from the dopant atoms diffusion from S/D regions induced by I/I B-type process. Indeed the  $V_T$  roll-off characteristics on  $L_G$  shown in Figure 4.2 revealed slightly changed characteristics for both *n*- and *p*-MCFETs, supporting the possibility of diffusion of dopants. Moreover, the threading dislocation patterns observed in the TEM images shown in Figure 2.3 suggest an enhanced diffusion of dopant atoms, typically reported as 100 times higher, through the defects which reduces the abruptness of channel and S/D regions [4.5].

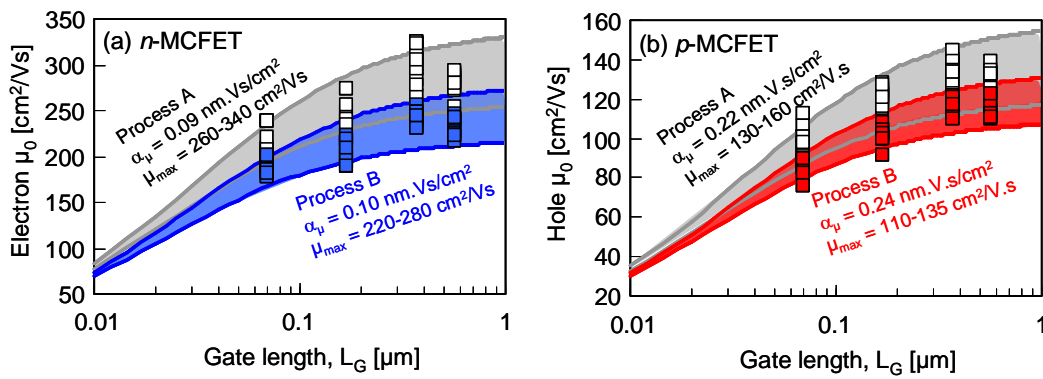


Figure 4.8 Estimated  $\mu_0$  on  $L_G$  scaling.

The values of the  $\alpha_{\mu}$  and  $\mu_{max}$  for MCFETs are summarized with reported values for planar FETs in Figure 4.9. The MCFETs with in situ SEG process show 2 and 3 times higher values in  $\alpha_{\mu}$  than the ballistic limit ( $\alpha_{\mu,bal}$ ), for *n*- and *p*-MCFETs, respectively. This deviation indicates the presence of Coulomb scattering in the channel which can also be inferred from the lower  $\mu_{max}$  value compared to other devices. The message is that, although in situ doped SEG process is useful for  $R_{SD}$  reduction, further process optimization in the dopant activation step is needed in order to suppress the diffusion of dopant atoms in to the channel.

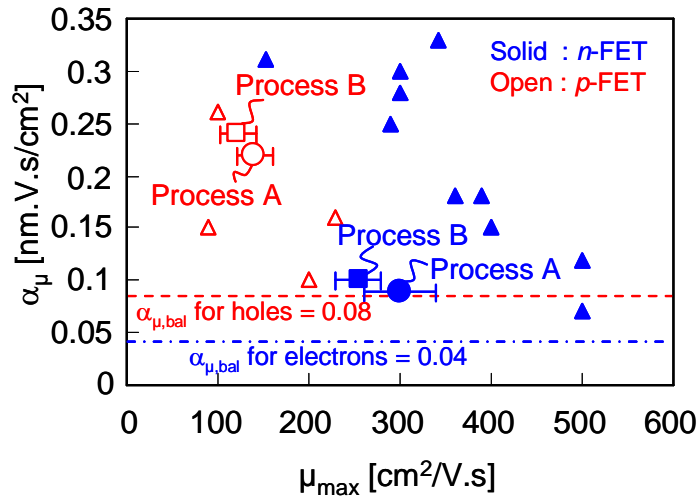


Figure 4.9 Summary of the extracted  $\alpha_{\mu}$  and  $\mu_{max}$ .

### 4.3.4 Gate Length Scaling

Using the extracted  $\alpha_{\mu}$  and  $\mu_{max}$ , one can estimate the  $\mu_0$  of the MCFETs with further scaled  $L_G$ . From Figure 4.9, the  $\mu_0$  with  $L_G$  scaling can be estimated. The  $\mu_0$  trend showed further reduction at scaled  $L_G$ , even considering the variability. The difference of the  $\mu_0$  becomes smaller between the process A and B. This estimation indicates that the electrical influence of the diffused dopants from the source and drain region can be neglected as large portion of ballistic limited mobility dominates at these  $L_G$  regions.

Here we examine the global MCFETs down-scaling, including short-channel effects. The  $I_{OFF}$  behavior, when normalized by a common threshold voltage  $V_T$ , reflects the subthreshold properties such as DIBL and SS (not the  $V_T$  roll-off, however). Figure 4.10 shows the  $I_{ON}$ - $I_{OFF}$  characteristics of n- and p-MCFET with several  $L_G$  and  $W$ . The currents were normalized by the total channel surface  $W_{total}$  ( $W_{total} = W \times 5ch. + T_{Si} \times 6side-ch.$ ). When reducing  $L_G$  down to 70 nm,  $I_{OFF}$  increases progressively due to the enhanced DIBL, while the SS value remains constant at  $\sim 70$  mV/decade for nFET and  $\sim 75$  mV/decade for pFET. MCFETs with  $L_G$  smaller than 70 nm have degraded subthreshold properties without the expected  $I_{ON}$  enhancement. This kind of degradation can be suppressed by adding the lateral gates electrostatic control through  $W$  down-scaling [4.6]. Drive current gains of 14 % for nFET and 20 % for pFET were

observed when  $W$  was reduced from 350 nm down to 100 nm. We measured in the meantime an improved mobility  $\mu_0$  of 11 % and 18 % for nFET and pFET, respectively. This suggests that  $W$  down-scaling may reduce the  $L_G$  dependent mobility degradation. Additional investigation is needed in order to obtain a physical explanation of this phenomenon which is compatible with volume inversion.

Lastly, we present the scaled MCFETs characteristics with the process C. Figure 4.11 shows  $I_D-V_G$  and  $I_D-V_D$  characteristics associated to 50-nm- $L_G$  80-nm- $W$  nMCFET and 40-nm- $L_G$  and 70-nm- $W$  pMCFET. We obtained extremely high  $I_{ON}$ -currents of 4.1 mA/ $\mu\text{m}$  for nFET and a record 2.7 mA/ $\mu\text{m}$  for pFET at  $V_{DD} = 1.2$  V. These values are obtained thanks to the 3D configuration of the vertically stacked channels and the enhanced impact of lateral conduction with small gate width. However,  $I_{OFF}$  is still high due to the non-optimized threshold voltage on those samples. When normalized at  $V_{OFF}+V_{DD}$ , the  $I_{ON}$ -currents are 3.3 mA/ $\mu\text{m}$  for nFET and 2.0 mA/ $\mu\text{m}$  for pFET. When normalized by  $W_{total}$ , the  $I_{ON}$ -currents at  $V_{OFF}+V_{DD}$  for n- and p-FET are 538  $\mu\text{A}/\mu\text{m}$  and 396 $\mu\text{A}/\mu\text{m}$ , respectively. These normalized  $I_{ON}$  values are comparable to planar fully depleted – SOIFETs when using the same (unoptimized) gate stack [4.7].

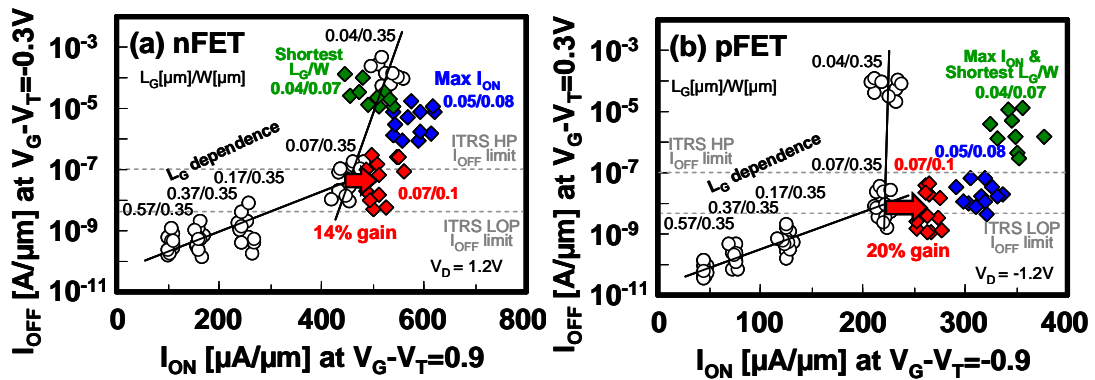


Figure 4.10  $I_{ON}$ - $I_{OFF}$  characteristics with several channel sizes for nMCFET (a) and pFET (b).

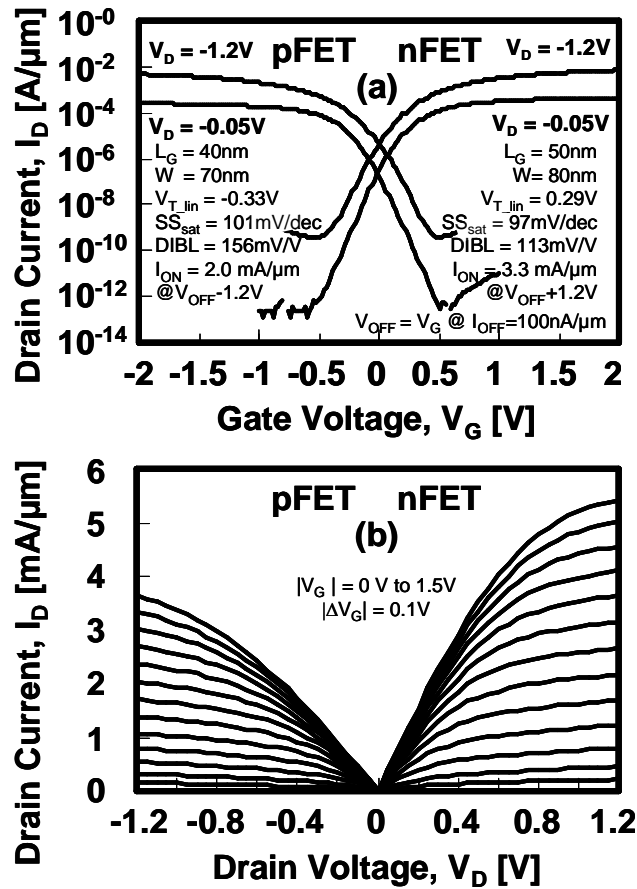


Figure 4.11  $I_D$ - $V_G$  (a) and  $I_D$ - $V_D$  (b) characteristics for the scaled MCFETs.

## 4.4 CONCLUSIONS

The influence of in situ doped SEG source and drain has been examined for vertically aligned MCFETs. A large enhancement, by a factor of 2 in the drive current, can be obtained when in situ doped SEG process is adopted. Detailed parameter extraction from the electrical measurements shows that the  $R_{SD}$  values can be reduced by 90 and 75% for  $n$ - and  $p$ -MCFETs, respectively, when in situ doped SEG is reinforced by adding ion implantation. On the other hand,  $V_T$  roll-off characteristics and the effective mobility behavior are slightly degraded, especially when ion implantation is combined to the SEG process. Mobility analysis has revealed an increase in the Coulomb scattering with  $L_G$  scaling, indicating the diffusion of dopant atoms from S/D regions. These results indicate an avenue to further improve the performance by optimizing the S/D activation annealing step.

## 4.5 REFERENCES

- [4.1] E. Bernard T. Ernst, B. Guillaumot, N. Vulliet, T. C. Lim, O. Rozeau. F. Danneville, P. Coronel, T. Skotnicki, S. Deleonibus, O. Faynot, First Internal Spacers' Introduction in Record High  $I_{ON}/I_{OFF}$  TiN/HfO<sub>2</sub> Gate Multichannel MOSFET Satisfying Both High-Performance and Low Standby Power Requirements, *IEEE Elec. Dev. Lett.*, 30 (2) (2009) pp. 148–151.
- [4.2] S.-Y. Lee, E.-J. Yoon, D.-S. Shin, S.-M. Kim, S.-D. Suk, M.-S. Kim, D.-W. Kim, D. Park, K. Kim and B.-il Ryu, Sub-25nm Single-Metal Gate CMOS Multi-Bridge-Channel MOSFET (MBCFET) for High Performance and Low Power Application, *Tech. Dig. Symp. VLSI Tech.* (2005) pp. 154–155.
- [4.3] K. Tachi, N. Vulliet, S. Barraud, B. Guillaumot, V. Maffini-Alvaro, C. Vizioz, C. Arvet, Y. Campidelli, P. Gautier, J.M. Hartmann, T. Skotnicki, S. Cristoloveanu, H. Iwai, O. Faynot and T. Ernst, "3D Source/Drain Doping Optimization in Multi-Channel MOSFET," 40th European Solid-State Device Research Conference (ESSDERC), pp. 368, 2010, Spain.
- [4.4] G. Bidal, D. Fleury, G. Ghibaudo, F. Boeuf, and T. Skotnicki, Guidelines for MOSFET Device Optimization accounting for L-dependent Mobility Degradation, *IEEE Silicon Nanoelectronics Workshop*, (2009) pp. 5–6.
- [4.5] K. Inoue, F. Yano, A. Nishida, T. Tsunomura, T. Toyama, Y. Nagai and M. Hasegawa, Three dimensional characterization of dopant distribution in polycrystalline silicon by laser-assisted atom probe, *Appl. Phys. Lett.* 93 (2008) 133507.
- [4.6] E. Bernard *et al.*, "Novel integration process and performances analysis of Low Standby Power (LSTP) 3D multi-channel CMOSFET (MCFET) on SOI with metal / high-K gate stack," in *VLSI Symp. Tech. Dig.*, 2008, pp. 16-17, 17–19.
- [4.7] F. Andrieu *et al.*, "Comparative scalability of PVD and CVD TiN on HfO<sub>2</sub> as a metal gate stack for FDSOI CMOSFET down to 25 nm gate length and width," in *IEDM Tech. Dig.*, 2006, pp. 641–644.

# **CHAPTER 5**

## ***CARRIER TRANSPORT PROPERTIES OF VERTICALLY- STACKED NANOWIRE MOSFETS***

# CHAPTER 5 CONTENTS

## **5 Carrier Transport Properties of Vertically-Stacked Nanowire MOSFETs**

- 5.1 Introduction
- 5.2 Electrical Characteristics
  - 5.2.1  $I$ - $V$  Characteristics
  - 5.2.2 Transport Limiting Velocity
  - 5.2.3 Carrier Mobility Evaluation
  - 5.2.4 Mobility Limiting Factors
- 5.3 Impact on Plasma Etching of SiGe Sacrificial layers
  - 5.3.1 One-Leveled Nanowire MOSFET Fabrication
  - 5.3.2 Carrier Mobility Evaluation
- 5.4 Effect of Hydrogen Annealing
  - 5.4.1 Cross-Sectional Shape
  - 5.4.2 Carrier Mobility Evaluation
  - 5.4.3 Interface Trap density
- 5.5 SiGe Nanowire MOSFET
  - 5.5.1 Device Fabrication Process
  - 5.5.2  $I$ - $V$  Characteristics
  - 5.5.3 Carrier Mobility Evaluation



5.5.4 Noise Measurement

5.6 Conclusions

5.7 References

## **5.1 INTRODUCTION**

To achieve devices with both high speed and low power consumption for future LSI applications, GAA SNWTs are one of the promising candidates because of their strong short-channel effect immunity. Moreover, to increase the drive current per unit area with the higher density for integration, vertical stacking of NWs enables the use more available silicon surface per device. Recently, short channel GAA-SNWTs have been successfully fabricated with diameter of less than 10 nm using several top-down CMOS compatible processes; they successfully suppress the short-channel effects. On the other hand, transport property degradation in SNWTs was also reported by several groups. However, the mobility behavior when the width is reduced has been remained unclear. Carrier transport in SNW is commonly discussed in terms of two main mechanisms; one is one-dimension (1-D) transport model, and the other is a facet-dominated transport model. The former can be adapted to sub-10 nm diameter, and the latter to larger one. From the fabrication process viewpoints, (dispersion, yield rate), a larger diameter is production friendly, provided that the short-channel effects under aggressively scaled gate length are suppressed.

In this chapter, carrier transport limiting components for vertically-stacked nanowire MOSFETs will be discussed to obtain better performance with suppressing short channel effects.

## **5.2 ELECTRICAL CHARACTERISTICS**

### **5.2.1 $I$ - $V$ Characteristics**

The measured  $I_D$ - $V_D$  (Figure 5.1) and  $I_{DS}$ - $V_{GS}$  (Figure 5.2) characteristics for vertically-stacked 15 nm width SNWTs with 32 nm effective gate length ( $L_{eff}$ ) for NMOS and 42 nm for PMOS show well-behaved characteristics.  $I_D$ - $V_G$  curves exhibit an excellent subthreshold slope (64 mV/dec for NMOS and 74 mV/dec for PMOS) and very low Drain Induced Barrier Lowering (32mV/V for NMOS and 62 mV/V for PMOS). On-currents  $I_{ON}$  (normalized by total circumference) of 840  $\mu$ A/ $\mu$ m and 540

$\mu\text{A}/\mu\text{m}$  with  $I_{OFF}$  of 4 nA/ $\mu\text{m}$  and 96 nA/ $\mu\text{m}$  are obtained for NMOS and PMOS, respectively. Comparable results were obtained in FDSOI FET. When the currents are normalized by top-view width, the  $I_{ON}$  for NMOS is 7.2 mA/ $\mu\text{m}$  for NMOS and 4.7 mA/ $\mu\text{m}$  for PMOS, showing the interest of 3-D devices to increase current density for a given layout. These extremely high currents are due to the vertically stacked structure. The devices showed excellent SCEs immunity as seen in Figure 5.3–5.6. Figure 5.7 shows drain currents as a function of  $L_{eff}$ . Gate length scaling is still effective down to sub-50nm  $L_{eff}$ .

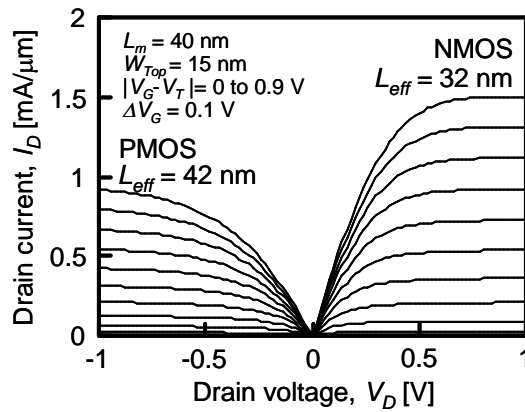


Figure 5.1  $I_D$ - $V_D$  characteristics of vertically-stacked silicon nanowire *n*- and *p*-MOSFET with sub-50-nm- $L_{eff}$  and 15-nm- $W_{Top}$ .

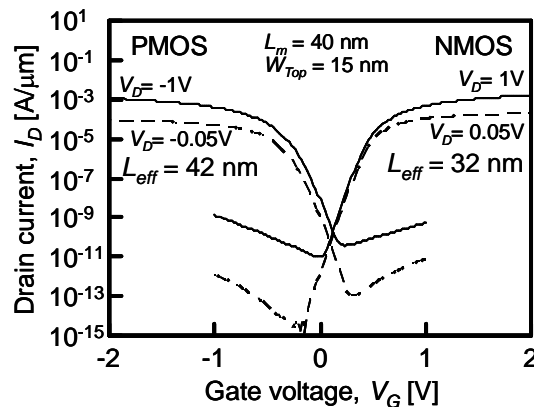


Figure 5.2  $I_D$ - $V_G$  characteristics of vertically-stacked silicon nanowire *n*- and *p*-MOSFET with sub-50-nm- $L_{eff}$  and 15-nm- $W_{Top}$ .

Table 5.1 Device parameters for vertically-stacked silicon nanowire n- and p-MOSFET with sub-50-nm- $L_{eff}$  and 15-nm- $W_{Top}$ . The on-currents  $I_{ON}$  are extracted at  $V_G - V_T = 0.7$  and  $-0.7$  V for n- and p-MOSFETs, respectively. The off-currents  $I_{OFF}$  are extracted at  $V_G - V_T = -0.3$  and  $0.3$  V for n- and p-MOSFETs, respectively.

	NMOS	PMOS
NW cross-section	3-level-stacking	
Max $W_{NW}/H_{NW}$	15nm/14nm	
$L_m$ [nm]	40	
$L_{eff}$ [nm]	32	42
EOT [nm]	1.7	1.7
$V_{DD}$ [V]	1	1
$I_{ON}/W_{eff}$ [mA/mm]	840	540
$I_{ON}/W_{Top}$ [mA/mm]	7.2	4.7
$I_{ON}/I_{OFF}$	$\sim 2 \times 10^5$	$\sim 6 \times 10^3$
$V_{Tsat}$ [V]	0.50	-0.37
DIBL [mV/V]	32	63
S.S. <sub>sat</sub> [mV/dec]	64	73

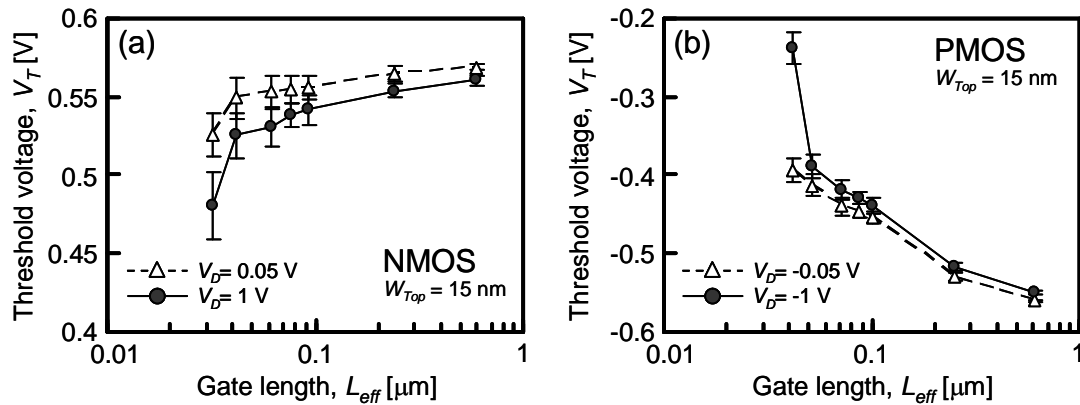


Figure 5.3 Threshold voltage as a function of effective gate length for vertically-stacked silicon nanowire n- and p-MOSFET with 15-nm- $W_{Top}$ .

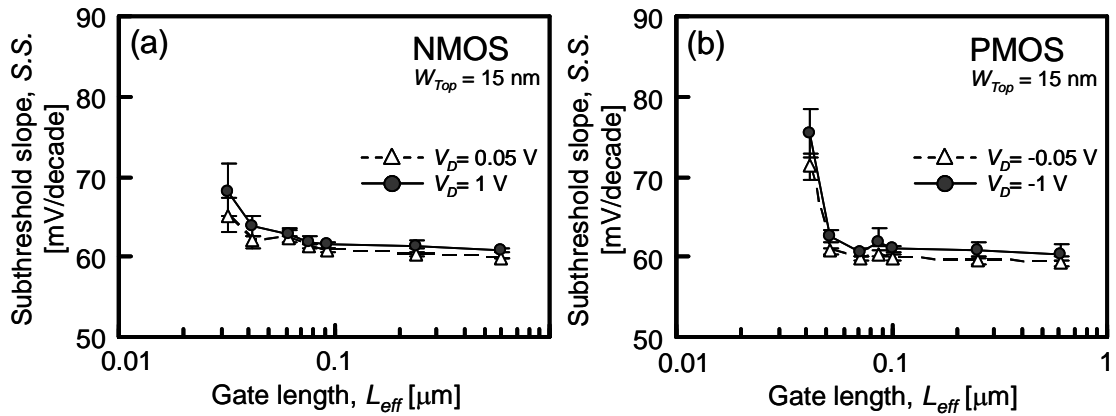


Figure 5.4 Subthreshold slope as a function of effective gate length for vertically-stacked silicon nanowire n- and p-MOSFET with 15-nm- $W_{Top}$ .

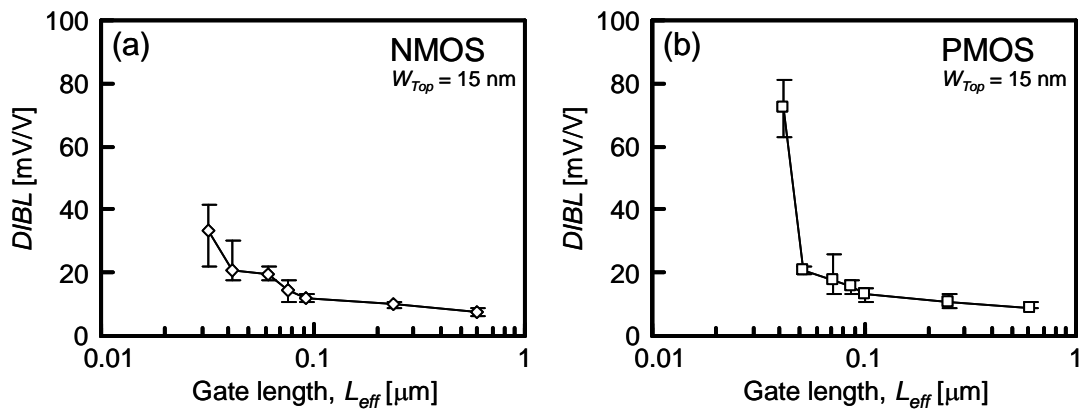


Figure 5.5 Drain-induced barrier lowering (DIBL) as a function of effective gate length for vertically-stacked silicon nanowire n- and p-MOSFET with 15-nm- $W_{Top}$ .

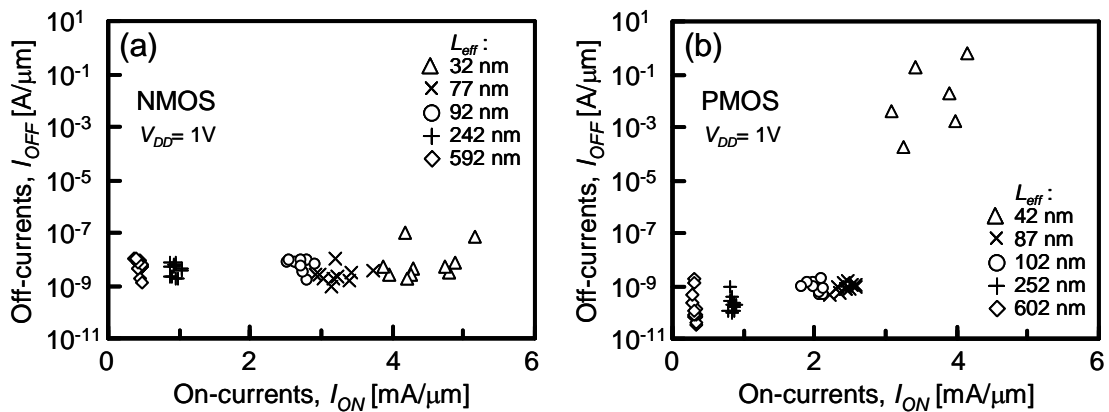


Figure 5.6  $I_{ON}$ - $I_{OFF}$  characteristics of vertically-stacked silicon nanowire n- and p-MOSFET with 15-nm- $W_{Top}$ .

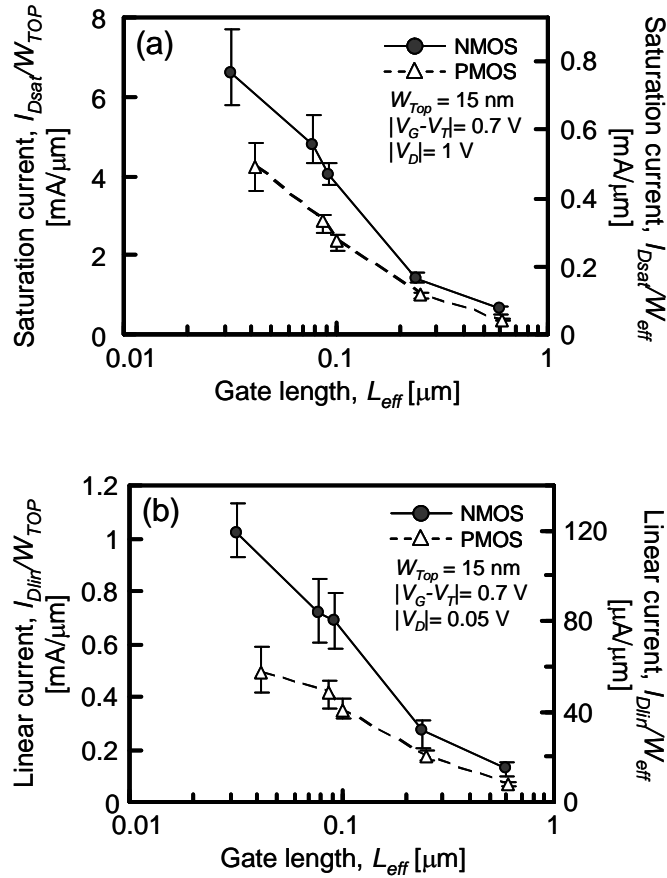


Figure 5.7 Saturation current density (a) and linear current density (b) as a function of effective gate length for vertically-stacked silicon nanowire n- and p-MOSFET with 15-nm- $W_{Top}$ . The currents are normalized by top-view width  $W_{Top}$  (left y-axis) and effective total width  $W_{eff}$  (right y-axis).

## 5.2.2 Transport Limiting Velocity

In thermal equilibrium conditions, carriers can be injected from the source reservoir to the channel with a thermal velocity. The part ( $r$ ) of injected carriers can be elastically backscattered towards the source, whereas the  $(1-r)$  part propagates towards the drain. Therefore, the effective source injection velocity ( $v_{inj}$ ) is smaller than thermal velocity. In the linear regime (small lateral field), the injection velocity, resulting from forwarded and backscattered fluxes and given by the ratio  $(1-r)/(1+r)$ , will be the only limitation of the total drain current, this being called the quasi-ballistic transport. However for high lateral electric field, saturation velocity  $v_{sat}$  resulting from optical phonon-electron interactions may constitute a stronger limitation than injection velocity.

Therefore, whatever the conduction regime (linear or on-state), there exists a certain limiting velocity that can be expressed as:  $v_{lim} = \min(v_{sat}, v_{inj})$ . This simple reasoning gives ground for a unification of all transport mechanisms, within one universal and continuous drain current model that is a kind of Matthiessen's rule. Since  $v_{sat}$  and  $v_{inj}$  have very close values, it is difficult to identify the true limiting mechanism. Fortunately, the temperature dependences of  $v_{sat}$  and  $v_{inj}$  are opposed, and thus they can reveal the limiting mechanism [5.1].

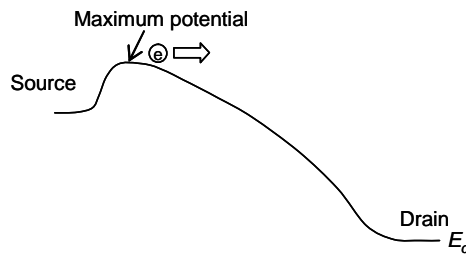


Figure 5.8 Schematic image of conduction band

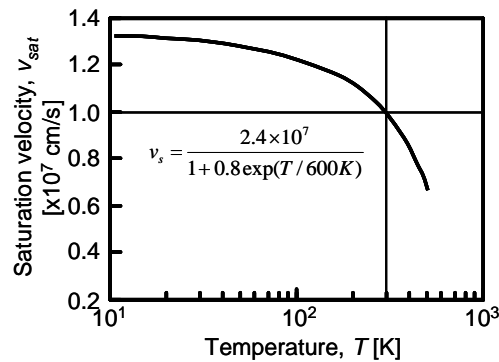


Figure 5.9 Temperature dependence of saturated electron drift velocity [5.2].

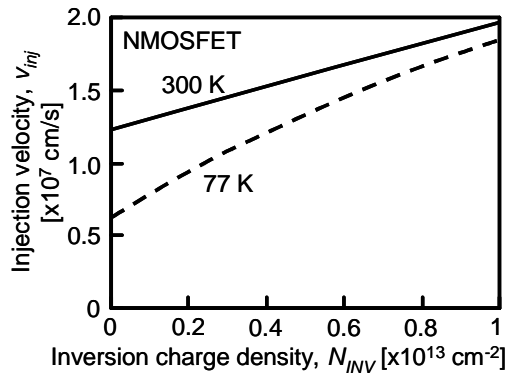


Figure 5.10 Injection velocity of a NMOSFET on (100) plane as a function of inversion charge density at 300 and 77 K. [5.3].

Low field mobility  $\mu_0$  is degraded with decreasing  $L_{eff}$  as shown in Figure 5.11. One of the possible reasons is the ballistic motion of carriers [5.4]. The part of injected carriers can ballistically reach drain. Indeed, the mobility experimentally extracted can be limited by ballistic transport. Thanks to the temperature dependence of both saturation velocity and injection velocity, the nature of the transport can be evidenced by plotting the temperature dependence of the limiting velocity. The temperature dependence of  $I_{DS}$ - $V_{GS}$  curves for the SNWT with  $L_{eff}$  of 32 nm is shown in Figure 5.12. The temperature range is from 5 to 300 K. The threshold voltage decreases with temperature, while the sub-threshold slope increases. These changes in  $V_T$  and  $SS$  with temperature are mainly due to band gap changes and are consistent with the theory. Figure 5.13 shows temperature dependence of  $v_{lim}$  for NMOS. It is clear that the vertically-stacked SNWTs are almost exclusively  $v_{sat}$  limited. This result implies high backscattering rate and the presence of strong scattering components.

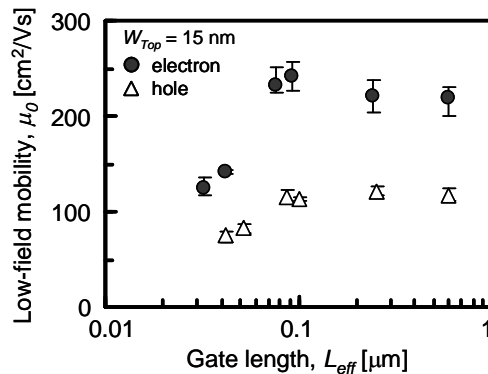


Figure 5.11 Low-field mobility  $\mu_0$  as a function of effective gate length for vertically-stacked silicon nanowire n- and p-MOSFET with 15-nm- $W_{Top}$ .

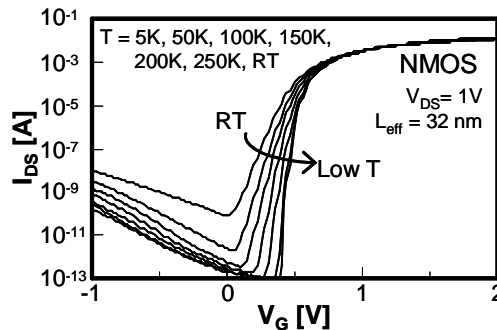


Figure 5.12 Temperature dependence of  $I_D$ - $V_G$  characteristics for vertically-stacked SNWTs.



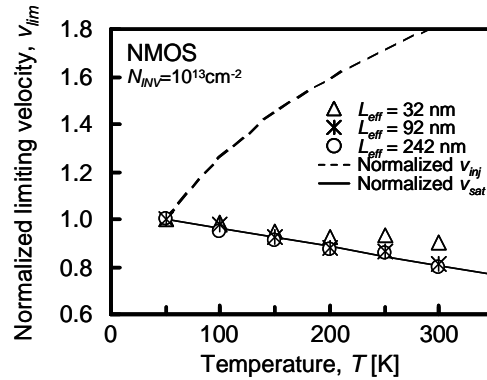


Figure 5.13 Temperature dependence of extracted limiting velocity  $v_{lim}$ . Theoretical dependence of saturation velocity  $v_{sat}$  from [5.5] and injection velocity  $v_{inj}$  from [5.6] are given.

### 5.2.3 Carrier Mobility Evaluation

Figure 5.14 shows possible carrier transport limiting factors intrinsically for silicon nanowire transistor. In general, the carrier mobility in two-dimensional (2-D) transport for planar FET strongly depends on its surface orientations due to the effective mass difference. The electron mobility on (100)-surface is about two times as high as that on (110)-surface, while the hole mobility is opposite. The rectangular nanowires directed to  $\langle 110 \rangle$  have two oriented surfaces, that is, (100)-surface for the top and bottom channels and (110)-surface for the side channels. In that case, as shrinking the wire width, that is, the (100)-surface, it is expected that the electron mobility decreases, while the hole mobility increase as shown in Figures 5.14 (b) and 5.15. Moreover, in silicon nanowire with less than 10 nm in diameter, carrier transport will become one-dimension (1-D). In that case, it is expected that carrier limiting components show different behaviors from two-dimensional transport as shown in Figure 5.14 (c). In addition, as nanowire width decreases, transport property at the corners for rectangular shaped nanowires becomes dominant. The carriers at the corners could possibly behave like one-dimensional transport depending radius of curvature as shown in Figure 5.14 (d) and 5.16. As the results of those carrier transport limiting factors, the experimentally extracted mobility is difficult to understand if the degradation is due to the extrinsic causes. In this study, mobility limiting components in silicon nanowires will be investigated in detail by observing temperature dependence of the mobility.

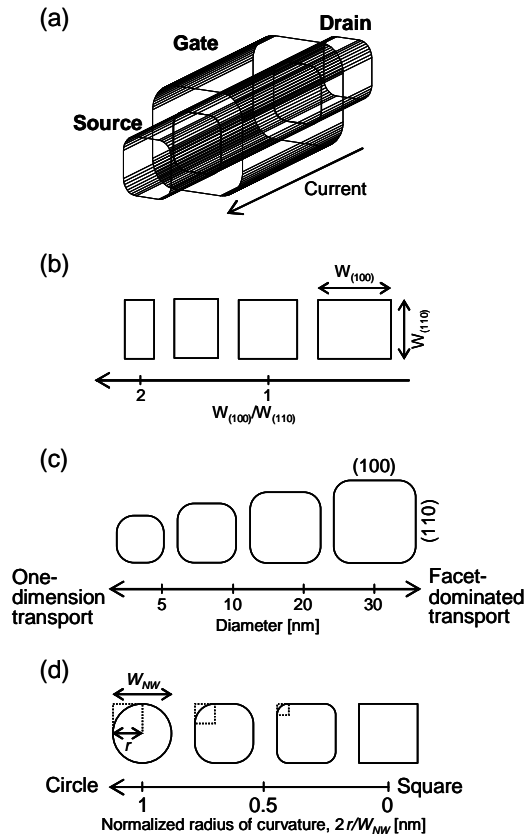


Figure 5.14 Schematic image of nanowire MOSFET (a) and its cross-section: (b) varying ratio of (100) width to (110) width, (c) varying size, (d) varying radius of curvature at the corners.

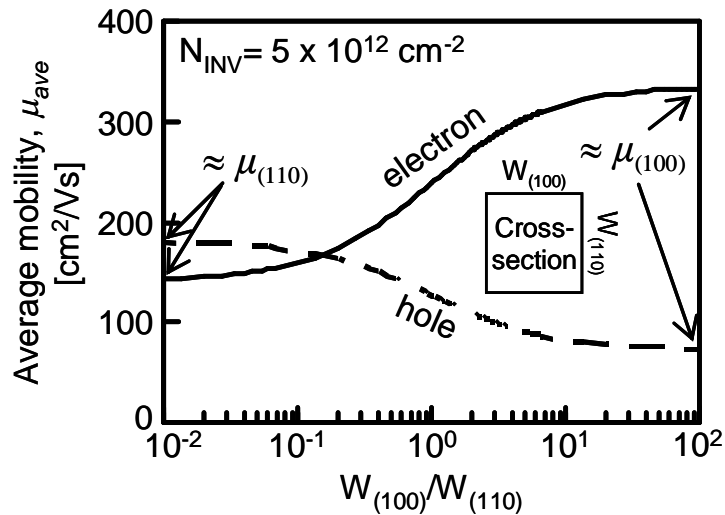


Figure 5.15 Nanowire mobility as a function of  $W_{(100)}$ -to-  $W_{(110)}$  ratio. The average mobility is  $\mu_{ave} = (\mu_{(100)}W_{(100)} + \mu_{(110)}W_{(110)}) / (W_{(100)} + W_{(110)})$ , where  $\mu_{(100)}$  and  $\mu_{(110)}$  are the mobilities on (100) and (110) surfaces, respectively.

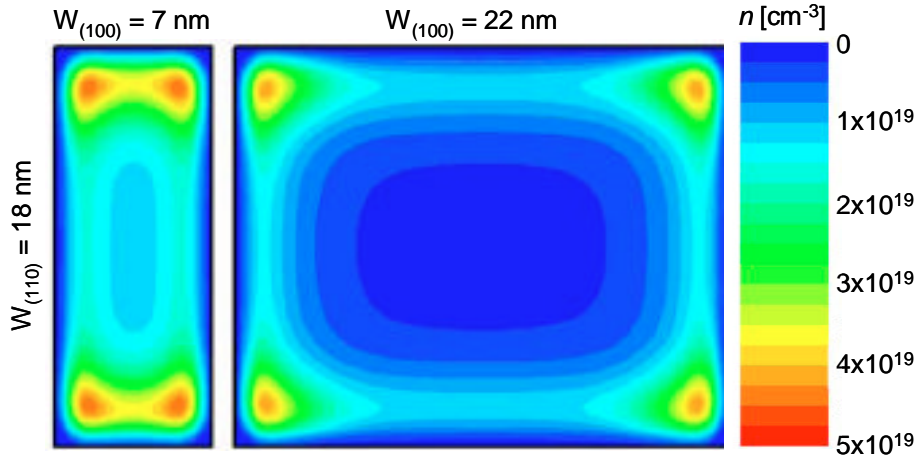


Figure 5.16 Calculated profiles of electron density across the cross section of silicon nanowires with  $W_{(110)}=18$  nm, and  $W_{(100)}= 7$  and  $22$  nm [5.7].

Since the backscattering rate is directly related to the mobility, it is important to examine the temperature dependence of mobility to quantify the contribution of each scattering mechanism. Figures 5.17 show effective mobility for electrons in vertically stacked SNWTs and fully-depleted SOI FET as a function of inversion charge density at different temperatures. It is clear that the electron mobility dependence on temperature for the SNWT is much lower than that for FDSOI. In addition, the electron mobility dependence on temperature is also much lower than that for hole. In general, mobility in MOSFETs is limited by three scattering components; coulomb, phonon, and surface roughness as shown in Figure 5.19 (b). The coulomb- $(\mu_{cb})$  and phonon- $(\mu_{ph})$  limited mobilities have negative and positive contribution at low temperature, respectively. Meanwhile, the surface roughness-limited mobility  $(\mu_{sr})$  does not depend on temperature. At low temperature, mobility is limited by only the coulomb scattering only at low  $N_{inv}$  and only by the surface-roughness scattering only at high  $N_{inv}$ . Figure 5.19 (a) shows effective mobility for electron and hole at high  $N_{inv}$  as a function of temperature. The  $\mu_{sr}$  values can be extracted by extrapolating the mobility at 10 K. The  $\mu_{sr}$  values for vertically-stacked SNWTs are much smaller than that for FDSOI. Phonon limited mobility can be extracted by using Matthiessen's rule and the extracted  $\mu_{sr}$ . Figure 5.21 shows comparison of mobility limiting components at high  $N_{INV}$ . It is clear

that electron effective mobility is strongly limited by surface roughness scattering, while hole mobility is limited by both surface roughness and phonon scattering at high  $N_{INV}$ . In Figure 5.22, electron mobility at low  $N_{inv}$  is degraded at lower temperatures. This indicates that electron mobility at low  $N_{inv}$  in vertically-stacked SNWTs is limited by coulomb scattering. On the other hand, hole mobility increase at low temperature. This means that phonon scattering is dominant at low  $N_{INV}$ . Mobility for vertically-stacked SNWTs is degraded due to surface roughness. The surface roughness could be one of the key factors to obtain high performance.

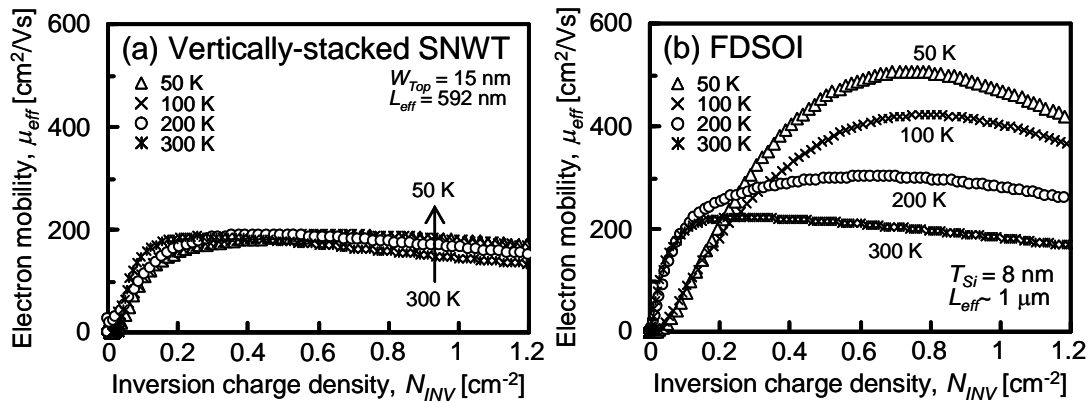


Figure 5.17 Temperature dependence of effective electron mobility in vertically-stacked silicon nanowire FET (a) and in fully-depleted SOI-FET (b).

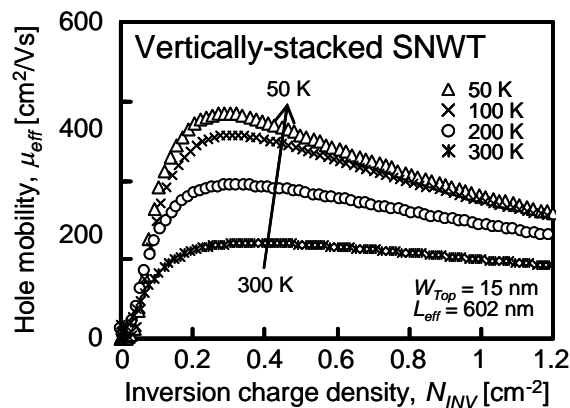


Figure 5.18 Temperature dependence of effective hole mobility in vertically-stacked silicon nanowire FET.

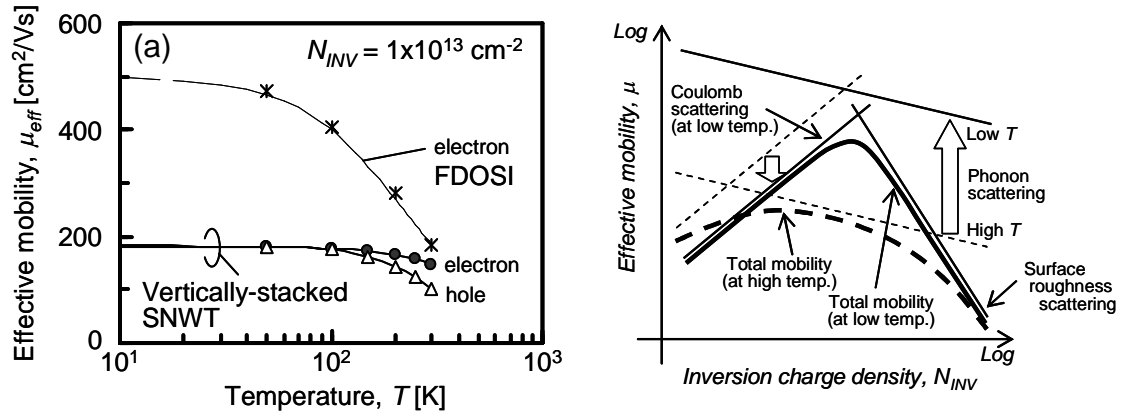


Figure 5.19 (a) Temperature dependence of effective mobility at high inversion charge density ( $N_{INV} = 10^{13}$  cm<sup>-2</sup>). (b) Schematic diagram of mobility limiting components at low temperature.

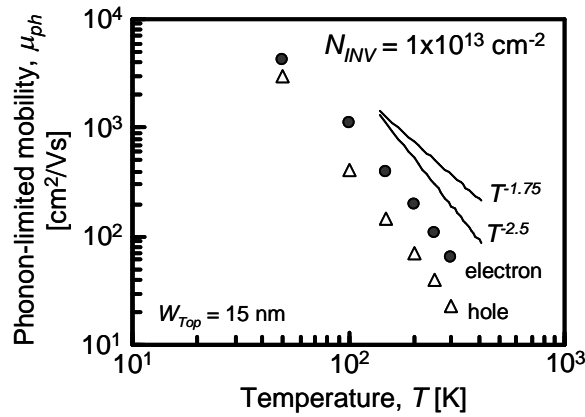


Figure 5.20 Temperature dependence of phonon-limited mobility at high inversion charge density ( $N_{INV} = 10^{13}$  cm<sup>-2</sup>) for vertically-stacked silicon nanowire MOSFETs.

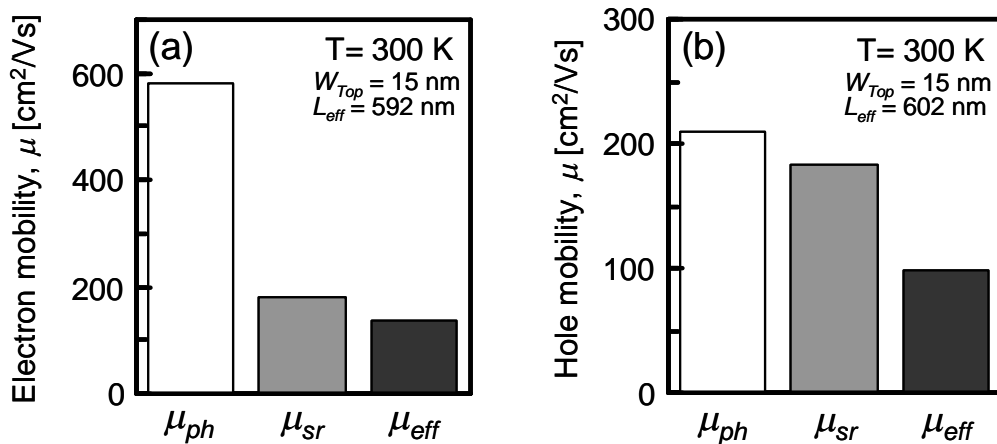


Figure 5.21 Mobility limiting components for electron (a) and hole for vertically-stacked silicon nanowire MOSFETs at 300 K.

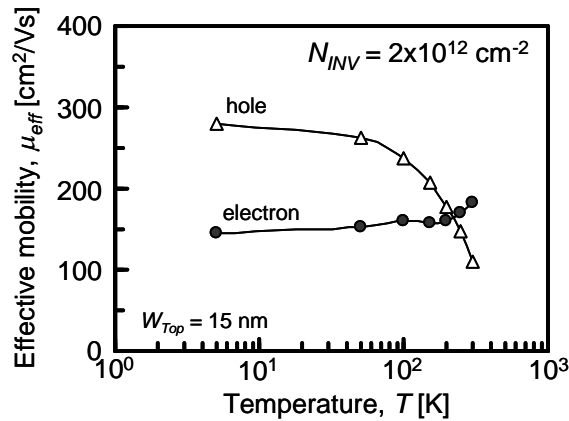


Figure 5.22 Temperature dependence of effective mobility at low inversion charge density ( $N_{INV}=2 \times 10^{12} \text{ cm}^{-2}$ ).

### 5.3 IMPACT ON PLASMA ETCHING OF SILICON-GIRMANIUM SACRIFICIAL LAYERS

One of the possible reasons of degraded surface-roughness limited mobility is damage due to the selective SiGe dry and isotropic etching. According to results reported by C. Dupre *et al.* [5.8], Si planar NMOS transistors have been roughened using an isotropic plasma etching, similar to the one used for SON technologies. AFM was used to evaluate the RMS of damaged Si surfaces as shown in Figure 5.23 and 5.24. In this section, impact on plasma etching of SiGe sacrificial layers for vertically-stacked SNWTs is investigated. To compare between with and without the plasma etching, one-level SNWTs were fabricated without SiGe sacrificial layer.

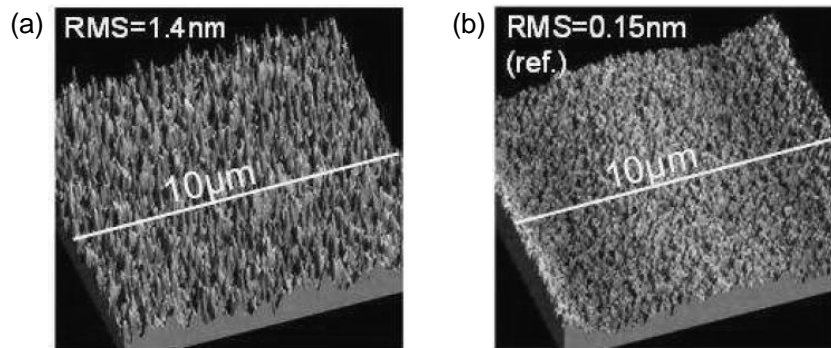


Figure 5.23 Atomic force microscopy images of silicon surface after isotropic SiGe dry etching (a) and the reference sample without the etching (b).

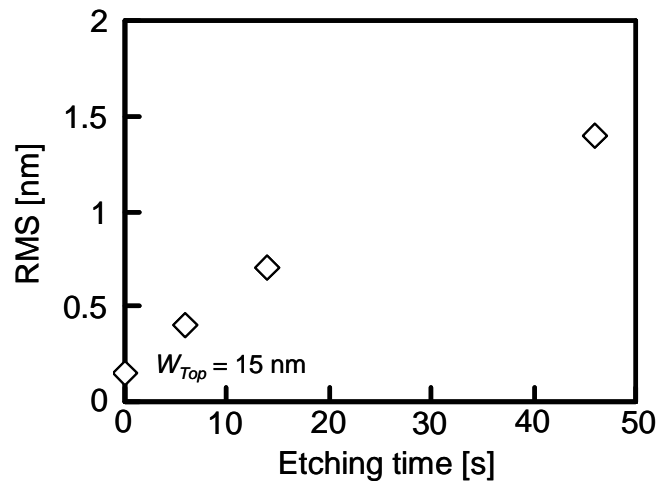


Figure 5.24 Root mean square (RMS) values as a function of isotropic SiGe dry etching.

### 5.3.1 One-Levelled Nanowire MOSFET Fabrication

In order to investigate the impact of the selective SiGe isotropic etching, one-level nanowire MOSFETs as reference are fabricated without SiGe epitaxy and etching process as shown in Figure 5.25. The NW diameter is controllable down to 5 nm by self limited oxidation [5.9] while keeping regularly arrayed NWs as shown in Figure 5.26 (a).

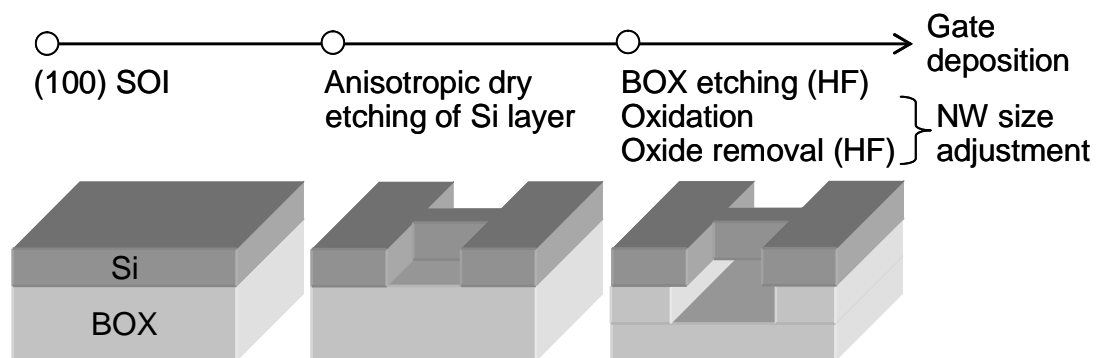


Figure 5.25 Brief process flow of 1-level silicon nanowire MOSFET.

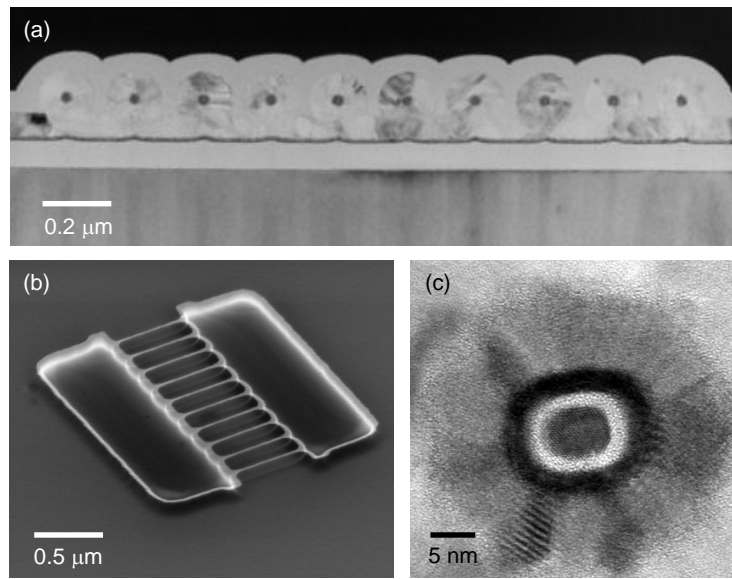


Figure 5.26 Gate-all-around 1-level silicon nanowire MOSFETs fabricated without SiGe epitaxy and selective etching.

### 5.3.2 Carrier Mobility Evaluation

Figure 5.27 shows effective mobility comparisons between vertically-stacked and 1-level SNWTs with 15 nm of  $W_{NW}$  at 300 K and 5 K. The 1-level SNWTs show higher mobility than vertically-stacked ones. The higher effective mobility at high inversion charge density in 1-level SNWTs means less surface-roughness scattering as shown in Figure 5.28–5.30. Moreover, in the case of 1-level SNWTs, coulomb scattering is less dominant as shown in Figure 5.31. The reason why stronger coulomb scattering is higher in stacked SNWTs may be the degraded interface quality with high-k because of the use of SiGe sacrificial layers. Additional surface treatments may thus be needed.

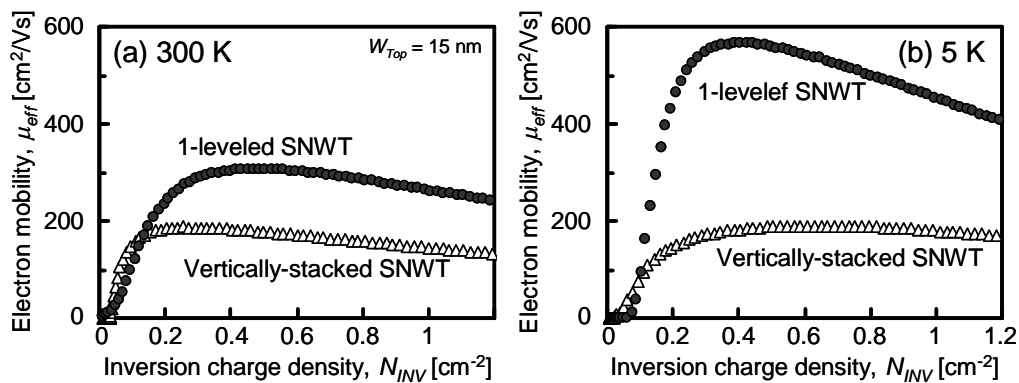


Figure 5.27 Electron mobility comparisons between 1-level and vertically-stacked silicon nanowire MOSFET at 300 K (a) and 5 K (b).



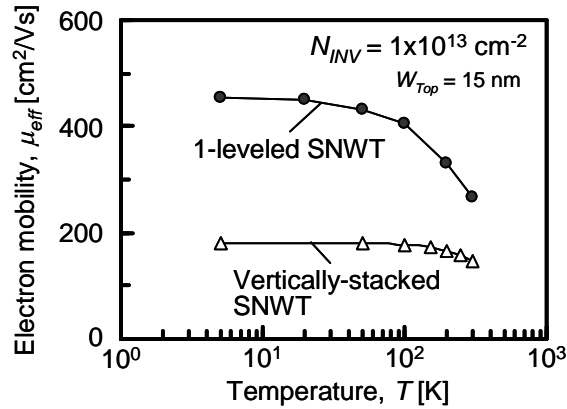


Figure 5.28 Temperature dependence of effective mobility at high inversion charge density ( $N_{INV}=10^{13} \text{ cm}^{-2}$ ) for 1-leveled and vertically-stacked silicon nanowire MOSFET.

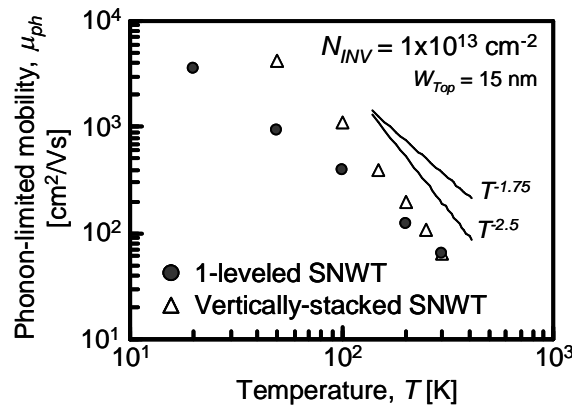


Figure 5.29 Temperature dependence of phonon-limited mobility at high inversion charge density ( $N_{INV}=10^{13} \text{ cm}^{-2}$ ) for 1-leveled and vertically-stacked silicon nanowire MOSFETs.

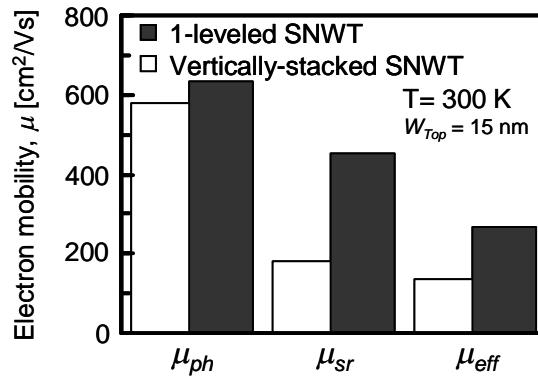


Figure 5.30 Mobility limiting components comparison at high inversion charge density between 1-leveled and vertically-stacked silicon nanowire MOSFETs at 300 K.

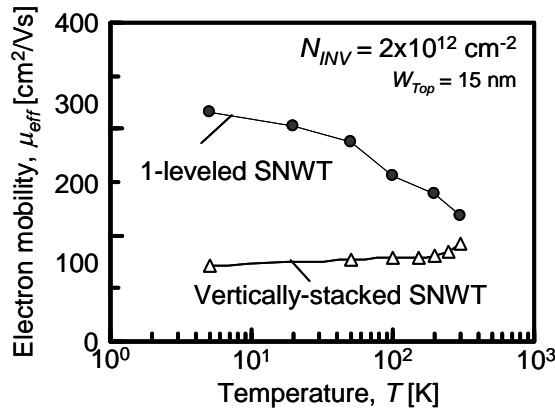


Figure 5.31 Temperature dependence of effective mobility at low inversion charge density ( $N_{INV}=2 \times 10^{12} \text{ cm}^{-2}$ ).

## 5.4 EFFECT OF HYDROGEN ANNEALING

Hydrogen annealing can, however, be used intentionally for three-dimensional profile transformation by rounding sharp corners while diminishing the surface roughness and keeping the active layer crystalline [5.10, 5.11]. In this section, a mobility study was performed in order to highlight the impact of hydrogen annealing on etched surfaces.

### 5.4.1 Cross-Sectional Shape

Hydrogen annealing (750°C, 2min) was performed on 15 nm wide Si nanowires (Figure 5.32 (a)). Si nanowires were rounded thanks to this specific process (Figure 5.32 (b)).

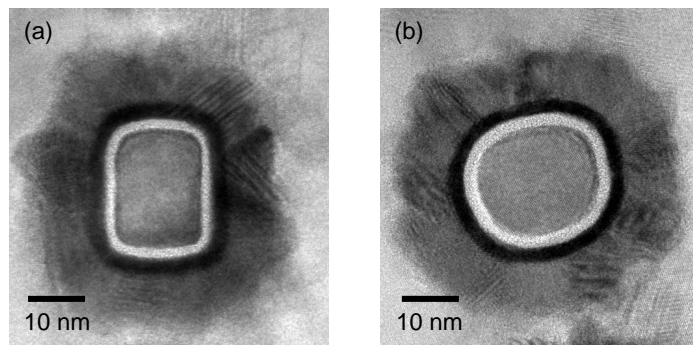


Figure 5.32 Cross-sectional TEM images of silicon nanowire (a) without and (b) with hydrogen annealing at 750 °C for two minutes.

### 5.4.2 Carrier Mobility Evaluation

First, the impact of H<sub>2</sub> annealing on NW surface quality was investigated by using 1-leveled SNWTs. Figure 5.33–5.36 show the comparisons of electron effective mobility between with and without hydrogen annealing. It is clear that effective mobility in H<sub>2</sub>-annealed SNWTs is more degraded by coulomb scattering, while surface roughness is improved. Figure 5.37 shows a mobility comparison between with and without hydrogen annealing for vertically-stacked SNWTs. A circular shape formed by hydrogen annealing leads to mobility degradation at low inversion charge density ( $N_{inv}$ ). Improvement of  $\mu_{eff}$  at high  $N_{inv}$  is however observed for circular NWs because their surface roughness is reduced by the H<sub>2</sub> annealing as well as 1-leveled SNWTs.

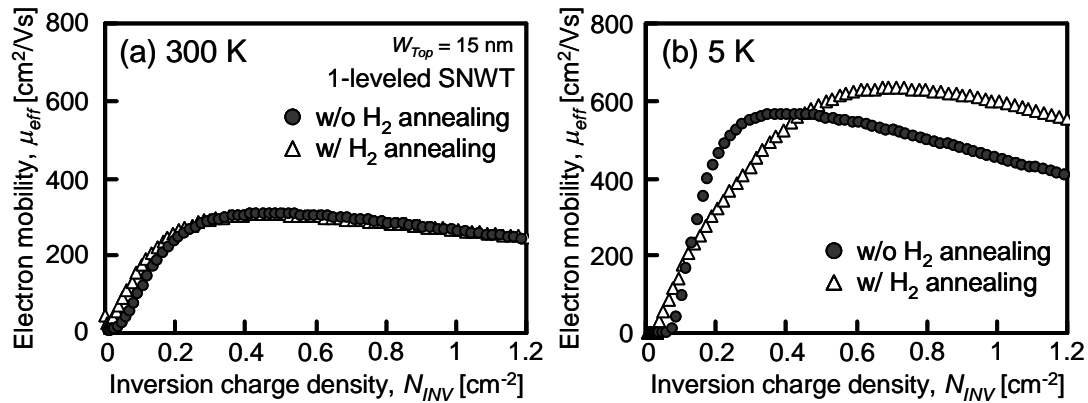


Figure 5.33 Electron mobility comparison of 1-leveled silicon nanowire MOSFETs between with and without hydrogen annealing. The measurement temperatures are 300 K (a) and 5 K (b).

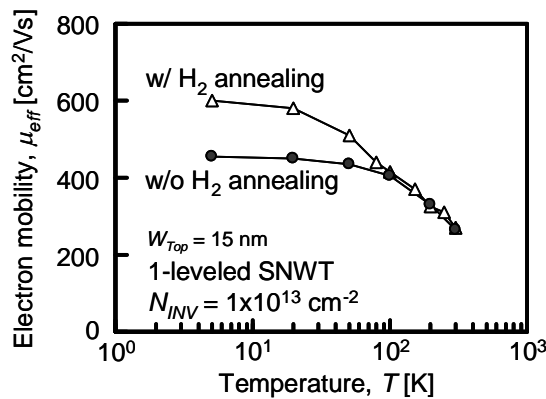


Figure 5.34 Temperature dependence of effective mobility at high inversion charge density ( $N_{INV}=10^{13} \text{ cm}^{-2}$ ) for 1-leveled nanowire MOSFET with and without H<sub>2</sub> anneal.

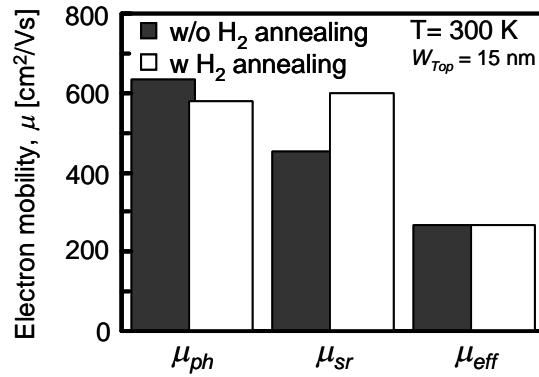


Figure 5.35 Mobility limiting components comparison at high inversion charge density and 300 K for 1-levelled silicon nanowire MOSFET between with and without hydrogen annealing.

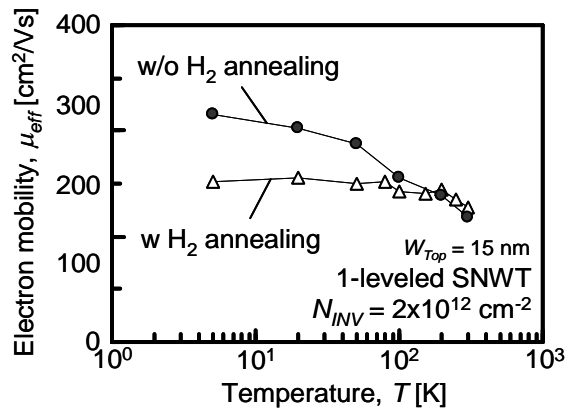


Figure 5.36 Temperature dependence of effective mobility at low inversion charge density ( $N_{INV}=2 \times 10^{12} \text{ cm}^{-2}$ ).

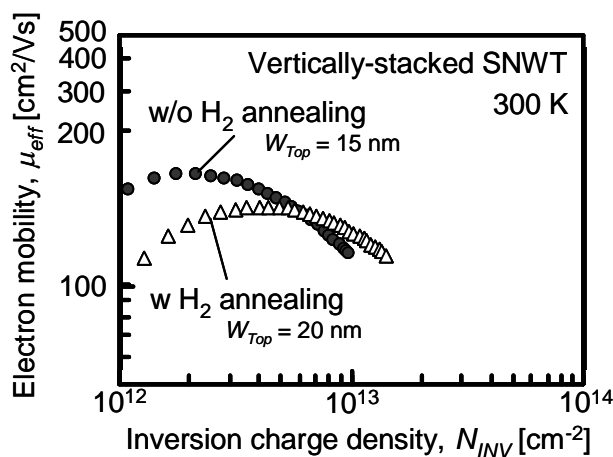


Figure 5.37 Electron mobility comparison of vertically-stacked silicon nanowire MOSFETs between with and without hydrogen annealing.

### 5.4.3 Interface Trap density

Mobility at low  $N_{inv}$  is mainly limited by (remote) coulomb scattering due to interface and oxide charges and/or interface dipoles between high- $k$  and interfacial layer in the case of high- $k$ /metal gate stack. To evaluate the interface quality, the interface trap density ( $D_{it}$ ) have been quantified by adapting the charge pumping method with gated-diode structures. Figure 5.38 shows the charge pumping current ( $I_{cp}$ ) in Si NWs which exhibits a typical ‘‘hat’’ shape. The peak  $I_{cp}$ -frequency ( $f$ ) plots shows a good linearity in Figure 5.39. Circular NWs have roughly 3 times higher mean  $D_{it}$  values than rectangular ones. Figure 5.40 show the energy profiles of  $D_{it}$  (obtained by temperature dependence of Si band gap). At both the upper and lower regions of the gap, the  $D_{it}$  of circular NWs is higher, leading to higher mean  $D_{it}$  values.

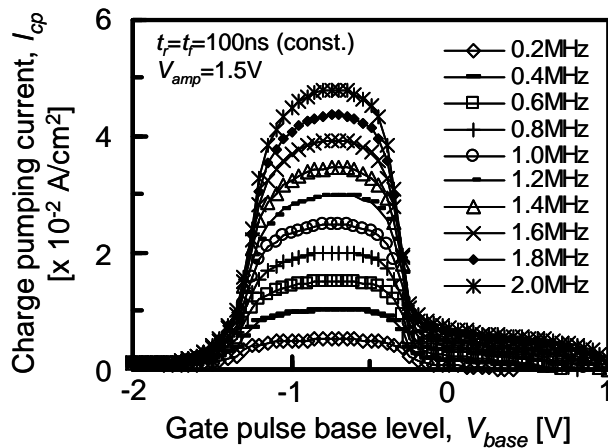


Figure 5.38 Charge pumping currents  $I_{cp}$  obtained base voltage sweep on nanowire gated-diode with  $L_G = 240$  nm and  $W_{NW}/H_{NW} = 20$  nm/15 nm. The currents are normalized by  $W_{eff}$  obtained from TEM images.

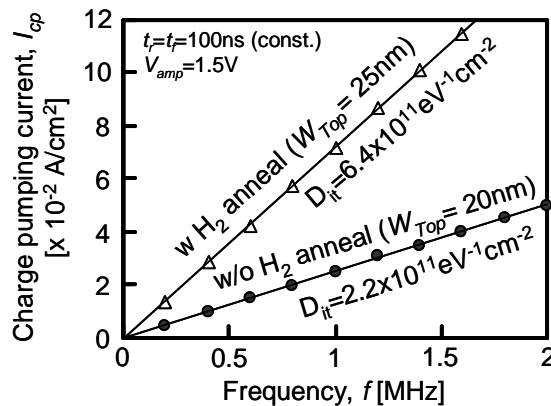


Figure 5.39 Charge pumping currents  $I_{cp}$  as a function of frequency  $f$ .

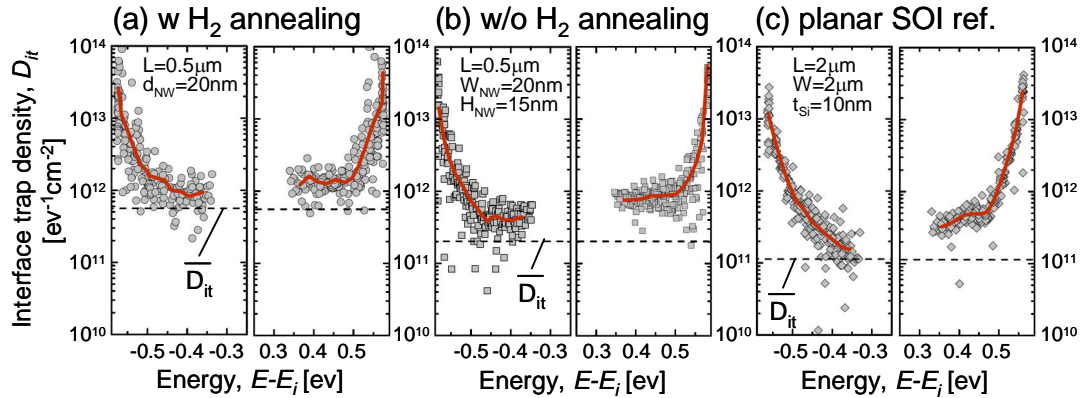


Figure 5.40 Interface trap density as a function of energy for vertically-stacked nanowires with (a) and without (b) hydrogen annealing, and planar SOI devices (c) with the same gate stack (3 nm  $\text{HfO}_2$  ALD/10 nm TiN CVD). The profile is obtained by scanning temperature from 300 K down to 25 K by 25 K steps. The bold line represents the mean value of  $D_{it}(E)$ . The dashed line is the directly measured mean value of interface trap density over the full energy range at 300 K which evidence the lower density of interface traps in the middle of the gap.

## 5.5 SILICON-GIRMANIUM NANOWIRE MOSFET

### 5.5.1 Device Fabrication Process

The fabrication process of vertically-stacked SiGe nanowire FETs was changed from Si ones as the following steps. SOI (001) wafers were used for Si and compressively (c)-strained SiGe NWs. Tensile-strained (1.3 GPa) SOI (001) wafers were used for un-strained SiGe NWs, respectively. After anisotropic etching of Si/Si<sub>0.8</sub>Ge<sub>0.2</sub> superlattices, isotropic etching of Si layers between Si<sub>0.8</sub>Ge<sub>0.2</sub> layers was performed to obtain the suspended Si<sub>0.8</sub>Ge<sub>0.2</sub> nanowires. In order to achieve better interface quality, a 2 nm-thick-Si cap was grown at 650 °C on the SiGe NWs.

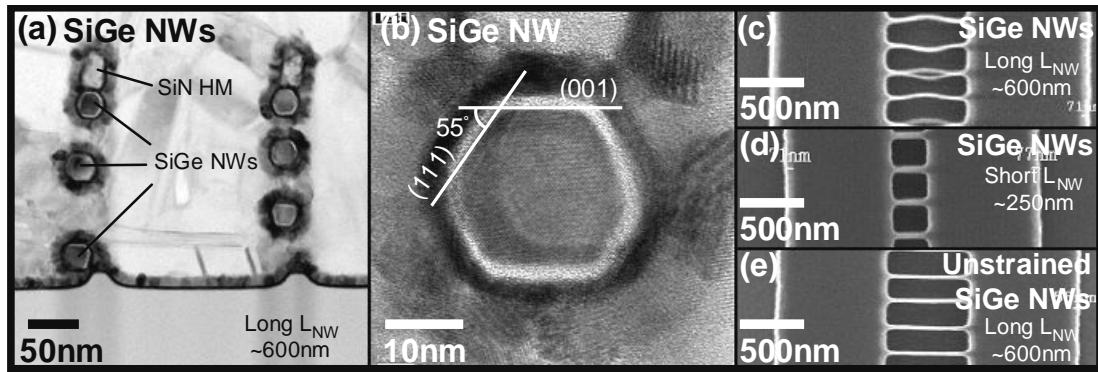


Figure 5.41 (a) Cross-sectional TEM micrographs of 3D-stacked compressively(c)-strained SiGe NWTs, (b) enlarged images of c-strained SiGe NW, (c) top view of bended c-strained SiGe NWs with  $L_{NW}=600nm$ , (d) top view of c-strained SiGe NWs with  $L_{NW}=250nm$ , and (e) top view of un-strained SiGe NWs with  $L_{NW}=600nm$ . Short length SiGe NWs are straight, this whatever their strain state.

### 5.5.2 I-V Characteristics

C-strained SiGe and un-strained SiGe NWs were evaluated in order to boost pFET performances. Figure 5.42 shows  $I_{ON}/I_{OFF}$  characteristics of Si, c-strained and un-strained SiGe NWs. The currents are normalized by the number of wires. Both the SiGe NWTs showed larger off-current than SNWTs. This is due to the lower  $V_T$  for the SiGe NWTs as shown in Figure 5.43. The c-strained SiGe NWTs show higher on-current. However the best  $I_{ON}/I_{OFF}$  performance is obtained for Si NWs.

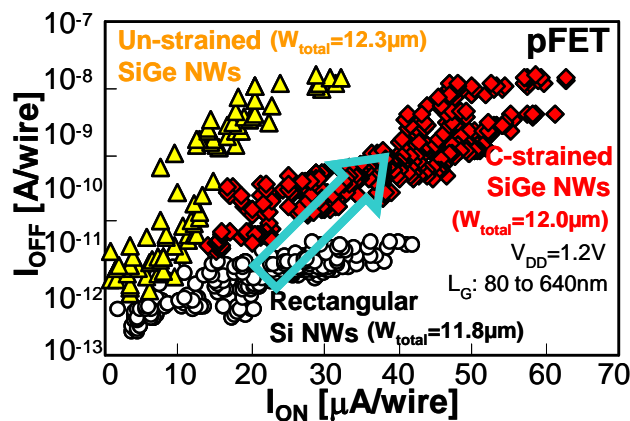


Figure 5.42  $I_{ON}/I_{OFF}$  characteristics of Si, c-strained and un-strained SiGe NWs normalized by the number of wires. The total NW surface  $W_{total}$  is estimated from the cross-sectional TEM images. The  $W_{NW}$  of all NWs is  $\sim 20nm$ .

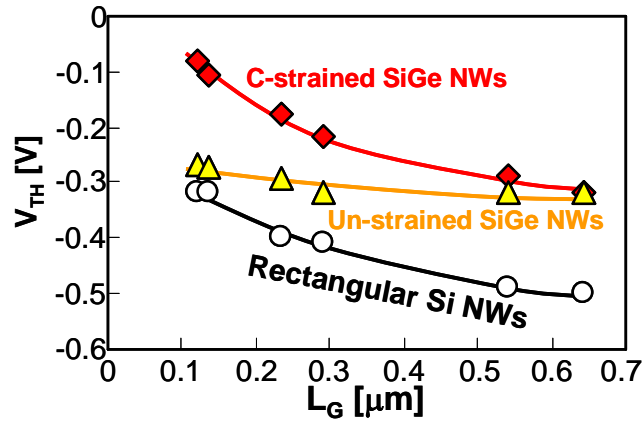


Figure 5.43 Threshold voltage of Si, c-strained and un-strained SiGe NWs as a function of gate length. The  $W_{NW}$  of all NWs are  $\sim 20\text{nm}$ .

### 5.5.3 Carrier Mobility Evaluation

Figure 5.44 shows a mobility comparison. The large enhancement of mobility was obtained in the c-strained SiGe NWTs compared with un-strained ones. This can be due to the compressive strain effect. However, in comparison with SNWTs, a small impact on mobility was observed. The c-strained SiGe NWTs have higher  $\mu_{eff}$  at high  $N_{inv}$  lead to a larger  $I_{ON}$  current than for Si NWTs. The hexagonal cross section of SiGe NWs with (111) sidewalls could also contribute to mobility degradation as shown in Figure 5.44.

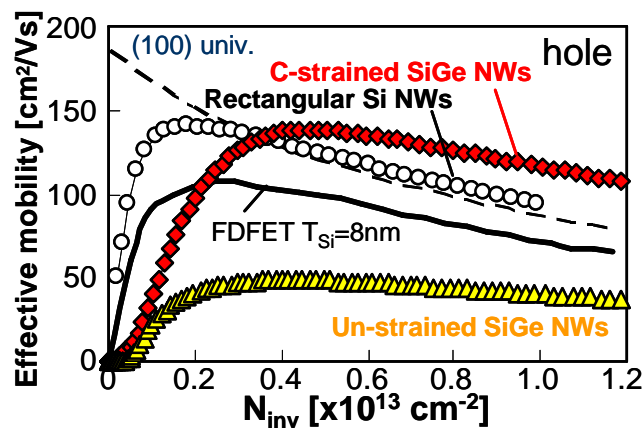


Figure 5.44 Effective hole mobility of Si, c-strained and un-strained SiGe NWs. The  $W_{NW}$  of all NWs are  $\sim 20\text{nm}$ .



### 5.5.4 Noise Measurement

Low-frequency noise measurements performed on the NWs between 10 Hz and 10 kHz at  $V_{DS}=50$  mV, show an oxide trap density ( $N_t$ ) for SiGe NWs 3.5 times larger than for Si NWs (Figure 5.45). This higher trap density may reduce the mobility.

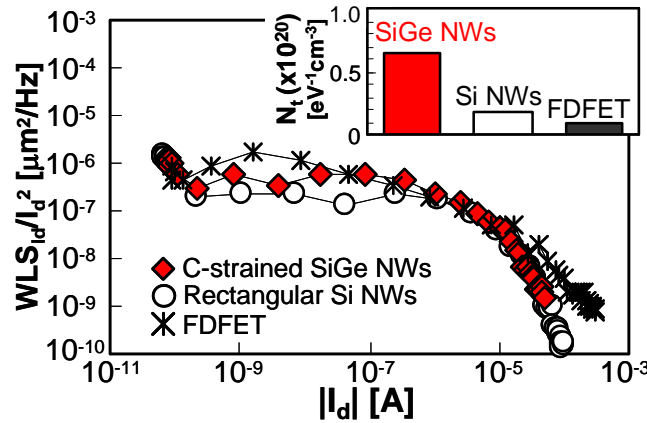


Figure 5.45 Low-frequency noise of Si and c-strained SiGe NWs. Inserted figure is a comparison of oxide trap density ( $N_t$ ).  $L_G$  and  $W_{NW}$  are  $\sim 290$ nm and  $\sim 20$ nm, respectively.

## 5.6 CONCLUSIONS

In this chapter, the electrical characteristics of vertically-stacked SNWTs have been investigated. Vertically-stacked nanowire structure can achieve extremely high on-currents per given layout surface with good short-channel effects immunity. This result is expected to achieve high integration and low power consumption. On the other hand, in terms of its performance, the optimisation of short-channel CMOS nanowire drive current will have to take into account specific effects. In particular, the use of SiGe sacrificial layer to make vertically-stacked channels cause the large mobility degradation due to the surface roughness, resulting from the damage of plasma etching. This result can evidence the poor ballisticity in the short channel SNWTs.

The hydrogen annealing can improve the surface-roughness limited mobility a little. Charge pumping measurements, however, revealed that circular-shaped SNWTs, which are formed by hydrogen annealing, have a higher  $D_{it}$  than rectangular ones, leading to low-field mobility degradation. This high  $D_{it}$  might be caused by the

continuously-varying surface orientation. The resulting additional coulomb scattering could partly explain the quite low mobility in 5 nm diameter SNWTs together with the already known transport limitations in NWs.

The vertically-stacked SiGe NWTs have been also investigated. Compressively-strained SiGe showed slightly higher mobility than Si ones. One of the possible reasons of the small mobility enhancement is the higher trap density for SiGe nanowires. Additionally, the hexagonal cross section of SiGe NWs with (111) sidewalls could also contribute to mobility degradation

## 5.7 REFERENCES

- [5.1] D. Fleury, G. Bidal, A. Cros, F. Boeuf, T. Skotnicki and G. Ghibaudo, “New Experimental Insight into Ballisticity of Transport in Strained Bulk MOSFETs” *VLSI Tech. Dig.*, pp. 16-17, 2009.
- [5.2] C. Jacoboni, C. Canali, G Ottaviani, and A. A. Quaranta, “A Review of Some Charge Transport Properties of Silicon,” *Solid-state Electron.*, 20,77 (1977).
- [5.3] K. Natori, “Ballistic Metal-Oxide-Semiconductor Field Effect Transistor,” *J. Appl. Phys.*, 76,4879 (1994).
- [5.4] M. S. Shur, “Low Ballistic Mobility in Submicron HEMTs,” *IEEE Electron Device Lett.*, vol. 23, no. 9, pp. 511–513, Sep. 2002.
- [5.5] S. M. Sze and Kwok K. Ng, *Physics of Semiconductor Devices*, 3<sup>rd</sup> edition, John Wiley & Sons, Inc., Hoboken, New Jersey, 2007.
- [5.6] V. Barral, T. Poiroux, F. Rochette, M. Vinet, S. Barraud, O. Faynot, L. Tosti, F. Andrieu, M. Casse, B. Previtali, E. Bernard, R. Ritzenthaler, P. Grosgeorges, G. Lecarval, D. Munteanu, J-L. Autran, S. Deleonibus, “Will Strain Be Useful for 10nm Quasi-Ballistic FDSOI Devices? An Experimental Study”, *VLSI Tech. Dig.*, pp.128-129, 2007.
- [5.7] L. Sekaric, O. Gunawan, A. Majumdar, X. H. Liu, D. Weinstein, and J. W. Sleight, “Size-dependent modulation of carrier mobility in top-down fabricated silicon nanowires.” *Appl. Phys. Lett.*, 95, 023113, 2009.

- [5.8] C. Dupre, T. Ernst, S. Borel, Y. Morand, S. Descombes, B. Guillaumot, X. Garros, S. Becu, X. Mescot, G. Ghibaudo, S. Deleonibus, “Impact of Isotropic Plasma Etching on Channel Si Surface Roughness Measured by AFM and on NMOS Inversion Layer Mobility”, *Proceedings of ULIS*, pp. 133-136, 2008.
- [5.9] A. Hubert et al., *ECS Trans*, 13(1), p.195, 2008.
- [5.10] M.-C. M. Lee and M. C. Wu, “Thermal Annealing in Hydrogen for 3-D Profile Transformation on Silicon-on-Insulator and Sidewall Roughness Reduction,” *Journal of Microelectromechanical systems*. Vol. **15**, no. 2, pp.338–343, 2006.
- [5.11] E. Dornel, T. Ernst, J. C. Barbe, J. M. Hartmann, V. Delaye, F. Aussenac, C. Vizios, S. Borel, V. Maffini-Alvaro, C. Isheden, and J. Foucher. “Hydrogen annealing of arrays of planar and vertically stacked Si nanowires”, *Applied Physics Letters*, vol. 91, 233502, 2007.



# **CHAPTER 6**

## ***THRESHOLD VOLTAGE CONTROL OF VERTICALLY-STACKED NANOWIRE MOSFETS***

# CHAPTER 6 CONTENTS

- 6 Threshold Voltage Control of Vertically-Stacked Nanowire MOSFETs**
  - 6.1 Introduction
    - 6.1.1 Threshold Voltage Control by Independent-Gate FinFET
    - 6.1.2 Vertically-Stacked Nanowire Transistor with Independent Gates
  - 6.2 Optimization of Device Dimensions
  - 6.3 Conclusions
  - 6.4 References

## 6.1 INTRODUCTION

In previous chapter, we discussed the possibility of vertically-stacked SNWTs in terms of  $R_{SD}$  resistance, transport properties, and short channel effect immunity. Another issue for the vertically-stacked SNWTs is how to control the threshold voltage. For various CMOS applications such as HP, LOP, and LSTP, it is important to achieve flexible threshold voltage in a transistor. In this chapter, the possibility of the flexible threshold voltage for vertically-stacked SNWT will be discussed. In particular, the flexibility and the short-channel effects immunity are investigated by numerical simulations.

### 6.1.1 Threshold Voltage Control by Independent-Gate FinFET

In usual case, the threshold voltages are mainly controlled by the gate work function and channel doping level. However, its control by the high- $\kappa$ /metal gate is difficult and complex because of the sensitivity of process conditions and the necessity of the dual metal and/or dual high- $\kappa$ . Furthermore, the use of channel dope technique yields large variations in a wafer due to dopants fluctuations. As one of the solutions for three-dimensional devices, independent-gate FinFETs (IG-FinFETs) have been proposed and demonstrated with excellent experimental results of threshold voltage control by the second gate and the synchronized driving mode operation by the double gates [6.1, 6.2]. The independent gates have been successfully fabricated by using a chemical–mechanical-polishing process or an etch-back process [6.1–6.4] as shown in Figure 6.1.

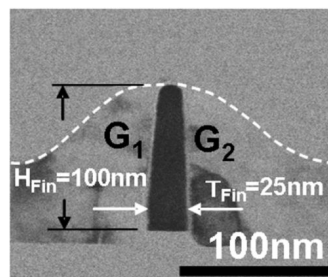


*Figure 6.1 Cross-sectional TEM image of the independent-gate FinFET fabricated by the resist etch back process [6.4].*

### **6.1.2 Vertically-Stacked Nanowire Transistor with Independent Gates**

Vertically-stacked SNWTs with independent gates have been experimentally demonstrated by C. Dupre *et al.* [6.5]. The device has internal spacers between the nanowires as shown in Figure 6.2, named  $\Phi$ FET since its shape is similar to the Greek letter  $\Phi$ . Figure 6.3 summarizes the fabrication process of  $\Phi$ -FET. First, Reduced Pressure- Chemical Vapor Deposition (RP-CVD) was used to epitaxially grow (25nm-Si /25nm-SiGe)x4 superlattice on SOI wafers (Fig.5.3, step 1). A SiN hard-mask was then deposited. After an hybrid DUV/e-beam lithography, the resist was trimmed to define narrow lines (fin width;  $W_{Si} \sim 30\text{nm}$ ). Then, the exposed Si and (Si/SiGe)x4 areas were etched by an anisotropic dry plasma etching (Fig.5.3, step 2). The same RIE reactor was used to remove the SiGe isotropically using a  $\text{CF}_4 + \text{O}_2$  chemistry in order to liberate the suspended Si-nanowires. Then, HTO and SiN were deposited. The partitions between the stacked nanowires were formed by internal spacer obtained by anisotropic and isotropic etchings of SiN selectively to HTO (Fig.5.3, steps 2.1 and 2.2). After chemical cleaning of the channel surface, a  $\text{HfO}_2 / \text{TiN} / \text{Poly-Si}$  gate stack was deposited. The gate stack over the SiN hard mask was removed by Chemical Mechanical Polishing (CMP) (Fig.5.3, step 3). After the gate etching, Source/Drain implantations and spacer formation, dopant atoms were activated and the top of S/D regions were silicided. The fabrication ended with a standard Back-End Of Line (BEOL) process. Figure 6.4 shows the cross-sectional TEM pictures of  $\Phi$ -FET.

This structure is expected to obtain flexible threshold voltage with keeping better short channel effects immunity due to their partially surrounding gates. Figure 6.5 and 5.6 shows the electrical results. Threshold voltage shift have been demonstrated due to a coupling effect between the two gates for  $\Phi$ FET. Moreover,  $\Phi$ FET's  $I_{\text{OFF}}$  currents are 2-decade lower than IG-FinFET ones thanks to an improved electrostatic control.



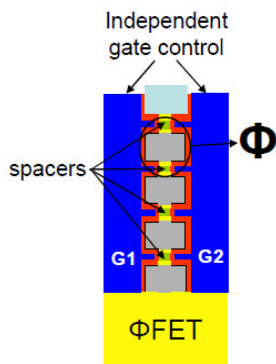


Figure 6.2  $\Phi$ -FET scheme.

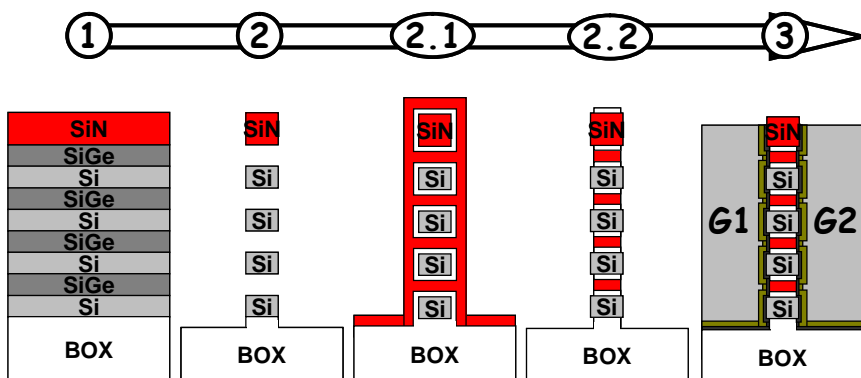


Figure 6.3 Schematic fabrication sequence of  $\Phi$ -FET.

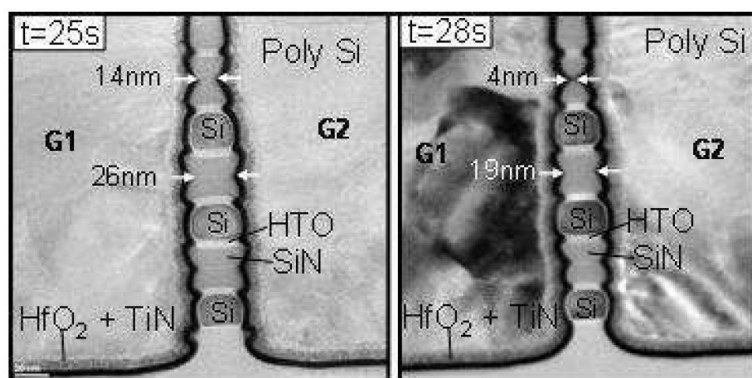


Figure 6.4 Cross-sectional TEM pictures of  $\Phi$ -FET (3 stacked nanowires). Left: 25s SiN isotropic etching Right: 28s SiN isotropic etching.

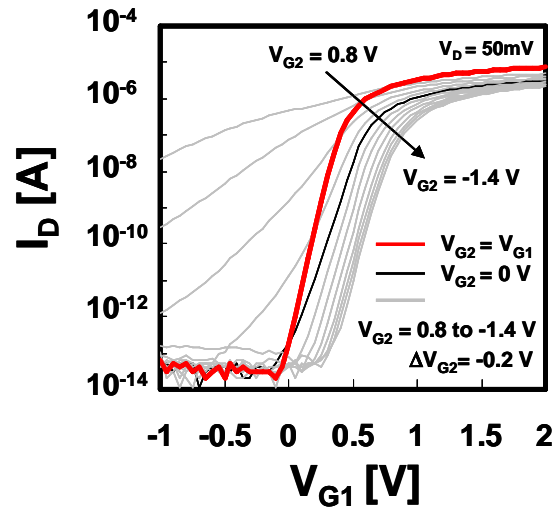


Figure 6.5 Experimental  $I_d$ - $V_{g1}$  characteristics at various  $V_{g2}$  for  $n$ -channel  $\Phi$ -FET. The gate length and channel width are 550 nm and 25 nm, respectively.

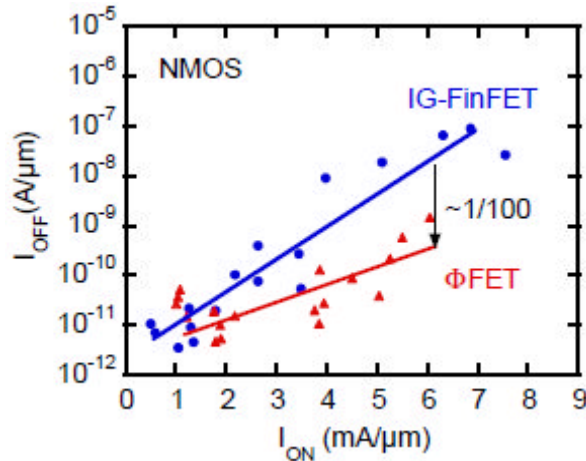


Figure 6.6  $I_{on}$ - $I_{off}$  characteristics comparison between  $\Phi$ -FET and IG-FinFET.

## 6.2 OPTIMIZATION OF DEVICE DIMENSIONS

Although the  $\Phi$ -FETs have been successfully demonstrated, it is necessary to optimize the structure in detail to obtain flexible threshold voltage with better short channel effects immunity. First, we will go through the simulation details. Figure 6.7 shows the simulated  $\Phi$ -FET structure. To extract DIBL associated to the given structure, the currents in the subthreshold regime are determined by using FlexPDF software as

the following procedure.

The source term is detailed as

$$S = \frac{q}{\epsilon} (N_a - N_d + n - p), \quad (6.1)$$

where  $N_a$  is the acceptor density ( $=10^{15} \text{ cm}^{-3}$ ),  $N_d$  the donor density ( $N_d = n_i^2 / N_a$  with  $n_i$  the intrinsic carrier density). Here,  $N_d$  is negligible due to p-type Si.  $n$  and  $p$  are given as a function of the potential  $V$ :

$$n = N_d \exp\left(\frac{qV}{kT}\right), \quad (6.2)$$

$$p = N_d \exp\left(-\frac{qV}{kT}\right). \quad (6.3)$$

The subthreshold current for long-channel MOSFET is given by:

$$I_{Dlong} = \frac{1}{L} \frac{kT}{q} \mu_{eff} Q_{is} \left(1 - e^{-\frac{qV_D}{kT}}\right), \quad (6.4)$$

where  $Q_{is}$  is the inversion charge per surface on the source side which is deduced by integrating  $n$  from the equation (6.2) in the Si volume. The short-channel current thus can be easily rewritten owing to a correction factor C.F [6.6]

$$I_{Dshort} = \frac{I_{Dlong}}{C.F.}, \quad (6.5)$$

$$C.F = \frac{1}{t_{Si} W_{Si} L} \int \exp\left(\frac{-q(V_{short} - V_{long})}{kT}\right), \quad (6.6)$$

where  $V_{short}$  and  $V_{long}$  are the potentials in short and long channels, respectively. The boundary conditions for a simple nanowire structure as shown in Figure 6.8 are adapted to  $\Phi$ -FET structure as following:  $V_G = 0.6 \text{ V}$  on the gate oxide and the built-in voltage ( $V_{BI}$ ) as each nanowire end as

$$V_{BI} = \frac{kT}{q} \ln\left(\frac{N_a N_d}{n_i^2}\right). \quad (6.7)$$

The long-channel case differs from the short-channel case only by applying Neumann boundary conditions: the gradient of the potential (electric field) is forced to zero at each nanowire end. Once the potential distribution is simulated, we used it to extract the

short-channel effects through the natural length  $\lambda$  [6.7],

$$\lambda = \sqrt{\frac{\epsilon_{Si} t_{Si} t_{ox}}{\epsilon_{ox} \eta}}, \quad (6.8)$$

where  $\eta$  is the empirical parameter which varies as a function of the gate configuration: planar ( $\eta=1$ ), double gate ( $\eta =2$ ), tri-gate ( $\eta =3$ ), and gate-all-around ( $\eta \approx 4$ ). In the long-channel, the potential is constant in the middle of the channel, while in the short-channel, the potential is parabolic as shown in Figure 6.9. In terms of subthreshold currents,  $n$  and  $p$  terms can be removed from equation (6.1). Then the equation (6.1) can be rewritten as follows

$$S = \frac{q}{\epsilon} N_a, \quad (6.9)$$

A quantum correction was introduced to have zero-charge at the Si/SiO<sub>2</sub> interface [6.8]. The poisson equation (6.10) thus is solved:

$$\nabla^2 V = S. \quad (6.10)$$

Figure 6.10 shows the simulated subthreshold currents. From the currents, we extracted the threshold voltage and the DIBL. The threshold voltage was extracted using the current constant method:  $V_T = V_G$  at  $I_D = 10^{-7} L/W$ .

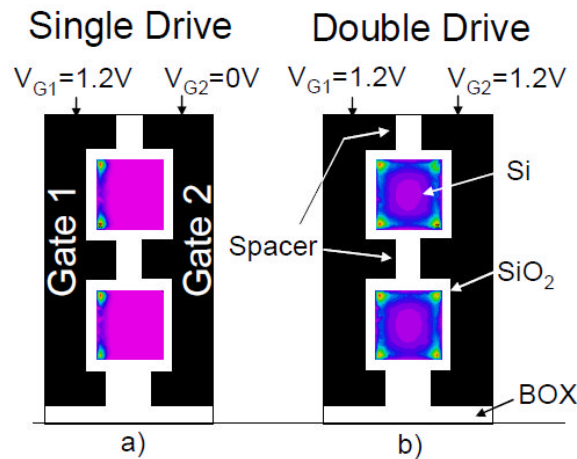


Figure 6.7 Simulated inversion charge density in a  $\Phi$ FET for (a) one gate activated (single drive mode) and (b) two gates activated (double drive mode).

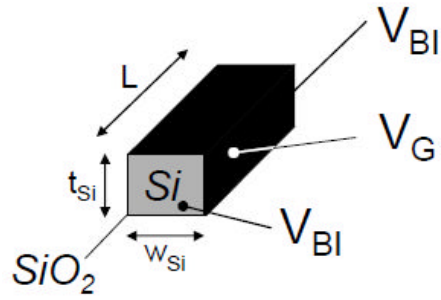


Figure 6.8 Schematic illustration of a SNWT with boundary conditions.

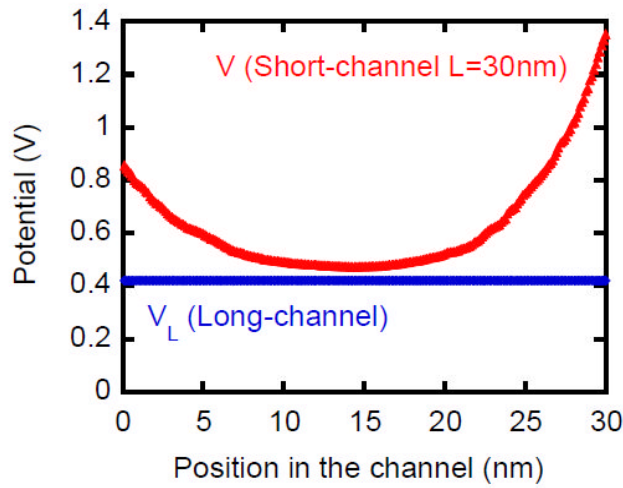


Figure 6.9 Potential along the channel for a long and short-channel transistor.

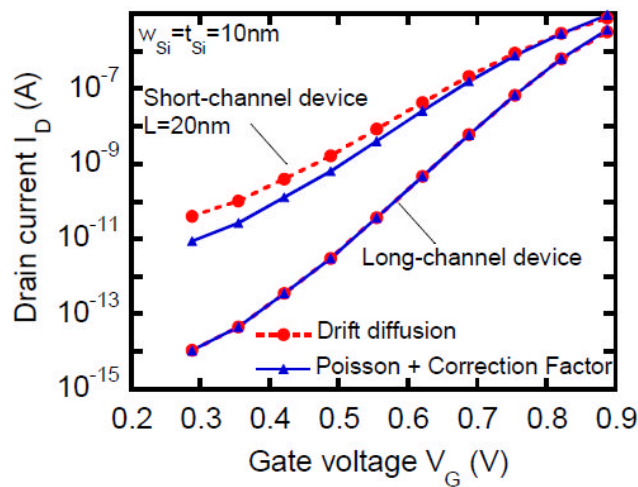


Figure 6.10 Simplified Poisson equation resolution for long-channel with C.F. for short channel is compared to the drift-diffusion model.

As the  $\Phi$ -FET structure is perfectly symmetric, the coupling factor ( $\alpha$ ) can be written as the threshold voltage sensitivity [6.9]:

$$\alpha \equiv \frac{\Delta V_{T1}}{\Delta V_{G2}} \approx \frac{C_{Si}}{C_{ox} + C_{Si} + C_{it}}, \quad (6.11)$$

where  $V_{T1}$  is the threshold voltage on the side of the gate 1, and  $V_{G2}$  is the gate 2 voltage. The coupling factor has been extracted on 2D simulations with long channel. We checked that the coupling is not degraded for shorter gate lengths. For a long-channel, the coupling was evaluated at 0.37 while it is equal to 0.33 at  $L=10$  nm.

From here, the simulation results are discussed. To understand a relationship between flexibility of the threshold voltage and short channel effects immunity, DIBL– $\alpha$  characteristics are plotted as a function of silicon width (Figure 6.11), silicon thickness (Figure 6.12), and spacer width (Figure 6.13). DIBL decreases and  $\alpha$  increases when the Si width is reduced as shown in Figure 6.11. For a given  $W_{Si}$ , DIBL and  $\alpha$  both decrease when changing from an IG-FinFET architecture to a  $\Phi$ -FET. The coupling decrease is understandable considering the rounded gates shape decreasing the gate coupling compared to the IG-FinFET's straight gates. The gate shape immunity to coupling effects has already been studied [6.10]. The lateral gates can screen narrow silicon body from the other gate influence as shown in Figure 6.14. The coupling decrease is understandable considering the rounded gates shape decreasing the gate coupling compared to the IG-FinFET's straight gates. The  $t_{Si}$  variation impact is shown on Figure 6.12. Decreasing the Si thickness improves the architecture electrostatics. The gate coupling is enhanced for the  $t_{Si}$  highest value, reaching the coupling value of IG-FinFET at  $t_{Si} = h_{Si} = 200$ nm. The spacer width  $W_{sp}$  impact is shown on Figure 6.13. For  $W_{sp} = 29$ nm, the spacers are aligned with the Si. This structure is equivalent to an IG-FinFET but with oxide and nitride alternatively with Si. Replacing Si by nitride or oxide decreases slightly the DIBL.  $w_{sp}$  has to be adjusted to have a low DIBL and a satisfying  $\alpha$  value. For  $W_{sp}/W_{Si} \approx 0.5$ , a good DIBL–coupling trade-off is obtained.

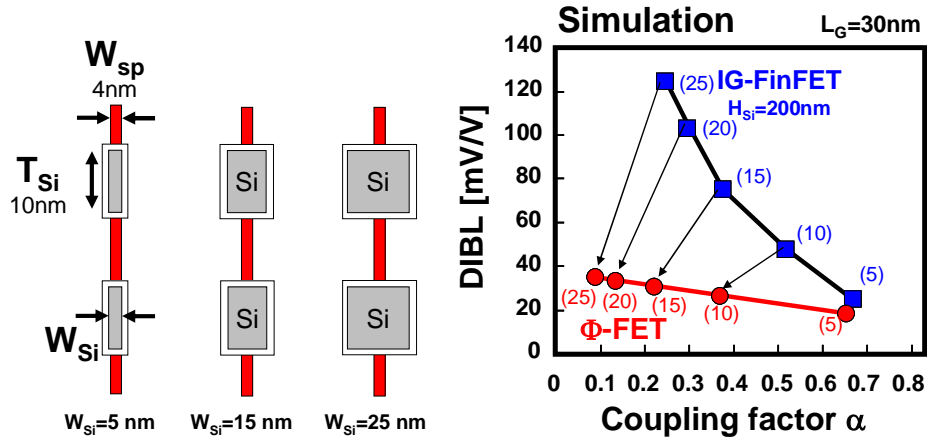


Figure 6.11 DIBL versus coupling factor: Silicon width ( $W_{Si}$ ) dependence.

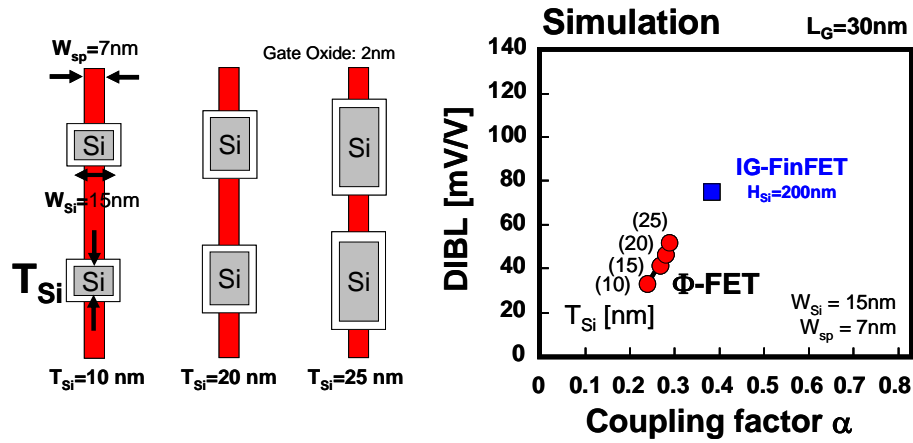


Figure 6.12 DIBL versus coupling factor: Spacer width ( $T_{Si}$ ) dependence.

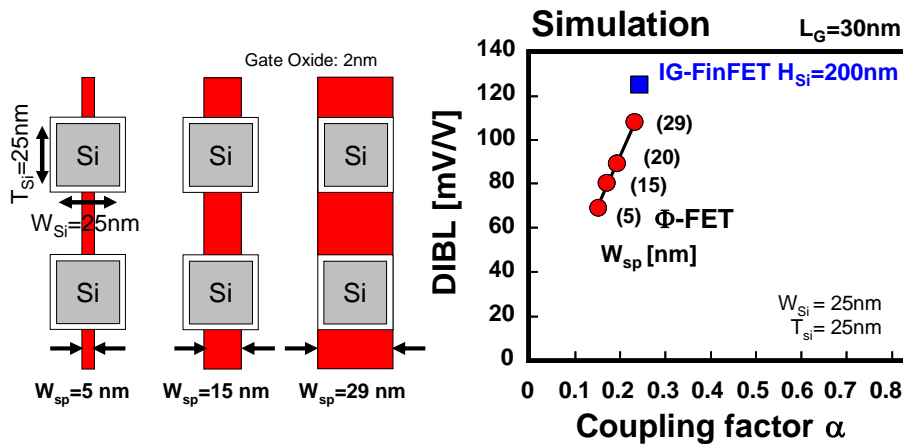


Figure 6.13 DIBL versus coupling factor: Spacer width ( $W_{sp}$ ) dependence.

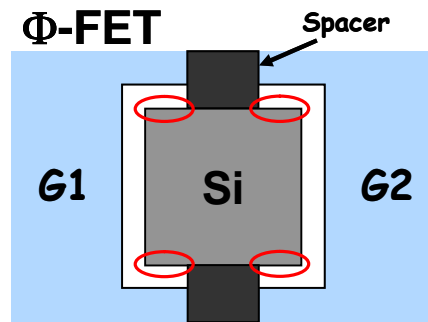


Figure 6.14 Lateral gates can screen narrow silicon body from the other gate influence.

### 6.3 CONCLUSIONS

In this chapter, vertically-stacked SNWTs architectures with independent gate operation ( $\Phi$ -FET) have been evaluated by simulation in terms of the flexibility of the threshold voltage and the short channel effects immunity.  $\Phi$ -FET structure can achieve better short-channel immunity than IG-FinFET owing to the partially surrounded gate structure. On the other hand, the lateral gates screen narrow silicon body from the other gate influence. This causes the degradation of coupling factor. However, the change of cross-sectional dimensions can make the threshold voltage flexible.

The proposed architectures can provide solutions for future technological nodes. It enable to achieve extremely high integration density and low leakage currents with multi-threshold voltage.

### 6.4 REFERENCES

- [6.1] Y. X. Liu, M. Masahara, K. Ishii, T. Tsutsumi, T. Sekigawa, H. Takahima, H. Yamauchi and E. Suzuki, "Flexible Threshold Voltage FinFETs with Independent Double Gates and an Ideal Rectangular Cross- Section Si-Fin Channel", *IEEE International Electron Devices Meeting IEDM*, p. 986, 2003.
- [6.2] Y. X. Liu, M. Masahara, K. Ishii, T. Sekigawa, H. Takahima, H. Yamauchi and E. Suzuki, "A Highly Threshold Voltage-Controllable 4T FinFET with an



- 8.5-nm-Thick Si-Fin Channel”, *IEEE Electron Device Letter*, vol. 25, no. 7, pp. 510–512, 2004.
- [6.3] D. Fried, J. Duster, and K. Kornegay, “Improved Independent Gate N-Type FinFET: Fabrication and Characterization”, *IEEE Electron Device Letters*, vol. 24, no. 9, p. 592, 2003.
- [6.4] K. Endo, Y. Ishikawa, Y. Liu, K. Ishii, T. Matsukawa, S. O’uchi, M. Masahara, E. Sugimata, J. Tsukada, H. Yamauchi, and E. Suzuki, “Four-Terminal FinFETs Fabricated Using an Etch-Back Gate Separation”, *IEEE Transactions on Nanotechnology*, vol. 6, no. 2, p. 201, 2007.
- [6.5] C. Dupré, A. Hubert, S. Bécu, M. Jublot, V. Maffini-Alvaro, C. Vizioz, F. Aussenac, C. Arvet, S. Barnola, J.-M. Hartmann, G. Garnier, F. Allain, J.-P. Colonna, M. Rivoire, L. Baud, S. Pauliac, V. Loup, T. Chevolleau, P. Rivallin, B. Guillaumot, G. Ghibaudo, O. Faynot, T. Ernst, and S. Deleonibus, “15nm-diameter 3D Stacked Nanowires with Independent Gate Operation:  $\square$ FET,” in *IEDM Tech. Dig.*, 2008, pp. 749–752.
- [6.6] A. Tsormpatzoglou, C. A. Dimitriadis, R. Clerc, Q. Rafhay, G. Pananakakis and G. Ghibaudo, “Semi-Analytical Modeling of Short-Channel Effects in Si and Ge Symmetrical Double-Gate MOSFETs”, *IEEE Transactions on Electron Devices*, vol. 54, no. 8, p. 1943, 2007.
- [6.7] R.-H. Yan, A. Ourmazd, K. Lee, “Scaling the Si MOSFET: From Bulk to SOI to Bulk”, *IEEE Transactions on Electron Devices*, vol. 39, no. 7, p. 1704, 1992.
- [6.8] W. Hansch, Th. Vogelsang, R. Kircher, M. Orlowski, “Carrier transport near the Si/SiO<sub>2</sub> interface of a MOSFET”, *Solid-State Electronics*, Vol. 32, no.10, p.839, 1989.
- [6.9] H.K. Lim and J. G. Fossum, “Threshold Voltage of Thin-Film Silicon-on-Insulator (Sol) MOSFET’s, *IEEE Transactions on Electron Devices*, vol. 30, no. 10, p. 1244, 1983.
- [6.10] R. Ritzenthaler, S. Cristoloveanu, O. Faynot, C. Jahan, A. Kuriyama, L. Brevard, S. Deleonibus, “Lateral coupling and immunity to substrate effect in sFET devices”, *Solid-State Electronics*, vol. 50, p. 558, 2006.



# **CHAPTER 7**

## *CONCLUSIONS*

# CHAPTER 7 CONTENTS

## **7 Conclusions**

7.1 Summary

7.2 Conclusions and Perspectives

## 6.1 SUMMARY

In this thesis, to achieve both high speed and low power consumption with high integration for future LSI applications, vertically-stacked silicon nanowire MOSFETs (SNWTs) have been experimentally investigated as one of the possible solutions to various problems related to the CMOS scaling explained in Chapter 1.

The contributions of this work can be divided into three main subjects:

- (1) Study of source/drain series resistance for thick source/drain region in vertically-stacked channel MOSFETs (Chapter 4),
- (2) Study of carrier transport in vertically-stacked SNWTs (Chapter 5),
- (3) Study of threshold voltage controllability for vertically-stacked SNWTs with separated gates (Chapter 6).

In Chapter 2, the device fabrication process was described. Vertically-stacked channel MOSFETs have been successfully fabricated by adapting Silicon-On-Nothing technology with sacrificial SiGe layers.

In Chapter 3, the electrical characterization methods was described. In order to analyze the performances of the fabricated devices, the intrinsic parameters extraction methods, Y-function method and Split C–V, were detailed in the latter half.

In Chapter 4, the influence of *in situ* doped SEG source/drain has been examined for vertically-stacked channel MOSFETs. A large enhancement, by a factor of 2 in the drive current, can be obtained when *in situ* doped SEG process is adopted. Detailed parameter extraction from the electrical measurements shows that the  $R_{SD}$  values can be reduced by 90 and 75% for *n*- and *p*-FETs, respectively, when *in situ* doped SEG is reinforced by adding ion implantation. On the other hand,  $V_T$  roll-off characteristics and the effective mobility behavior are slightly degraded, especially when ion implantation is combined to the SEG process. Mobility analysis has revealed an increase in the

Coulomb scattering with  $L_G$  scaling, indicating the diffusion of dopant atoms from S/D regions. These results indicate an avenue to further improve the performance by optimizing the S/D activation annealing step.

In chapter 5, the carrier transport limiting components for vertically-stacked nanowire MOSFETs have been discussed to obtain better performance with suppressing short channel effects. The optimization of drive currents will have to take into account specific effects to vertically-stacked SNWTs. In particular, the use of SiGe sacrificial layer to make vertically-stacked channels cause the large mobility degradation due to the surface roughness, resulting from the damage of plasma etching. This result can evidence the poor ballisticity in the short channel SNWTs.

The hydrogen annealing can improve the surface-roughness limited mobility a little. Charge pumping measurements, however, revealed that circular-shaped SNWTs, which are formed by the annealing, have a higher interface trap density ( $D_{it}$ ) than rectangular ones, leading to low-field mobility degradation. This high  $D_{it}$  might be caused by the continuously-varying surface orientation. The resulting additional coulomb scattering could partly explain the quite low mobility in 5 nm diameter SNWTs together with the already known transport limitations in NWs.

In chapter 6, vertically-stacked SNWTs with independent gates by internal spacers between the nanowires to control  $V_T$ , which is named  $\Phi$ -FETs, have been evaluated.  $\Phi$ -FETs demonstrated excellent  $V_T$  control by inter-gate coupling effects. As the results of numerical simulations to optimize  $\Phi$ -FETs structures, it have been found that when the spacer width is reduced, the DIBL value can be lowered by a factor of 2 compared to independent-gate FinFETs with the same silicon width. The superior scaling of  $\Phi$ -FETs with narrow spacer results from a better electrostatic control which also attenuates the inter-gate coupling.

## 6.2 CONCLUSIONS AND PERSPECTIVE

In this thesis, it have been demonstrated that gate-all-around silicon nanowire structure can dramatically suppress short-channel effects. Moreover, the introduction of internal spacers between the nanowires can control threshold voltage. These technologies enable to achieve ultra-low power consumption.

In order to obtain high speed operation, the carrier transport limiting components in vertically-stacked SNWTs have been investigated in detail. In addition, the study of mechanical stress to the nanowires indicates a guide of mobility enhancement.

Vertically-stacked channel structure has yielded extremely high drive current density per top-viewed channel width compared to planer MOSFETs. However, this high current may not connect to intrinsic delay reduction because the parasitic capacitance increases in proportion to the number of channels. A benefit of the structure is a possibility of ultra-high integration per given layout area, that is, gate width scaling. For SNWTs, the optimization of the integration is strongly limited by horizontal spaces between the nanowires. The use of vertically stacked channel structure without any nanowires in parallel enables to cancel this limitation. To realize this structure, it is necessary to increase the number of channels in vertical direction. To do that, various process developments are needed such as (Si/SiGe)  $\times n$  superlattice formation shown in Figure 7.1 and its etching with vertically straight line edge.

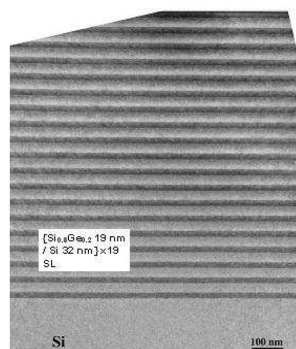


Figure 7.1 Cross-sectional TEM image of the 19 period superlattice with 19 nm  $Si_{0.8}Ge_{0.2}$  and 32 nm of Si [fabricated by J.M. Hartmann in CEA-Leti].

## ***Publications and Presentations***

### *Nanowire MOSFETs*

[Publications as 1<sup>st</sup> author]

1. K. Tachi, N. Vulliet, S. Barraud, K. Kakushima, H. Iwai, S. Cristoloveanu and T. Ernst, “Influence of source/drain formation process on resistance and effective mobility for scaled multi-channel MOSFET,” Special Issue of Solid-State Electronics, (accepted for publication)
2. K. Tachi, S. Barraud, K. Kakushima, H. Iwai, S. Cristoloveanu and T. Ernst, “Comparison of low-temperature electrical characteristics of gate-all-around nanowire FETs, Fin FETs and fully-depleted SOI FETs,” Microelectronics Reliability, (accepted for publication)

[Presentations as 1<sup>st</sup> author]

3. K. Tachi, M. Cassé, S. Barraud, C. Dupré, A. Hubert, N. Vulliet, M.E. Faivre, C. Vizioz, C. Carabasse, V. Delaye, J.M. Hartmann, H. Iwai, S. Cristoloveanu, O. Faynot and T. Ernst, “Experimental study on carrier transport limiting phenomena in 10 nm width nanowire CMOS transistors,” *IEDM Tech. Dig.*, p.784, 2010, San Francisco, US.
4. K. Tachi, N. Vulliet, S. Barraud, B. Guillaumot, V. Maffini-Alvaro, C. Vizioz, C. Arvet, Y. Campidelli, P. Gautier, J.M. Hartmann, T. Skotnicki, S. Cristoloveanu, H. Iwai, O. Faynot and T. Ernst, “3D Source/Drain Doping Optimization in Multi-Channel MOSFET,” 40th European Solid-State Device Research Conference (ESSDERC), pp. 368, 2010, Spain.
5. K. Tachi, M. Casse, D. Jang, C. Dupré, A. Hubert, N. Vulliet, V. Maffini-Alvaro, C. Vizioz, C. Carabasse, V. Delaye, J. M. Hartmann, G. Ghibaud, H. Iwai, S. Cristoloveanu, O. Faynot, and T. Ernst, “Relationship between mobility and



high-*k* interface properties in advanced Si and SiGe nanowires,” *IEDM Tech. Dig.*, p.313, 2009, Baltimore, US.

5. K. Tachi, T. Ernst, C. Dupré, A. Hubert, S. Bécu, H. Iwai, S. Cristoloveanu, O. Faynot, “ Transport Optimization with Width Dependence of 3D-stacked GAA Silicon Nanowire FET with High-*k*/Metal Gate Stack,” *2009 IEEE Silicon Nanoelectronics Workshop*, p.11, 2009, Kyoto, Japan.
6. K. Tachi, T. Ernst, C. Dupré, A. Hubert, S. Bécu, H. Iwai, S. Cristoloveanu, O. Faynot, “ F-FET: Electrostatics and influence of spacer thickness,” *5th EUROSOI*, 2009, Chalmers University of Technology, Sweden.

[Publications as co- author]

7. D. Jang, J. W. Lee, K. Tachi, L. Montes, T. Ernst, G. T. Kim and G. Ghibaudo, “Low-frequency noise in strained SiGe core-shell nanowire p-channel field effect transistors, ” *Appl. Phy. Lett.* 97, 073505, 2010.
8. M. Casse, K. Tachi, S. Thiele and T. Ernst, “Spectroscopic charge pumping in Si nanowire transistors with a high-*k*/metal gate, ” *Appl. Phy. Lett.* 96, 123506, 2010.
9. T. Ernst, K. Tachi, E. Saracco, A. Hubert, C. Dupré, S. Bécu, N. Vulliet, E. Bernard, P. Cherns, V. Maffini-Alvaro (CEA-LETI), J. Damlencourt, C. Vizioz, J. Colonna, C. Bonafos and J. Hartmann, “3D suspended nanowires integration for CMOS and beyond,” *Electrochemical Society (ECS) Transaction*, vol. 25, Issue.7 , pp. 471-478, 2009.

[Presentations as co-author]

10. K-I. Na, W. Van Den Daele, L. Pham-Nguyen, M. Bawedin, K-H. Park, J. Wan, **K. Tachi**, S-J. Chang, I. Ionica, Y-H. Bae, J.A. Chroboczek, C. Fenouillet-Beranger, T. Ernst, E. Augendre, C. Le Royer, A. Zaslavsky, H. Iwai and S. Cristoloveanu, “(Invited) Selected SOI puzzles and tentative answers, ” 6th SemOI workshop & 1st Ukrainian-French SOI Seminar, 2010, Ukraine.
11. A. Hubert, E. Nowak, **K. Tachi**, V. Maffini-Alvaro, C. Vizioz, C. Arvet, J.-P. Colonna, J.-M. Hartmann, V. Loup, L. Baud, S. Pauliac, V. Delaye, C. Carabasse, G. Molas, G. Ghibaud, B. De Salvo, O. Faynot and T. Ernst, “A stacked SONOS technology, up to 4 levels and 6nm crystalline nanowires, with gate-all-around or independent gates (  $\Phi$  -Flash), suitable for full 3D integration,” *IEDM Tech. Dig.*, p.673, 2009, Baltimore, US.
12. T. Ernst, S. Bécu, P. Cherns, L. Durrafourg, C. Dupré, P. Andreucci, A. Hubert, J.-M. Hartmann, J.-P. Colonna, M. Jublot, G. Delapierre, V. Delaye, **K. Tachi**, E. Saracco, J.-F. Damlencourt, J. Foucher, and O. Faynot, “A 3D stacked nanowire technology - Applications in advanced CMOS and beyond,” 7th International Conference on Frontiers of Characterization and Metrology for Nanoelectronics, 2009, US.
13. P. D. Cherns, F. Lorut, S. Beçu, C. Dupré, **K. Tachi**, D. Cooper, A. Chabli, and T. Ernst, “A Study Of Gate-All-Around Transistors By Electron Tomography,” AIP Conf. Proc. 1173, 290, 2009.

*High-k/Metal Gate*

[Publications as 1<sup>st</sup> author]

14. K. Tachi, K. Kakushima, P. Ahmet, K. Tsutsui, N. Sugii, T. Hattori and H. Iwai, “Improvement of interface properties of W/La<sub>2</sub>O<sub>3</sub>/Si MOS structure using Al capping layer,” *Electrochemical Society (ECS) Transaction* Vol.11 No.4 pp.191-198, 2007.
15. K. Tachi, K. Kakushima, P. Ahmet, K. Tsutsui, N. Sugii, T. Hattori and H. Iwai, “Effect of Oxygen for Ultra-Thin La<sub>2</sub>O<sub>3</sub> Film Deposition,” *Electrochemical Society (ECS) Transaction* 3 (3), pp. 425-435, 2006.

[Presentations as 1<sup>st</sup> author]

16. K. Tachi, K. Kakushima, P. Ahmet, K. Tsutsui, N. Sugii, T. Hattori and H. Iwai, “Improvement of interface properties of W/La<sub>2</sub>O<sub>3</sub>/Si MOS structure using Al capping layer,” *212th Electrochemical Society (ECS) Meeting*, Abs#E4-07520, October, 2007, Washington, DC.
17. K. Tachi, K. Kakushima, P. Ahmet, K. Tsutsui, N. Sugii, T. Hattori and H. Iwai, “Effect of Oxygen for Ultra-Thin La<sub>2</sub>O<sub>3</sub> Film Deposition,” *Physics and Technology of High-k Gate Dielectrics 4, 210th Electrochemical Society (ECS) Meeting*, Abs#1128, November, 2006, Cancun, Mexico.

[Publications and Presentations as co-author]

18. K. Kakushima, K. Okamoto, T. Koyanagi, K. Tachi, M. Kouda, T. Kawanago, J. Song, P. Ahmet, K. Tsutsui, N. Sugii, T. Hattori and H. Iwai, “Selection of Rare Earth Silicate with SrO Capping for EOT Scaling below 0.5 nm,” *39th ESSDERC*, pp 403, 2009, Greece.
19. K. Kakushima, K. Tachi, J. Song, S. Sato, H. Nohira, E. Ikenaga, P. Ahmet, K. Tsutsui, N. Sugii, T. Hattori, and H. Iwai, “Comprehensive x-ray photoelectron

- spectroscopy study on compositional gradient lanthanum silicate film,” *Journal of Applied Physics*, vol. 106, 124903, 2009.
20. T. Koyanagi, K. Tachi, K. Okamoto, K. Kakushima, P. Ahmet, K. Tsutsui, N. Sugii, T. Hattori, and H. Iwai, “Electrical Characterization of La<sub>2</sub>O<sub>3</sub>-Gated Metal Oxide Semiconductor Field Effect Transistor with Mg Incorporation,” *Japanese Journal of Applied Physics*, vol. 48, 05DC02, 2009.
21. K. Kakushima, K. Okamoto, K. Tachi, J. Song, S. Sato, T. Kawanago, K. Tsutsui, N. Sugii, P. Ahmet, T. Hattori, and H. Iwai, “Observation of band bending of metal/high-*k* Si capacitor with high energy x-ray photoemission spectroscopy and its application to interface dipole measurement,” *Journal of Applied Physics*, vol. 104, 104908, 2008.
21. M. Kouda, K. Tachi, K. Kakushima, P. Ahmet, K. Tsutsui, N. Sugii, T. Hattori and H. Iwai, “Electrical Properties of CeOX /La<sub>2</sub>O<sub>3</sub> Stack as a Gate Dielectric for Advanced MOSFET Technology,” *Electrochemical Society (ECS) Transaction*, vol. 16, Issue.5 , pp. 153-160, 2008.
22. K. Kakushima, K. Okamoto, M. Adachi, K. Tachi, S. Sato, T. Kawanago, , J. Song, P. Ahmet, K. Tsutsui, N. Sugii, T. Hattori, and H. Iwai, “Impact of Thin La<sub>2</sub>O<sub>3</sub> Insertion for HfO<sub>2</sub> MOSFET,” *Electrochemical Society (ECS) Transaction*, vol. 13, Issue.2 , p. 29, 2008.
23. K. Kakushima, K. Tachi, M. Adachi, K. Okamoto, S. Sato, J. Song, T. Kawanago, P. Ahmet, K. Tsutsui, N. Sugii, T. Hattori, and H. Iwai, “Advantage of La<sub>2</sub>O<sub>3</sub> gate dielectric over HfO<sub>2</sub> for direct contact and mobility improvement,” 38th ESSDERC, p.126, 2008.
24. K. Kakushima, K. Okamoto, K. Tachi, S. Sato, T. Kawanago, J. Song, P. Ahmet, K. Tsutsui, N. Sugii, T. Hattori, and H. Iwai, “Further EOT Scaling below 0.4

- nm for High-k Gated MOSFET,” International Workshop on Dielectric Thin Films for future ULSI devices, p. 9, 2008, Japan.
25. T. Koyanagi, K. Tachi, K. Okamoto, K. Kakushima, P. Ahmet, K. Tsutsui, N. Sugii, T. Hattori, and H. Iwai, “Electrical Characterization of La<sub>2</sub>O<sub>3</sub>-Gated MOSFET with Mg Incorporation,” International Workshop on Dielectric Thin Films for future ULSI devices, p. 73, 2008, Japan.
26. J. Molina, K. Tachi, K. Kakushima, P. Ahmet, K. Tsutsui, N. Sugii, T. Hattori and H. Iwai, “Effects of N<sub>2</sub>-Based Annealing on the Reliability Characteristics of Tungsten/La<sub>2</sub>O<sub>3</sub>/Silicon Capacitors,” *J. Electrochem. Soc.*, Volume 154, Issue 5, pp. G110-G116, 2007
27. T. Kawanago, K. Tachi, J. Song, K. Kakushima, P. Ahmet, K. Tsutsui, N. Sugii, T. Hattori and H. Iwai “Electrical Characterization of Directly Deposited La-Sc Oxide Complex for Gate Insulator Application,” *Microelectronic Engineering*, vol. 84, issue. 9-10, pp. 2235-2238, 2007.
29. S. Sato, K. Tachi, K. Kakushima, P. Ahmet, K. Tsutsui, N. Sugii, T. Hattori and H. Iwai “Thermal-stability improvement of LaON thin film formed using nitrogen radicals,” *Microelectronic Engineering*, vol. 84, issue. 9-10, pp. 1894-1897, 2007.
30. S. Sato, K. Tachi, K. Kakushima, P. Ahmet, K. Tsutsui, N. Sugii, T. Hattori and H. Iwai, “Thermal Stability of Lanthanum Oxynitride Thin Film Fabricated by in-situ Radical Nirtidation,” *54th Japan Society of Applied Physics (JSAP) Spring Meeting*, 29p-ZH-13, 2007, Aoyama Gakuin University, Japan.
31. K. Kakushima, P. Ahmet, J.-A. Ng, J. Molina, H. Sauddin, Y. Kuroki, K. Nakagawa, A. Fukuyama, K. Tachi, Y. Shiino, J. Song, K. Tsutsui, N. Sugii, T.

- Hattori and H. Iwai, "Study of La<sub>2</sub>O<sub>3</sub> Gate Dielectric Suitability for Future MIM and MOSFETs", *2006 IEEE Silicon Nanoelectronics Workshop*, 12th June 2006, Hawaii, USA.
32. H. Nohira, T. Matsuda, K. Tachi, Y. Shiino, J. Song, Y. Kuroki, J. Ng, P. Ahmet, K. Kakushima, K. Tsutsui, E. Ikenaga, K. Kobayashi, H. Iwai and T. Hattori, "Effect of Deposition Temperature on Chemical Structure of Lanthanum Oxide/Si Interface Structure," *2006 International Workshop on Dielectric Thin Films for Future ULSI Devices (IWDTF)*, pp.29-30, November, 2006, Kawasaki, Japan
33. J. Molina, K. Tachi, K. Kakushima, P. Ahmet, K. Tsutsui, N. Sugii, T. Hattori and H. Iwai, "Effects of N<sub>2</sub>-Based Annealing on the Reliability Characteristics of Tungsten/La<sub>2</sub>O<sub>3</sub>/Silicon Capacitors," *Electrochemical Society (ECS) Transaction 3 (3)*, pp. 233, 2006.
34. H. Nohira, T. Matsuda, K. Tachi, Y. Shiino, J. Song, Y. Kuroki, J. Ng, P. Ahmet, K. Kakushima, K. Tsutsui, E. Ikenaga, K. Kobayashi, H. Iwai and T. Hattori, "Effect of Deposition Temperature on Chemical Structure of Lanthanum Oxide/Si Interface Structure," *Electrochemical Society (ECS) Transaction 3 (2)*, pp. 169, 2006.
35. H. Nohira, T. Matsuda, K. Tachi, Y. Shiino, J. Song, Y. Kuroki, J. Ng, P. Ahmet, K. Kakushima, K. Tsutsui, E. Ikenaga, K. Kobayashi, H. Iwai and T. Hattori, "Thermal Stability of LaOX/Si Interfacial Transition Layer", *53rd Japan Society of Applied Physics (JSAP) Spring Meeting*, 23p-V-2, 2006, Musashi Institute of Technology, Japan.
36. K. Nakajima, K. Kimura, K. Tachi, K. Kakushima and H. Iwai, "Hydrogen Depth Profiling in La<sub>2</sub>O<sub>3</sub>/Si(001) by High-resolution Erastic Recoil Detection",

*53rd Japan Society of Applied Physics (JSAP) Spring Meeting, 23p-V-5, 2006,  
Musashi Institute of Technology, Japan.*

***Awards***

*2010 IEEE EDS Japan Chapter Student Award*

*2009 IEEE EDS Japan Chapter Student Award*